NEUTRON STARS IN COMPACT BINARY SYSTEMS: FROM THE EQUATION OF STATE TO GRAVITATIONAL RADIATION

by

Jocelyn S. Read

A Dissertation Submitted in
Partial Fulfillment of the
Requirements for the Degree of

Doctor of Philosophy
in
Physics

at
The University of Wisconsin–Milwaukee
August 2008

NEUTRON STARS IN COMPACT BINARY SYSTEMS: FROM THE EQUATION OF STATE TO GRAVITATIONAL RADIATION

by

Jocelyn S. Read

A Dissertation Submitted in
Partial Fulfillment of the
Requirements for the Degree of

Doctor of Philosophy
in
Physics

at
The University of Wisconsin–Milwaukee
August 2008

John Friedman Date

Jolien Creighton Date

Graduate School Approval Date

ABSTRACT

NEUTRON STARS IN COMPACT BINARY SYSTEMS: FROM THE EQUATION OF STATE TO GRAVITATIONAL RADIATION

by

Jocelyn S. Read

The University of Wisconsin–Milwaukee, 2008
Under the Supervision of Professor John Friedman
and Professor Jolien Creighton

Neutron stars are incredibly dense astrophysical objects that give a unique glimpse of physics at extreme scales. This thesis examines computational and mathematical methods of translating our theoretical understanding of neutron star physics, from the properties of matter to the relativistic behaviour of binary systems, into observable characteristics of astrophysical neutron stars.

The properties of neutron star matter are encoded in the equation of state, which has substantial uncertainty. Many equations of state have been proposed based on different models of the underlying physics. These predict various quantities, such as the maximum stable mass, which allow them to be ruled out by astronomical measurements. This thesis presents a natural way to write a general equation of state that can approximate many different candidate equations of state with a few parameters. Astronomical observations are then used to systematically constrain parameter values, instead of ruling out models on a case-by-case basis.

Orbiting pairs of neutron stars will release gravitational radiation and spiral in toward each other. The radiation may be observable with ground-based detectors. Until the stars get very close to each other the rate of inspiral is slow, and the orbits are approximately circular. One can numerically find spacetime solutions that satisfy the full set of Einstein equations by imposing an exact helical symmetry. However, we find that the helically-symmetric solution must be matched to a waveless boundary region to achieve convergence. Work with toy models suggests this lack of convergence is intractable, but the agreement of waveless and helical codes validates the use of either approximation to construct state-of-the-art initial data for fully dynamic binary neutron star simulations.

The parameterized equation of state can be used with such numerical simulations to systematically explore how the emitted gravitational waves depend on the properties of neutron star matter. Late-time waveforms from numerical simulations with varying equation of state are matched onto early-time post-Newtonian waveforms to generate hybrid waveforms for data analysis. The variation in waveforms from changing the EOS is compared to the noise properties of the tunable Advanced LIGO detector to determine measurability of neutron star and equation of state parameters.

John Friedman Date

Jolien Creighton Date

to

Mom and Dad,

Grandma and Granddad

Contents

Preface

Chapters 2 and 3 contain material from

"A parametrized equation of state for neutron-star matter." Jocelyn S. Read, Benjamin D. Lackey, John L. Friedman, Benjamin J. Owen.

Chapters 4 and 5 contain material from

"Models of helically symmetric binary systems." Shin'ichirou Yoshida, Benjamin C. Bromley, Jocelyn S. Read, Koji Uryu, John L. Friedman. Class. Quantum Grav. 23 (2006) S599-S613.

Chapter 7 is based on

"Constraints from binary inspiral on the equation of state above nuclear density." Jocelyn S. Read, Charalampos Markakis, Masaru Shibata, Koji Uryu, Jolien Creighton, John L. Friedman.

Acknowledgements

I first thank my collaborators on the work presented in this thesis. I am delighted to have worked with so many wonderful people. For the work in Part I on astrophysical constraints for piecewise polytropes, I thank Ben Lackey for successfully producing understandable plots of his constraint calculations. I thank Ben Owen for contributing his analysis of the astrophysical observations we base our constraints on. I thank my collaborators on the helical toy model comparison work in Part II, Shin Yoshida and Ben Bromley. I also thank Koji Uryu for the computational inspiration of my toy model implementation, as well as the use of his codes for the initial data of the numerical simulations for different EOS in Part III. I thank Harris Markakis, for constructing that initial data, and Masaru Shibata, for running his state-of-the-art code for neutron star numerical evolution and gravitational wave extraction with our EOS. I particularly thank my dissertation co-chairs: John Friedman, for invaluable guidance throughout my graduate career, many interesting problems to work on, and eventually-imparted understanding in nigh-uncountable areas of physics. Jolien Creighton, for help this last year in navigating many perilous seas including those of data analysis, LIGO conventions, and typesetting.

The physics department at UWM is the kind of community I'd like to spend my life working in. My fellow grad students, especially, helped balance working hard with hanging out in people's offices making dorky jokes. It's hard to overstate my satisfaction. Dissertation-related thanks especially to Nick for proofreading and Ben for last minute checks of research results.

I also thank my family, particularly Mom, for showing me never to be afraid to jump into an entirely new field of study, and Dad, for encouraging pride in nerdiness and good communication skills despite introversion. And I thank my husband, Uwe, for thinking I kick ass and being awesomely supportive.

Conventions

In the discussion of neutron star equation of state thermodynamics, n will refer to number density and ϵ to total energy density. The mass per baryon, $m_b = 1.66 \times 10^{-27}\,\mathrm{kg}$, of the matter dispersed to infinity is used define a rest mass density $\rho \sim n$.

Nuclear density is taken to be $\rho_{\mathrm{nuc}} = 2.7 \times 10^{14}\,\mathrm{g/cm^3}$.

Factors of c are suppressed (setting $c = 1$) in thermodynamic discussions, and the pressure p is generally reported as p/c^2. Note p/c^2, ϵ, and ρ share units of $\mathrm{g/cm^3}$.

The enthalpy per rest mass is h, the pseudo-enthalpy is $H = \log(h)$.

Spacetime indices will be Greek, as in α, β, γ, $\dots$, while spatial indices will be Latin, as in a, b, c, $\dots$. Indices early in the alphabet can be regarded as abstract indices, and those later in the alphabet, such as μ, ν, λ, and i, j, k, can be regarded as concrete indices taking values such as $\mu = 0, 1, 2, 3$ and $i = 1, 2, 3$.

The Fourier transform conventions are

$$\tilde{x}(f) = \int_{-\infty}^{\infty} x(t) \mathrm{e}^{-2\pi i f t} dt$$

$$x(t) = \int_{-\infty}^{\infty} \tilde{x}(t) \mathrm{e}^{2\pi i f t} df.$$

List of Tables

List of Figures

Introduction

We begin with the death of a star.

When the star is young, although the gravity of the star pulls matter inward, the nuclear fusion reactions radiate energy outward, supplying enough pressure to keep the star at the size we see. Eventually, however, the raw materials in the core are used up. The fusion halts, and the outward pressure drops. Without this pressure, the core collapses in on itself until something else provides support.

For most stars, those around one to eight times the mass of the sun, this comes from the gas of electrons surrounding the nuclei. The pressure from degenerate electrons, unable to drop to already-filled lower energy states, is enough to support the core. The result is a white dwarf.

But for larger stars, the pull of gravity will overcome the electron pressure in the core of the star. The electrons are pushed in to merge with protons in the nuclei and make neutrons. Nuclei with extra neutrons are more unstable, and neutrons start to drip out of the nuclei and mix with the gas of electrons that surrounds them.

As gravity pulls the matter of the star tighter, the overall density reaches the density of the atomic nuclei, leaving no division between each nucleus and its surroundings. The pressure that supports the star against collapse now comes from the degeneracy of the neutrons themselves. The resulting fluid of mostly neutrons may form the core of a neutron star.

Dense matter and neutron star astrophysics

The matter of neutron stars is at extreme densities, ranging up to central densities that likely exceed $10^{15}\,\mathrm{g/cm^3}$ and may reach $10^{16}\,\mathrm{g/cm^3}$. This is up to a hundred times the density of an atomic nucleus; the mass of a sun or two is packed into a

Table 1 : Example particles in the classes relevant to neutron stars and ground states. No two fermions can occupy the same state, by the Pauli Exclusion Principle, which results in a degeneracy pressure that supports fermionic matter against collapse.

Fundamental Particles		
Fermions		Bosons
Leptons	Quarks	force mediators: photons, gluons, …
neutrinos (ν), electrons (e), muons (μ), …	up, down, strange, …	

Hadrons (quark/gluon composite particles)		
Baryons (fermionic)		Mesons (bosonic)
Nucleons	Hyperons	paired quarks: pions (π), kaons (K), …
the lightest baryons: neutrons (n) and protons (p)	baryons that include strange quarks: Lambda (Λ), Sigma (Σ), Xi (Ξ), …	

sphere of 20 to 30 km in diameter. And yet, for most of the star's existence, the matter is effectively cold: it is in its lowest possible energy configuration.

We do not know exactly how this cold dense matter behaves. It does not exist on earth. We can create comparably *dense* matter in experiments like the Relativistic Heavy Ion Collider (RHIC) by smashing gold nuclei together, but it is very hot and out of equilibrium. The extrapolation back to the equilibrium ground state is both difficult and model-dependent.

The uncertainty is not a question of unknown fundamental physics—the standard model, particularly the theory of quantum chromodynamics (QCD), which describes the interactions of the colour-charged quarks and gluons that make up protons and neutrons and other particles described in Table 1, is valid at these scales. However, it is difficult to determine the residual interactions of colour-neutral hadrons, and the many-body problem is computationally intractable.

Figure 1 : A schematic diagram of the phases of matter described by quantum chromodynamics, over a range of temperatures T and chemical potentials μ. The matter we ordinarily observe is a two-phase mixture of vacuum and nuclear matter. In neutron star cores a single phase of nucleon-based matter forms, which may also incorporate mesons and hyperons as density increases. At high pressures, the $T = 0$ ground state may not involve hadrons at all, but transition to some form of quark-gluon gas or liquid.

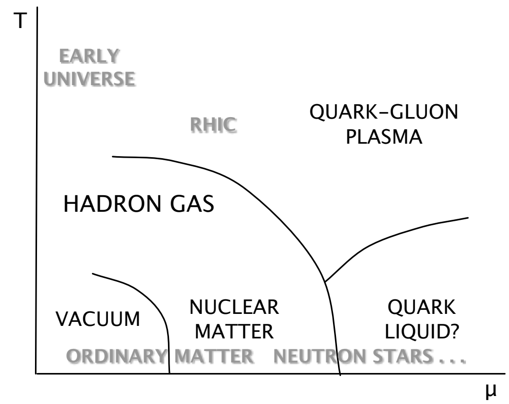

Instead, the ground state must be modelled by hypothesizing the particular composition of particles and the forms of their interaction potentials, and by approximating the many-body problem with a few levels of multi-particle interactions or mean field approximations. While neutrons and protons are the known constituents of nuclei, additional types of particles, hyperons and mesons, can come into play as densities increase. At very high densities the equilibrium ground state of matter may not even contain composite particles like neutrons and protons at all, but rather be a soup of the fundamental quarks themselves. A QCD phase diagram is shown in Fig. 1.

Unable to measure the properties of the QCD ground state on earth, we look to observe their signatures on neutron stars in outer space. Most observed neutron stars are pulsars, spinning neutron stars with relativistic electrons emitting radiation in cones from their magnetic poles as sketched in Fig. 2. Whenever the spin brings a cone in line with the earth, we see a pulse of radio and/or x-ray emissions. Observations of these pulses tell us how fast the star spins. In some cases, further information can be deciphered.

If the neutron star is in a binary system with another star, the orbital motion

Figure 2 : A diagram of the lighthouse model of pulsar emission. Charged particles accelerated along magnetic field lines create beams of radiation, which sweep around with the rotation of the star. When the beam points toward the earth, a pulse of radiation is observed.

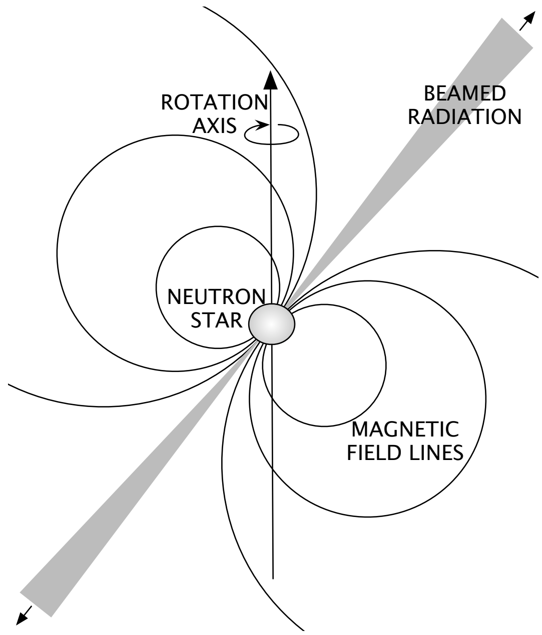

modulates the pulse frequency. This redshifting and blueshifting gives limits on the mass of the stars. If the companion is optically visible and eclipsed by the neutron star, modulation of the optical signal combined with its spectral shifting allows an estimate of both masses. A neutron star may also accrete layers of matter from a large companion, leading to bursts of x-rays believed to come from thermonuclear reactions over the full surface of the neutron star. Modelling this burst gives an estimate of the radius of the x-ray emission if the mass can also be measured.

When the companion star in a binary is also a neutron star, the orbital dynamics can become highly relativistic. Observations of redshift, period, and the advance over time of the orbital periastron—similar to the advance of the periastron of Mercury—allow precise determination of the two neutron star masses as shown in Fig. 3. A double-pulsar system, where pulses from both of the neutron stars in the binary are measured, yields additional information about the orbital dynamics which may allow an estimate of a neutron star's moment of inertia. The first double-pulsar system, PSR J0737−3039, was discovered in 2004.

Figure 3 : Determination of neutron star masses in the Hulse-Taylor binary, a pulsar with a neutron star companion. The solid lines correspond to mass values compatible with measured orbital parameters $\dot{\omega}$, $\dot{P}_b$, and γ. The parameter γ characterizes the time delays in pulse arrival from redshifting and time dilation as the pulsar orbits. The parameter $\dot{\omega}$ is the rate of periastron advance. The parameter $\dot{P}_b$ is the rate of change of the orbital period, which both confirms the masses determined by the first two parameters and the prediction of general relativity that the binary pulsar emits energy through gravitational waves. The additional orbital parameters s and r also confirm the predictions of general relativity. Figure from [1].

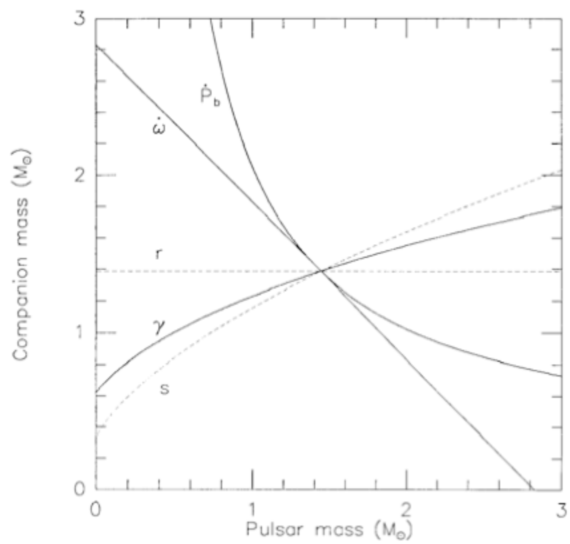

The signature of the behaviour of matter at the highest densities lies in the observations that depend on the core structure of the neutron star: properties like the star's mass, spin, and size. By observing dynamical neutron star behaviour we can also infer neutron star properties like tidal deformability and the resistance to changes in spin (moment of inertia), which depend on the internal structure of a particular neutron star. All these properties can be traced back to one function: the equation of state (EOS) of the neutron star matter, which describes the relationship between pressure and energy density in the neutron star.

If we observe large neutron star masses, we know that cold dense matter provides enough pressure to support them against collapse to a black hole. We can look at the fastest spinning stars and learn that the core must be dense enough to bind matter at the equator moving at the speed such rotation requires. The radius and interior structure of a particular neutron star are determined by the precise way the pressure of cold dense matter varies with increasing density. Thus, by observing such properties, we begin to be able to rule out hypotheses about the ground state at various densities.

A new observational tool for neutron star astrophysics is the detection of gravitational waves. Orbiting compact objects emit gravitational radiation and spiral in toward each other, eventually colliding. As two neutron stars approach each other at the end of the inspiral, the tidal deformation modifies their orbits, changing the gravitational waveform.

On earth, gravitational wave detectors like the Laser Interferometer Gravitational-wave Observatory (LIGO) are capable of measuring the ripples in space-time that radiate from inspiralling neutron stars. Upgrades to the detectors, such as Advanced LIGO, may improve the sensitivity enough to measure effects of the EOS of neutron stars on the gravitational waves measured on earth.

Levels of approximations

To learn about the nature of matter above nuclear density from astrophysical observations, we must link the femtometre (10^{-15} m) scale interaction of hadrons to the behaviour of neutron stars tens of kilometres across, or even to gravitational waves hundreds of kilometres (10^5 m) long. This involves chaining together many levels of physically reasonable approximations.

For example, the structure of a neutron star requires the full equations of general relativity to calculate. Yet the matter within it can be modelled using flat-space quantum field theory—or, at moderate densities, nonrelativistic theory—from the perspective of a comoving, instantaneously inertial observer. The spacetime curvature is significant only over distances much larger than those relevant to particle interactions.

In turn, the input into the structure equations is the equation of state, a single function of pressure versus density that characterizes the behaviour of a piece of neutron star matter. Details of nuclear structure and mixed phases are averaged.

Large-scale neutron star structure is well approximated in most cases by that of a spherical, stationary star. Imposing such symmetries simplifies the usually-complicated Einstein equations, allowing them to be written as a system of first-order differential equations. A small rotational perturbation on the static solution is sufficient to calculate the moment of inertia for the more quickly spinning member the double-pulsar system J0737−3039A. The simplified equations allow efficient calculation of predicted moments of inertia for a wide range of EOS. It is only in the calculations of maximum allowed rotation that we must resort to considering neutron stars with arbitrary spin.

Different levels of approximation are used for the orbital dynamics of binary neutron stars over the course of their evolution. For most of their lifetimes, the neutron stars are far apart and slowly inspiralling. They can be approximated as point particles, with the first order relativistic corrections of the post-Newtonian approximation sufficient to model their gravitational interaction. One models the particle dynamics by closed orbits, neglecting the small infall due to gravitational radiation. The secular evolution of orbital characteristics, such as the change in period with time, is then calculated on longer timescales by balancing the gravitational-wave luminosity of the system against the change in binding energy with orbital separation.

This is the approximation used to calculate neutron star masses, and moments of inertia, from binary pulsar observations. It is also used to generate waveform templates for gravitational wave detection searches.

A similar approximation can be made to calculate the full fluid profile of two neutron stars instantaneously following circular orbits. A series of such snapshots with decreasing orbital separation can be pieced together to form a quasiequilibrium sequence, modelling the hydrodynamic-dependent properties of the binary.

For the final inspiral and merger of two neutron stars, however, the requirements for the above approximations break down. The stars are moving very quickly, they are very close, and they have complicated hydrodynamics. The physics in such a situation can only be modelled with the full four-dimensional simulations of Einstein's equations including relativistic hydrodynamics. Such simulations are computationally expensive; fortunately the approximate methods suffice until near the end of the evolution.

Results using one approximation often feed into models using different approximations. The perfect fluid equation of state is an ingredient for the general relativistic calculation of neutron star properties. Quasiequilibrium data are used as initial conditions for full numerical simulations. The neutron star mass and moment of inertia, calculated for slowly rotating isolated stars in full general relativity, can be used to characterize stars through dynamic orbital motion in a binary system. This dynamical motion can itself be calculated in the entirely different approximation that the stars are point particles, with gravitational effects calculated using a post-Newtonian expansion.

Questions of this thesis

We have discussed how the observable properties of cold dense matter in neutron star cores are determined by the equation of state, and how the composition and interactions of cold matter at high densities are not fully known.

It is desirable to parameterize our lack of knowledge, ideally with some set of natural parameters for the theory which can be systematically constrained by observations. But this has not been done for high density nuclear equations of state. Instead a set of candidate equations of state is considered, with the choice of elements changing on a timescale of half decades, and individual candidates are allowed or ruled out by a given astrophysical observation.

The reason for this is that the natural parameters are tied to the models used to generate the equation of state, and the models used to describe cold dense matter vary so much that there is no generic natural choice of parameters. Yet, the candidate equations of state that span many different classes of models show reasonably simple forms over a limited swathe of possible pressures.

In Part I, I answer the following question: Can we find a systematic way to characterize the neutron star equation of state by varying a small number of parameters that are independent of the particular microphysical model, such that astrophysical observations can be used to limit the values of these parameters?

❃

We have also outlined varying levels of approximation used to describe the physics of neutron star binaries. When one considers certain characteristic properties, such as the binding energy of the system, there is a conflict between a common method of constructing quasiequilibrium data and the known higher-order post-Newtonian approximation.

The conformally flat approximation assumes that several of the degrees of freedom in the spacetime metric are zero; specifically, the departure of the spatial part of the metric from conformal flatness. This is accurate to first post-Newtonian order, but describes a spacetime with no radiation.

Imposing exact helical symmetry on the binary system provides equations for these additional components, resulting in a spacetime that satisfies the full set of Einstein equations. This may give more accurate characteristics of the binary properties and better initial data for numerical simulations.

In Part II, I answer the following question: Can a full helical symmetry assumption be used to construct convergent numerical solutions for quasiequilibrium neutron stars which go beyond conformal flatness?

Finally, we have discussed how gravitational-wave detectors such as LIGO and Advanced LIGO may open a new window on the astrophysics of neutron stars. For most of the frequencies that the detector is sensitive to, neutron star binary waveforms are expected to be well-described by point particle post-Newtonian waveforms. Quasiequilibrium simulations seem to show fluid-dynamic-dependent properties at the edges of Advanced LIGO's frequency band, but these are difficult to translate into gravitational wave effects.

Masaru Shibata at the University of Tokyo has started running simulations of binary neutron stars with parameterized equations of state, using initial data created by Koji Uryu and Charalampos Markakis. These are the first fully relativistic binary neutron star simulations that start several orbits before merger. This allows them to be matched onto post-Newtonian point-particle inspirals to yield full waveforms suitable for work on data analysis and parameter extraction.

In Part III, I answer the following question: Will the effects of the neutron star equation of state be visible with Advanced LIGO, and, if so, how accurately might an observation of a binary neutron star inspiral characteristics in Advanced LIGO constrain equation of state properties?

Part I

Equations of state for neutron stars

Chapter 1

Properties of cold dense matter

The structure and dynamics of neutron stars are determined by the behaviour of matter within it. For most of the lifetime of a neutron star, the bulk of its matter is cold and degenerate: that is, the matter is at temperatures below the Fermi temperatures of its constituent particles, so they are in their ground states.

The Fermi temperature can be estimated as follows: Let μ_0 be the Fermi energy or chemical potential at a temperature $T = 0$, and κ_F the radius of the Fermi sphere in momentum space scaled by $\hbar$. Then $\mu_0 = (\hbar\kappa_F)^2/2m$ for a particle of mass m. In a spatial volume V, the number of states N in the Fermi sphere is $2(2\pi)^{-3}V\left(\frac{4}{3}\pi{\kappa_F}^3\right)$ for particles of spin $\frac{\hbar}{2}$. At $T = 0$ this N is equal to the total number of particles in the volume V.

The Fermi temperature, T_F, where $kT_F = \mu_0$, is

$$T_F = \frac{\mu_0}{k} = \frac{\hbar^2}{2mk}{\kappa_F}^2 = \frac{\hbar^2}{2mk}\left(3\pi^2\frac{N}{V}\right)^{\frac{2}{3}} \tag{1.1}$$

and at temperatures below this the particles are degenerate[2], and their energy and chemical potential will be approximately equal to those calculated at zero temperature. For nucleons above nuclear density, $T_F \gtrsim 10^{11}\,\mathrm{K}$.

Although neutron stars are born with temperatures of $\sim 10^{11}\,\mathrm{K}$, they cool to $\sim 10^8\,\mathrm{K}$ in a month and to $\sim 10^6\,\mathrm{K}$ in less than a million years [3]. The temperature-dependent region for an isolated neutron star is a layer of thickness $\sim 1\,\mathrm{m}$, containing only a tiny fraction of the matter. The structure of neutron stars will be almost entirely determined by the zero temperature equation of state.

We will also be considering nonmagnetic neutron star matter, an appropriate approximation for $B < 10^{16}$ G as the magnetic energy density is much smaller than the pressure density.

1.1 Thermodynamics of neutron star matter

Consider a piece of matter small on the scale of hydrodynamic motions and variations in gravitational potential in neutron stars. This is on the scale of centimetres or metres, still large compared to the scale of the particles and nuclear structures that comprise the matter. Its properties can be described statistically.

Within the considered piece, we model the physics entirely from the perspective of a local Lorentz frame comoving with the fluid element, thereby separating the local behaviour of particle physics from large-scale general relativistic effects. The change in the metric of the neutron star will be small over centimetre- to metre- length regions.

At scales larger than this, the structure of the neutron star will depend only on properties averaged over the small piece of matter, i.e. the thermodynamic variables. For degenerate or ground-state matter, these properties are entirely determined by n, the average number density of baryons measured in the comoving frame.

If ϵ is the total energy density measured in the frame, we have the first law of thermodynamics for the heat gained per baryon, $\bar{d}Q$, of

$$\bar{d}Q = d\left(\frac{\epsilon}{n}\right) + pd\left(\frac{1}{n}\right) \tag{1.2}$$

with pressure p, volume per baryon $1/n$, and energy per baryon ϵ/n.

In a reversible process, $dQ = T\,ds$, with s the entropy per baryon and T the temperature, and the second law of thermodynamics becomes

$$d\epsilon = \rho T\,ds + \frac{\epsilon + p}{n}dn \tag{1.3}$$

where I have used the average rest mass per baryon of the neutron star matter dispersed to infinity, m_b, to define a rest mass density

$$\rho = m_b n. \tag{1.4}$$

The enthalpy h per unit rest mass is

$$h = \frac{\epsilon + p}{\rho}, \tag{1.5}$$

in units where $c = 1$.

Since the neutron star matter is almost entirely in the ground state, at temperatures below the Fermi temperature, the entropy per baryon is nearly uniform over the star. Thus the increase in pressure and density will be be approximated as isentropic, with $ds = 0$, and thus both adiabatic and reversible. Then Eq. (1.3) becomes

$$d\epsilon = \frac{\epsilon + p}{\rho} d\rho, \tag{1.6}$$

which can be rearranged to give

$$\frac{d\log(p)}{d\log(\rho)} = \frac{\epsilon + p}{p}\frac{dp}{d\epsilon} = \Gamma \tag{1.7}$$

defining Γ, the adiabatic index, characterizing the change in pressure per change in comoving volume at constant entropy. The adiabatic index also characterizes the response of matter to density perturbations as long as the perturbations are slow enough to maintain equilibrium. The speed of sound in the fluid is given by

$$v_s = \frac{\partial p}{\partial \epsilon}. \tag{1.8}$$

1.2 Equation of state

The equation of state of matter in neutron stars is usually described using $p(\epsilon)$, the pressure as a function of energy density, which is required to solve the equations for stellar structure that will be discussed in Chapter 2. However, ϵ itself can be considered a function of the baryon density n or rest mass density ρ.

The microscopic stability of matter requires a monotonically increasing equation of state, $dp/d\rho \geq 0$, or else small bits of matter are prone to spontaneously collapse. For the matter to satisfy causality, the speed of sound given by Eq. (1.8) must be less than one.

For neutron stars, the matter will be in an equilibrium under reactions involving both nuclear and electromagnetic interactions. The timescales of achieving chemical and nuclear equilibrium are all short compared to the lifetime of neutron stars. The ground state of the matter can thus be calculated at a fixed number density by finding the minimum energy achievable through varying the composition. In a nuclear physics context, the equation of state is usually constructed to minimize the internal energy per baryon as a function of number density.

This ground state energy density $\epsilon(n)$ then determines the pressure of the matter via the first law of thermodynamics, as

$$p = n^2 \frac{d\,(\epsilon/n)}{dn} \tag{1.9}$$

The question thus becomes: what is the ground state energy of matter at a given number density? Although at zero temperature this is in theory entirely determined by the standard model, in practise the complex many-body interactions of the system are difficult to calculate. The fundamental interactions of particles will determine these properties.

1.3 Physics on the femtometre scale

Various methods are used to describe the dependence of energy density on rest mass density.

The equation of state is known fairly well up to neutron drip, at an energy density of about $10^{11}\,\mathrm{g\,cm^{-3}}$. Below this density, reasonable variations in models up to neutron drip have negligible effect on the equation of state [4].

At low densities the balance of nuclear and electromagnetic forces gives a minimum energy density for nuclei at the composition of iron. While the energy density is dominated by the baryons, the pressure is dominated by the surrounding gas of nonrelativistic and degenerate electrons, which gives an equation of state in the ideal noninteracting nonrelativistic limit of $p \propto \rho^{5/3}$.

As the density increases, the electrons providing the pressure becomes relativistic, $p \propto \rho^{4/3}$ in the ideal relativistic limit. The nuclei become more neutron-rich, as protons undergo inverse beta decay,

$$p + e^- \to n + \nu_e \tag{1.10}$$

absorbing some of the high-energy electrons. The neutrinos produced diffuse to the edge of the star and escape. At around $4.3 \times 10^{11}\,\mathrm{g\,cm^{-3}}$, the neutron-rich nuclei become unstable and neutrons begin to "drip" out of the nuclei, forming a superfluid neutron gas [5] around the nuclei.

One method of modelling the EOS in this region is the Compressible Liquid Drop Model [6], which calculates energy density contributions from the bulk of nucleons in a nucleus, the surface of the nucleus, and coulomb contributions from nuclei and nuclear structures, plus a uniform electron gas contribution. This method generates the crust EOS of the SLY4 EOS table, which is the basis of the fixed crust EOS in Chapter 3 and Part III of this thesis.

The saturation density of symmetric nuclear matter, matter with equal numbers of protons and neutrons, is $\rho_0 \simeq 2.5 \times 10^{14}\,\mathrm{g\,cm^{-3}}$. This is the zero-pressure density of the ground state of nuclear matter, and due to the short distance repulsion of the strong force, the nucleons remain at roughly this density as the size of a nucleus grows [3].

After neutron drip, as neutron star matter approaches the saturation density, the spacing of the nuclei in the equilibrium configuration decreases, and the inverse beta decay continues, until the matter is uniform fluid of neutron matter, containing a small dissolved fraction of protons and electrons. Muons appear when the electron chemical potential μ_e surpasses $m_\mu c^2 = 105.7$ MeV [6].

Computation of the energy at higher density is a many-body problem with an array of possible computational techniques. EOS calculations may use realistic nucleon-nucleon potentials, developed through scattering, and/or phenomenological descriptions with effective three-body or higher corrections. Variational, Bruekner-Bethe-Goldstone, and relativistic mean field calculations are used to determine the ground state energy.

As densities increase, new reactions may become energetically favourable, allowing the production of hyperons, mesons, and quarks. This requires additional terms in the Hamiltonians or Lagrangians of the above theories. The density of appearance for these particles is uncertain; few experiments constrain hyperon-nucleon interactions, which must be calculated from QCD.

At very high energies, the equilibrium state of nuclear matter may not be well described in terms of baryons and hyperons, but rather in terms of the fundamental quarks. The asymptotic behaviour of QCD suggest that quark interactions become weak at sufficiently high densities, transitioning from bound hadrons to a liquid quark phase. Hybrid models of the EOS mix quark and hadron phases in an intermediate region.

Chapter 2

Neutron star structure

The cold equation of state above nuclear density determines the macroscopic properties of neutron stars, which are potentially extractable from astrophysical observation. Unlike white dwarfs, all neutron stars are expected to be described by the same one-parameter equation of state, so multiple neutron star observations can be used to constrain the properties of the single neutron-star EOS. Isolated neutron stars are generally characterized by their mass, radius, and spin frequency. In binary pulsars, the spin-orbit coupling can also give information about the stars' moments of inertia. Atmospheric and crust properties are required to determine the behaviour of bursts, glitches, and other behaviour, and observations of such processes are more sensitive to aspects of neutron-star physics beyond the cold equation of state. Here we will focus instead on the properties that derive from the core equation of state, specifically those which are well-described by perfect fluid behaviour of cold high-density equilibrium matter.

2.1 Static, spherical stars

The simplest model of a neutron star is a spherically symmetric, nonrotating perfect fluid, supported against gravitational collapse by its pressure.

With a metric of the form

$$ds^2 = -e^{2\Phi(r)}dt^2 + e^{2\lambda(r)}dr^2 + r^2 d\Omega^2, \tag{2.1}$$

matter described by a perfect fluid stress energy tensor with four-velocity $u^\mu =$

$(-1/g_{00}, 0, 0, 0)$,

$$T^{\mu\nu} = -pg^{\mu\nu} + (p+\epsilon)u^\mu u^\nu, \tag{2.2}$$

and a given equation of state

$$\epsilon = \epsilon(p), \tag{2.3}$$

the stellar structure is determined by the Einstein equations in the form

$$\frac{dm}{dr} = 4\pi r^2 \epsilon \tag{2.4}$$

$$\frac{dp}{dr} = -\frac{(m + 4\pi r^3 p)(p+\epsilon)}{r^2(1-2m/r)} \tag{2.5}$$

$$\frac{d\Phi}{dr} = \frac{m + 4\pi r^3 p}{r^2(1-2m/r)} \tag{2.6}$$

Here $m(r)$ is defined via

$$e^{2\lambda} = \left(1 - \frac{2m}{r}\right)^{-1} \tag{2.7}$$

and is interpreted as the mass (including potential energy contributions) inside the circumferential radius r. These are known as the Tolman-Oppenheimer-Volkoff (TOV) equations [7].

A neutron star model can be defined by the choice of the central energy density, ϵ_c, which for a one-parameter equation of state fixes the central pressure $p_c = p(\epsilon_c)$. The remaining boundary condition at the centre is

$$m(r=0) = 0. \tag{2.8}$$

The surface is defined at the radius $r = R$ where $p = 0$, and we define a boundary condition on Φ via

$$m(r=R) = M \tag{2.9}$$

$$\Phi(r=R) = \frac{1}{2}\ln\left(1 - \frac{2M}{R}\right) \tag{2.10}$$

completing the specification of boundary conditions for m and Φ given a central $p(\epsilon_c)$.

Outside the surface, the metric is the vacuum Schwartzchild metric of mass M,

$$e^{2\Phi} = \left(1 - \frac{2M}{r}\right) \qquad (r > R) \tag{2.11}$$

$$e^{2\lambda} = \left(1 - \frac{2M}{r}\right)^{-1} \qquad (r > R). \tag{2.12}$$

The baryon mass A of the star is found by integrating the rest mass density ρ over the proper volume of the star

$$A = \int \rho dV = 4\pi \int_0^R \rho \frac{4\pi r^2}{\sqrt{1-2m/r}} dr. \tag{2.13}$$

2.1.1 Enthalpy

There are numerical challenges when solving the TOV equations in the form specified above. The radius at the edge of the star, R, is not known until the equations are solved, so some iteration procedure is required to seek the edge of the star, where p and ϵ become zero. Integrating in terms of pseudo-enthalpy H, instead of the radius, will have the advantage that the surface is at a known value $H = 0$ and the equations are nonsingular at this point [8].

A neutron star, at zero temperature, can be described by a one-parameter equation of state

$$\epsilon = \epsilon(n), \qquad p = p(n) \tag{2.14}$$

of energy density ϵ and pressure p in terms of baryon number density n or rest mass density $\rho = m_b n$. Recall that the first law of thermodynamics in the zero-temperature case is

$$d\epsilon = \frac{\epsilon + p}{\rho} d\rho \tag{2.15}$$

and that

$$h = \frac{\epsilon + p}{\rho} \tag{2.16}$$

is the comoving enthalpy per unit rest mass. The pseudo-enthalpy

$$H = \ln(h) \tag{2.17}$$

satisfies

$$\frac{dp}{dH} = \epsilon + p, \tag{2.18}$$

and using $(\epsilon + p)/\rho \to 1$ as $p \to 0$ we obtain

$$H = \int_0^p \frac{dp'}{\epsilon(p') + p'}. \tag{2.19}$$

For positive energy density and pressure, h is monotonically increasing with pressure, so we can convert an equation of state into the form

$$\epsilon = \epsilon(h), \qquad p = p(h). \tag{2.20}$$

Following Lindblom [8], we re-express Eq. (2.5), using Eq. (2.18) as

$$\frac{dH}{dr} = -\frac{m + 4\pi r^3 p(H)}{r(r - 2m)} \tag{2.21}$$

which, by comparison with equation (2.6), shows that

$$\frac{d\Phi}{dr} = -\frac{dH}{dr}. \tag{2.22}$$

Using the conditions $H = 0$ and $\Phi = \frac{1}{2}\ln\left(1 - \frac{2M}{R}\right)$ at the surface we have

$$\Phi = \frac{1}{2}\ln\left(1 - \frac{2M}{R}\right) - H \qquad (r < R). \tag{2.23}$$

The equations of stellar structure, (2.4) and (2.5), can then be written in terms of the pseudo-enthalpy as

$$\frac{dr}{dH} = -\frac{r(r - 2m)}{m + 4\pi r^3 p(H)} \tag{2.24}$$

$$\frac{dm}{dH} = 4\pi r^2 \epsilon \frac{dr}{dH}, \tag{2.25}$$

with $r = R$ and $m = M$ at $H = 0$; and the metric within the star is [recall $H = \ln(h)$]

$$ds^2 = -\frac{1}{h(r)^2}\left(1 - \frac{2M}{R}\right) dt^2 + \left(1 - \frac{2m(r)}{r}\right)^{-1} dr^2 + r^2 d\Omega^2. \tag{2.26}$$

The rest mass of the matter making up the neutron star, which is proportional to the number of the constituent baryons, is again determined by integrating the rest mass density in a comoving Lorentz frame, which can be written in terms of enthalpy as

$$\rho = \frac{p + \epsilon}{h}, \tag{2.27}$$

over the volume of the star.

2.1.2 Stability and maximum mass

A sequence of nonrotating models can be constructed for a given equation of state by varying central energy density ϵ_c. Although these solutions will satisfy hydrodynamic equilibrium, there is no guarantee that they will be *stable* solutions. The onset of instability determines the maximum mass possible for a given equation of state.

The stability to radial perturbations can be expressed in terms of the radial component of a Lagrangian displacement of the fluid $\xi(\mathbf{x}, t)$. These radial perturbations are decomposed into a set of orthonormal modes of oscillation with time dependence $\sim \exp(i\omega_j t)$. The eigenvalues ω_j^2 of these modes are real, forming a sequence $\omega_0^2 < \omega_1^2 < \omega_2^2 \cdots$, with the eigenfunction ξ_j of each mode having j nodes for $0 < r < R$ [4].

Overall stability is governed by the fundamental mode ξ_0, which has no nodes within $0 < r < R$. If this mode is stable, with $\omega_0^2 > 0$, then all modes are stable as their ω_i^2 must be larger than a positive quantity. If it is unstable, it is the fastest growing unstable mode, as ω_0^2 is the most negative.

We evaluate stability along a sequence of models characterized by ϵ_c. Assume stability is known at some low density. Consider a critical point where $dM/d\epsilon_c = 0$ is a local extremum. Then there exist two nearby equilibrium models which have the same energy M but different configurations. Let ξ be the Lagrangian displacement from the lower ϵ_c^L model to the higher ϵ_c^H model. Using the equations of motion for the ξ_j, one can show that $dM/d\epsilon_c = 0$ implies the existence of some ξ_i with $\omega_i^2 = 0$ linking the two equilibrium models [4].

Start with a low central energy density where a model is known to be stable, so all modes have positive ω_i^2. As the central energy density ϵ_c increases, the first critical point must indicate where the smallest eigenvalue ω_0^2 crosses zero. This is the onset of instability, as the the lowest fundamental mode ξ_0 is then unstable. However, further critical points may indicate either a return to stability, as ω_0^2 becomes positive again, or an extended set of unstable equilibrium models as higher normal modes become unstable.

The variation of the radius over the same ϵ_c-parameterized sequence of models determines whether stability to radial perturbations will change at later critical points. This can be shown as follows: As the central energy density is increasing, the mode ξ connecting the two models will be negative near the centre of the star (fluid elements contract). Then, if ξ is a mode with an even number of nodes, ξ will also be negative near the radius of the star, and the radius will decrease across the critical point. Conversely, if ξ has an odd number of nodes the radius will increase across the critical point.

Thus, after a stable region, a series of critical points with $dR/d\epsilon_c < 0$ will indicate

Figure 4 : Gravitational mass M, plotted vs central energy density ϵ as well as versus radius R. Critical points are labelled with letters in order of increasing central energy density.
Top panels: An equation of state with a phase transition, parameterized according to to Chapter 3 by $p_2 = 13.85$, $\Gamma_1 = 3$, $\Gamma_2 = 1.2$, $\Gamma_3 = 3$. A is a first maximum mass, B a minimum in mass, and C a second maximum mass. The change in radius over the critical points shows that there is a second stable sequence from B to C.
Bottom panels: In this EOS, a minimum mass at E indicates the onset of ξ_1 mode instability, rather than a second stable sequence, as seen by the change in radius R.

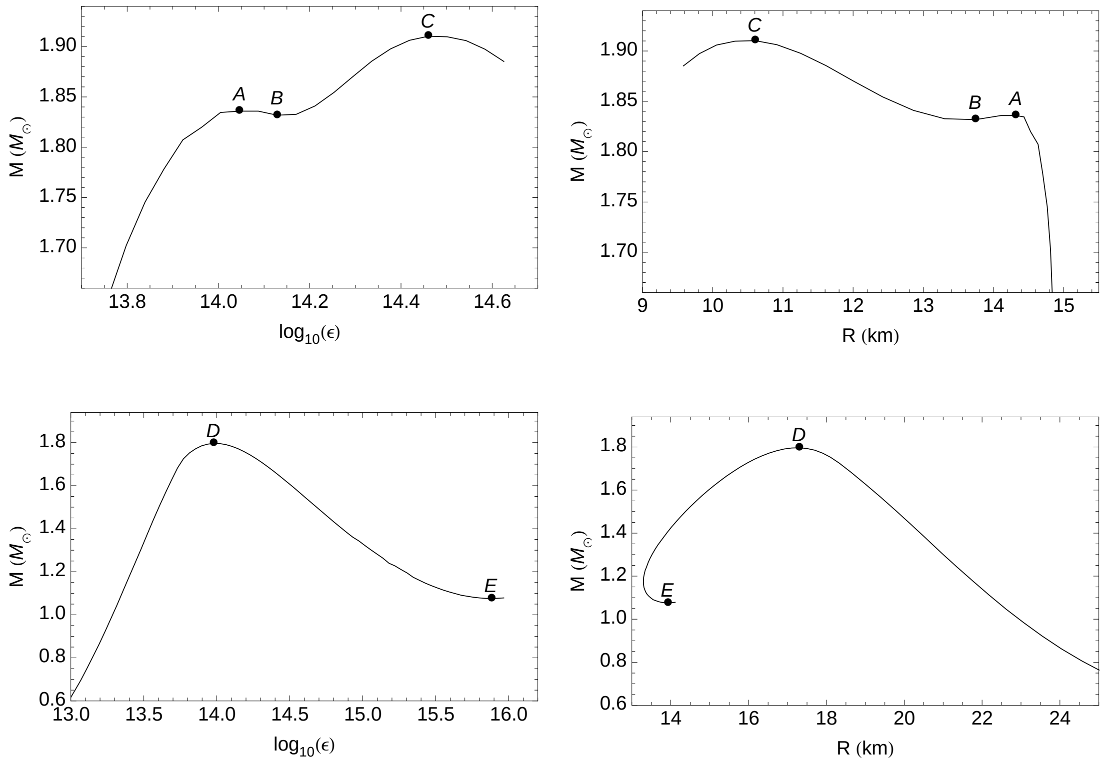

alternating regions of stability and instability the as fundamental mode, with zero nodes, crosses zero. The first critical point with $dR/d\epsilon_c > 0$, however, indicates the onset of instability of the ξ_1 mode.

This condition can be seen in the curve parameterized by ϵ_c in the M-R plane, rather than by considering M vs ϵ, as demonstrated in Fig. 4.

For the equation of state of cold degenerate matter, the first critical point is a maximum white dwarf mass, and the second critical point corresponds to the minimum neutron star mass. For most $npe\mu$-only equations of state, the third critical point is the maximum neutron star mass, and further critical points indicate additional unstable modes. However, equations of state with phase transitions to exotic forms of matter above nuclear density may have two stable branches of neutron stars [9].

To determine the absolute maximum stable mass for a given equation of state, a sequence of models must be constructed through possible regions of fundamental mode instability until higher modes also become unstable. For the set of realistic and parameterized equations of state considered, the onset of ξ_1 instability appears to be irrecoverable.

2.2 Slow Rotation

A formalism for slowly rotating neutron stars, with quantities expressed in orders of the angular velocity Ω, was developed by Hartle [10, 11]. It is valid for $\Omega \ll \Omega_K$, where Ω_K is the Kepler velocity of a particle in a circular orbit at the equator, $\Omega_K \sim (GM/R^3)^{1/2}$.

For the purposes of characterizing neutron star structure, we will consider the moment of inertia calculated for slowly rotating neutron stars at first order. This is reviewed nicely in [12]. Another equation of state dependent property of slowly rotating neutron stars is the quadrupole moment induced by the rotation, but this requires terms to second order in Ω and will not be considered in this thesis.

For slowly and uniformly rotating stars, the metric can be written in spherical coordinates as

$$ds^2 = -e^{2\Phi(r)}dt^2 + \left(1 - \frac{2m(r)}{r}\right)^{-1} dr^2 - 2\omega(r,\theta)r^2 \sin^2\theta dt d\phi + r^2\left(d\theta^2 + \sin^2\theta d\phi^2\right). \tag{2.28}$$

For a uniformly rotating configuration of angular velocity Ω, an observer falling freely from infinity gains an angular velocity $\omega(r,\theta)$. The difference $\bar{\omega}(r,\theta) = \Omega - \omega(r,\theta)$ is the coordinate angular velocity of the fluid element at (r,θ). The Einstein equations with the additional component in (2.28) require $\bar{\omega}$ to be a function of r alone, obeying the differential equation.

$$\frac{1}{r^4}\frac{d}{dr}\left(r^4 j \frac{d\bar{\omega}}{dr}\right) + \frac{4}{r}\frac{dj}{dr}\bar{\omega} = 0 \tag{2.29}$$

with

$$j(r) = \sqrt{1 - 2m(r)/r} \tag{2.30}$$

and $d\bar{\omega}/dr = 0$ at $r = 0$. This equation for $\bar{\omega}$ is the only addition, at order Ω, to Eqs. (2.6) and (2.5) of the spherical case.

Matching the interior solution to the metric outside the star, where $\omega = 2J/r^3$ or

$$\bar{\omega}(r) = \Omega - \frac{2J}{r^3}, \tag{2.31}$$

gives the condition

$$J = \frac{1}{6}R^4 \left(\frac{d\bar{\omega}}{dr}\right)_{r=R} \tag{2.32}$$

which supplies the second boundary condition on the differential equation (2.29) for $\bar{\omega}$:

$$\frac{\bar{\omega}}{\Omega}\bigg|_{r=R} = 1 - \frac{R}{3}\left(\frac{d\left(\bar{\omega}/\Omega\right)}{dr}\right)_{r=R}. \tag{2.33}$$

The moment of inertia is then $I = J/\Omega$, a quantity independent of Ω in the slow-rotation approximation.

2.2.1 Moment of inertia using enthalpy

In terms of enthalpy, j can be rewritten using Eqs. (2.30) and (2.23) as

$$j(r) = \left(\frac{1 - 2m/r}{1 - 2M/R}\right)^{1/2} e^H \tag{2.34}$$

so that, after substituting in dm/dr and dh/dr, we find that j satisfies

$$\frac{dj}{dr} = -j\frac{4\pi r^3(p + \epsilon)}{r(r - 2m)} \tag{2.35}$$

We can then rewrite (2.29) in terms of H as a pair of first order equations, defining

$$\frac{d\overline{\omega}}{dr} = \alpha \tag{2.36}$$

and then substituting α for $d\bar{\omega}/dr$ and using (2.35) for dj/dr in (2.29), then solving for $d\alpha/dr$, we find

$$\frac{d\alpha}{dr} = -\frac{4\alpha}{r} - (r\alpha + 4\frac{\bar{\omega}}{r})\frac{4\pi(\epsilon + p)}{1 - 2m/r}. \tag{2.37}$$

The boundary condition $d\bar{\omega}/dr = 0$ becomes $\alpha = 0$ at the central value of the enthalpy h_c, where $r = 0$. The boundary condition at the surface, (2.33), becomes

$$\bar{\omega}(R) = \Omega - \frac{R}{3}\alpha(R). \tag{2.38}$$

The angular momentum J and angular velocity Ω of the solution will be

$$J = \frac{1}{6}R^4\alpha(R) \tag{2.39}$$

$$\Omega = \overline{\omega}(R) + \frac{2J}{R^3}, \tag{2.40}$$

which determines the Ω-independent the moment of inertia I, for any $\bar{\omega}(R)$ in the slow-rotation approximation, via

$$I = \frac{J}{\Omega}. \tag{2.41}$$

This formalism allows the characterizing properties of mass, baryon mass, radius, and slowly-rotating moment of inertia to all be written in terms of a system of first order differential equations in h, which can be simultaneously solved using standard numerical routines for a given equation of state $p(h)$, $\epsilon(h)$:

$$\frac{dr}{dH} = -\frac{r(r-2m)}{m+4\pi r^3 p(H)} \tag{2.42}$$

$$\frac{dm}{dH} = 4\pi r^2 \epsilon \frac{dr}{dH} \tag{2.43}$$

$$\frac{dm_b}{dH} = (p+\epsilon)e^{-h}\frac{4\pi r^2}{\sqrt{1-2m/r}}\frac{dr}{dH} \tag{2.44}$$

$$\frac{d\overline{\omega}}{dr} = \alpha\frac{dr}{dH} \tag{2.45}$$

$$\frac{d\alpha}{dr} = \left(-\frac{4\alpha}{r} + \frac{4\pi(\epsilon+p)(r\alpha+4\overline{\omega})}{1-2m/r}\right)\frac{dr}{dH}. \tag{2.46}$$

This system can be solved numerically, after specifying boundary conditions at the centre via a small uniform-density ball.

2.3 Fast Rotation

As Ω increases, a rotating neutron star eventually reaches a mass-shed limit. This is the point at which the neutron star is rotating sufficiently rapidly that matter at the surface becomes gravitationally unbound. It can be found by calculating the Kepler velocity Ω_K of an equatorial particle and comparing it to the angular velocity Ω of the star; the two are equal at the mass-shed limit.

Although most neutron stars rotate slowly enough that the slow rotation approximation is valid, some nascent neutron stars, and some in x-ray binaries spun up by accreting matter from the companion star, may rotate with angular velocities near Ω_K. For these maximal rotations, the approximation of slow rotation, by its definition, breaks down. However, we can still consider uniform rotation to be a good approximation for long-lived but quickly rotating neutron stars.

To determine the properties of uniformly rotating stars of arbitrary rotation, numerical solutions must be calculated. For work discussed in this thesis, the open-source code `rns` [13] was used, in the updated form `rns2.0` [14]. Other methods are reviewed in [15, 16, 17].

The `rns` code sets up central conditions for a stellar model based on ϵ_c, and uses a nonrotating solution as an initial model. Rotating models are specified using the axis ratio $\mathfrak{r}$ between equatorial and polar axes. Models are restricted to axisymmetric, uniformly rotating neutron stars.

The Einstein equations are solved using the method of Komatsu, Eriguchi, and Hachisu (KEH) [18], where one splits off a flat-space Laplacian operator iterating over the remaining nonlinearities. A similar method will be discussed in PartII for the construction of binary neutron star initial data.

Given a model specified by ϵ_c and $\mathfrak{r}$, a convergent solution of the Einstein equations is characterized by various equilibrium properties calculated in `rns`, including: gravitational mass, baryonic mass, equatorial radius, angular momentum, moment of inertia, angular velocity, and Kepler velocity.

2.3.1 Stability and maximum rotation

The equilibrium rotating models for a given cold equation of state form a two-parameter family, which can be specified by the central energy density ϵ_c and the axis ratio $\mathfrak{r}$, as in the base `rns` routine, or equivalently by ϵ_c and the angular velocity Ω. In the limit that $\Omega \to 0$ and thus $\mathfrak{r} \to 1$, we recover the one-parameter family of nonrotating spherical models.

The mass-shed limit gives a maximally rotating equilibrium model for each central energy density ϵ_c, but, as in the spherical case, these equilibrium models are not

Figure 5 : Two families of equilibrium rotating neutron stars, plotted as surfaces of baryon mass M_b for a given central energy density ϵ and angular momentum J. A maximum angular momentum model is reached, for a given ϵ, at the mass-shed limit. Stability can be determined by considering critical points of M_b along sequences of constant J, as in the spherical, or $J = 0$, limit. For the EOS on the left, there is one stable limit, and the maximum rotation model is very close to the maximum mass model on the mass-shed limit sequence. For the EOS on the right, there are two stable regions along each line of constant J, comparable to the two stable regions of the first EOS in Fig. 4. As frequency of rotation increases along the mass-shed limit, the maximum rotation model will lie in the second stable region, which has higher central density than the maximum mass model in the first stable region.

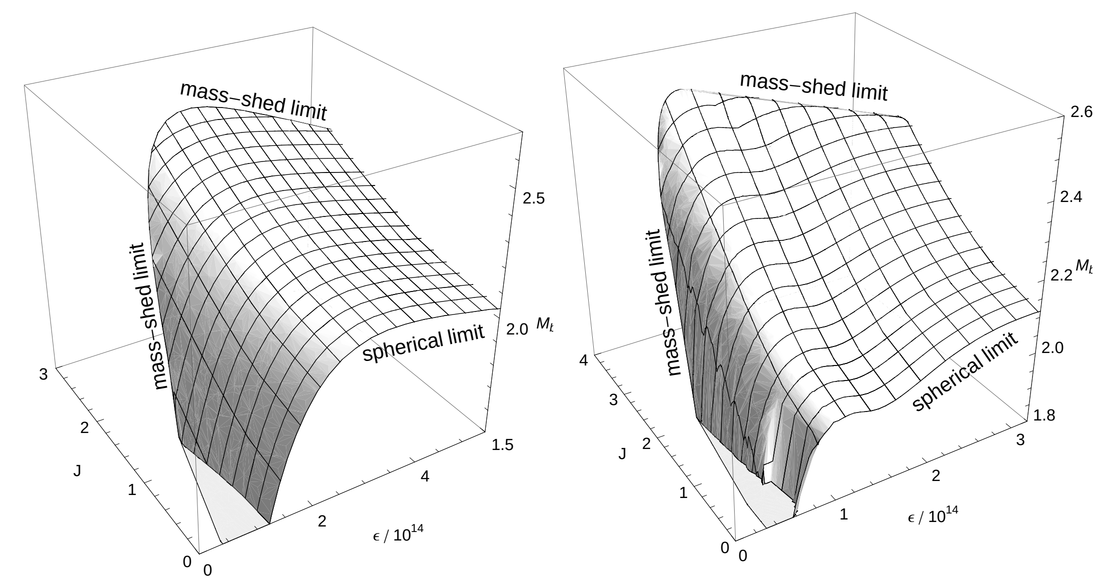

guaranteed to be stable to perturbations.

Overall stability in uniformly rotating models is governed, as in the nonrotating limit, by the stability of the model to radial perturbations. As in the spherical $\Omega = 0$ case, there can exist alternating regions of stable and unstable rotating models along a sequence of fixed Ω. A criterion for the onset of instability is developed by Friedman, Ipser and Sorkin in [19].

The critical points that potentially indicate a change in stability are extrema of mass-energy M under variation in both baryon mass M_b and angular momentum J.

The model of maximum rotation is the fastest-spinning stable member of the mass-shed limit models. For most $npe\mu$-only equations of state, this is close to the point on the mass-shed limit with maximal mass-energy. However, especially in cases with phase transitions or two stable branches of neutron stars, this is not necessarily true. An example is in EOS L of [15], or the parameterized EOS of Fig. 5.

Universally valid searches for limiting stability, as in for example [15], have required covering the set of models with sequences of constant rest mass M_b and extremizing J on each one, or vice versa. However it is possible to obtain a more general criteria for critical points.

To obtain a more general stability condition, consider the two-parameter family of rotating neutron stars as a surface Σ in M_b-J-ϵ_c space, like that shown in Fig. 5. The central energy density ϵ_c and axis ratio $\mathfrak{r}$ are suitable parameters for this surface.

This surface has folds, the tops of which are the maxima of baryon mass M_b along sequences of constant J (or of J along sequences of constant M_b). If projected onto the M_b-J plane, these folds give the boundaries of a family of equilibrium models. These are the analogs of the $dM = 0$ critical points in the $J = 0$ spherical case.

The set of models with limiting stability, the "critical line", is thus the set where a vector in the ϵ_c direction, $\widehat{\boldsymbol{\epsilon}_c}$, is tangent to the surface of equilibrium models. Equivalently, this is where the normal vector to the surface is perpendicular to $\widehat{\boldsymbol{\epsilon}_c}$.

Given the parameterization of the surface in terms of ϵ_c and $\mathfrak{r}$, the normal vector to the surface $\boldsymbol{\Sigma} = \{M_b, J, \epsilon_c\}$ is along

$$\boldsymbol{n} = \frac{\partial \boldsymbol{\Sigma}}{\partial \epsilon_c} \times \frac{\partial \boldsymbol{\Sigma}}{\partial \mathfrak{r}} \tag{2.47}$$

with component along $\widehat{\boldsymbol{\epsilon}_c}$.

$$n_{\epsilon_c} = \frac{\partial M_b}{\partial \epsilon_c}\frac{\partial J}{\partial \mathfrak{r}} - \frac{\partial J}{\partial \epsilon_c}\frac{\partial M_b}{\partial \mathfrak{r}} \tag{2.48}$$

which is zero at the critical line between stable and unstable equilibriums on the surface $\boldsymbol{\Sigma}$.

This condition could also be described as point where M_b and J as functions over ϵ_c and $\mathfrak{r}$ have parallel gradients; this means that the condition of [19], that $dJ/d\lambda = 0$ along a sequence of constant M_b, will hold; nearby models have the same properties at the critical line. As in the spherical case, there may be multiple stable and unstable regions of the equilibrium fluid configurations.

The maximally rotating model for a given equation of state may be found by considering a sequence of central energy densities ϵ_c. First, increase the axis ratio $\mathfrak{r}$ until the Kepler limit is found, as in the example program `main.c` of `rnsv2.0`. Second, vary ϵ_c and $\mathtt{r}$ around this point to estimate the partial derivatives of Eq. 2.48. The sign of n_{ϵ_c} will change as the Kepler limit sequence crosses the stability limit.

A critical point along a constant J sequence may indicate not a new stable region, but the onset of higher mode instability (as in the spherical case of Fig. 4). One can generalize the radial change condition of spherically symmetric stars to differentiate two-branch EOS from the onset of further instabilities, as pseudo-radial perturbations do characterize this stability, but this has not been shown in detail.

For equations of state with two stable regions, the Kepler limit models may show a maximum mass near the first critical point, but a maximum rotation near a second critical point with smaller mass but substantially larger angular velocity; this is the behaviour of EOS L in [15] and the parameterized EOS in Fig. 5.

An empirical formula, developed by Haensel and Zdunik in [20], predicts maximum stable rotation for a given EOS from the maximum-mass spherically symmetric model for that EOS of mass M_s and radius R_s:

$$\left(\frac{\Omega_{max}}{10^4\,\mathrm{s}^{-1}}\right) \approx \kappa \left(\frac{M_s}{M_\odot}\right)^{\frac{1}{2}} \left(\frac{R_s}{10\,\mathrm{km}}\right)^{-\frac{3}{2}} \tag{2.49}$$

The original calculation of Haensel and Zdunik gave $\kappa = 0.77$. An overview of subsequent calculations is given by Haensel et al. in [21], reporting values of $\kappa = 0.76$–0.79 for a range of EOS sets and calculation methods including those of [22, 23, 15]. If we calculate maximum rotations with `rns` as described above, over a the full range of parameters considered for the parameterized EOS of Chapter 3, we find $\kappa = 0.79 \pm 0.03$.

Chapter 3

Piecewise polytrope parameterization

3.1 Introduction

Studies of astrophysical constraints (see, for example, [24, 25, 26, 27, 28] and references therein) present constraints by dividing the EOS candidates into an allowed and a ruled-out list.

Our goal is to find a parameterized EOS for which the number of parameters is smaller than the number of astrophysical observables that might constrain them. At the same time, the number of parameters must be large enough that a point in parameter space can accurately characterize the true EOS of neutron star matter. We test such a parametrization by finding the accuracy with which it can fit a large, representative collection of tabulated candidate EOS. An accurate parameterization will reproduce the neutron star characteristics of the candidate EOS, such as allowed neutron star masses, to an accuracy comparable with, or better than, astrophysical measurement.

With the parameterization fixed, each observational constraint becomes a restriction to a subset of the parameter space. The work reported here shows the regions of our parameter space allowed by causality and by current astrophysical observations; it also shows the implied restrictions on the parameter space of possible future observations.

The parameterization developed is based on a few polytropic regions of constant adiabatic index. Similar piecewise-polytropic equation of state have been considered by Vuille and Ipser [29]; and, with different motivation, several other authors [30, 31, 32, 33] have used piecewise polytropes to approximate neutron star EOS.

3.2 Candidates

We consider a wide array of equations of state, covering many different generation methods and potential species. For plain $npe\mu$ nuclear matter, we include

- two potential method EOS (PAL[34] and SLY4[6]),
- eight variational method (four APR variants[35], FPS[36], and three WFF variants[37]),
- one relativistic (BBB2[38]) and three relativistic (BPAL12[39], ENGVIK[40] and MPA1[41]), Brueckner-Hartree-Fock EOS, and
- four relativistic mean field theory EOS (3 MS variants[42] and PRAKDAT[43]).

We also consider models with exotica such as hyperons, mesons, and quarks, collectively referred to as $K/\pi/H/q$ EOS.

- one neutron-only EOS with pion condensates (PS[44]),
- two relativistic mean field theory EOS with kaons (two SCHAF variants [45]),
- one effective potential EOS including hyperons (BALBN1H1 [46]),
- four relativistic mean field theory EOS with hyperons (GLENDNH3[47] and three GM.NPH variants[43]),
- one relativistic mean field theory EOS with hyperons and quarks (PCL_NPHQ [48]), and
- four hybrid EOS with mixed APR nuclear matter and colour-flavor-locked quark matter (ALF* [49]).

These candidate EOS are described in more detail in Appendix A. The tables are plotted in Fig. 6 to give an idea of the range of equations of state considered for this parameterization.

Figure 6 : Pressure versus rest mass density for the set of candidate equation of state tables considered in the parameterization

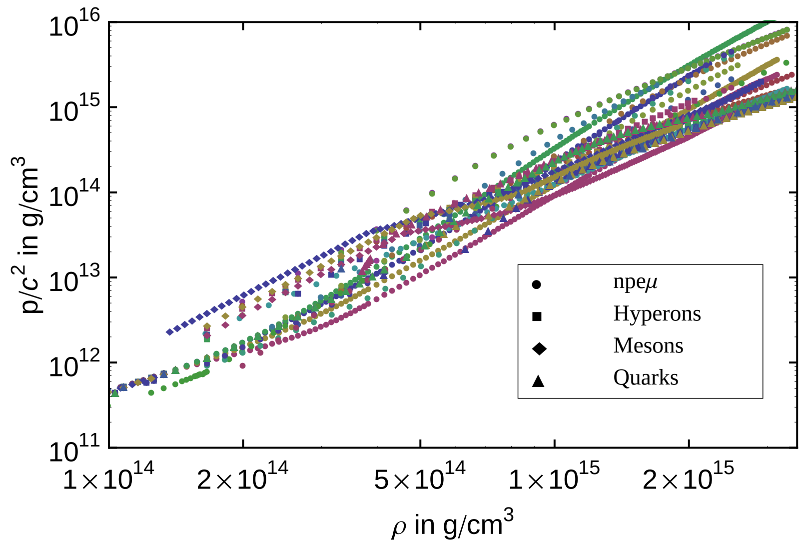

3.3 Piecewise Polytropes

A polytropic EOS has the form

$$p(\rho) = K\rho^{\Gamma} \tag{3.1}$$

for pressure p as a function of the rest-mass density ρ, in terms of the two constants K and Γ. The constant Γ is the adiabatic index. The energy density ϵ is fixed by the first law of thermodynamics,

$$d\frac{\epsilon}{\rho} = -p\ d\frac{1}{\rho}. \tag{3.2}$$

For p of the form (3.1), Eq. (3.2), has the immediate integral when $\Gamma > 1$ of

$$\frac{\epsilon}{\rho} = (1+a) + \frac{1}{\Gamma - 1}\frac{p}{\rho}, \tag{3.3}$$

where a is a constant; and the requirement $\lim\limits_{p\to 0}\dfrac{\epsilon}{\rho} = 1$ implies $a = 0$ and the standard relation

$$\epsilon = \rho + \frac{1}{\Gamma - 1}p. \tag{3.4}$$

A polytropic index N is defined by $N = 1/(\Gamma - 1)$.

The parameterized EOS we consider are piecewise continuous polytropes above a density ρ_0, satisfying Eqs. (3.1) and (3.3) on a sequence of density intervals, each with its own K_i and Γ_i: An EOS is piecewise polytropic for $\rho \geq \rho_0$ if, for a set of dividing densities $\rho_0 < \rho_1 < \rho_2 < \cdots$, the pressure and energy density are everywhere continuous and satisfy

$$p(\rho) = K_i \rho^{\Gamma_i}, \quad d\frac{\epsilon}{\rho} = -p\, d\frac{1}{\rho}, \quad \rho_i \leq \rho \leq \rho_{i+1}. \tag{3.5}$$

Then, for $\Gamma \neq 1$,

$$\epsilon(\rho) = (1 + a_i)\rho + \frac{K_i}{\Gamma_i - 1}\rho^{\Gamma_i} \tag{3.6}$$

with

$$a_i = \frac{\epsilon(\rho_i)}{\rho_i} - 1 - \frac{K_i}{\Gamma_i - 1}\rho_i^{\Gamma_i - 1}. \tag{3.7}$$

In each region $\rho_i \leq \rho \leq \rho_{i+1}$, the enthalpy h is defined as $(\epsilon + p)/\rho$ and is given by

$$h_i(\rho) = 1 + a_i + \frac{\Gamma_i}{\Gamma_i - 1} K_i \rho^{\Gamma_i - 1} \tag{3.8}$$

The internal energy $e = \epsilon/\rho - 1$ is then

$$e_i(\rho) = a_i + \frac{K_i}{\Gamma_i - 1}\rho^{\Gamma_i - 1} \tag{3.9}$$

and the sound velocity $v_s = dp/d\epsilon$ is

$$v_{s,i}(\rho) = \sqrt{\frac{\Gamma_i K_i \rho^{\Gamma_i - 1}}{h(\rho)}} \tag{3.10}$$

In general, each region of a piecewise polytrope equation of state is specified by three parameters: the initial density ρ_i, the coefficient K_i, and the adiabatic index Γ_i. However, when the equation of state at lower density has already been specified up to the chosen ρ_i, continuity of pressure restricts K_i to be

$$K_i = \frac{p(\rho_i)}{{\rho_i}^{\Gamma_i}} \tag{3.11}$$

Thus each additional region requires only two additional parameters, ρ_i and Γ_i. Furthermore, if the initial density of a region is chosen to be a fixed value for the parameterization, the region requires only a single additional parameter.

3.3.1 Fitting methods

We assume a fixed crust equation of state that can be extended arbitrarily to a fitted initial density ρ_1 where the core stiffening begins. The low-density EOS used is a piecewise-polytrope fit to the SLY4 equation of state. If the low density equation of state is based on a fit to a table other than SLY4, best fit parameters for the EOS change slightly, but much less than the typical difference in best-fit parameters for different candidates.

Fits to the high-density equation of state are done using points above $\rho = 10^{14.3}\mathrm{g/cm}^3 = 0.74\rho_{\mathrm{nuc}}$. If the best fit core EOS is of sufficiently high pressure that it lies above the low density equation of state at $0.74\rho_{\mathrm{nuc}}$, the lowest polytropic piece is extended back towards lower densities until it intersects the low density equation of state, where the two are matched together. Similarly, if the best fit core EOS has smaller pressure than the crust EOS at $0.74\rho_{\mathrm{nuc}}$, the crust EOS is extend forward until it intersects the first matched polytrope piece. This gives monotonically increasing equations of state, with no additional parameters required for matching.

For each tabled equation of state, the central rest mass density of the maximum mass TOV star is used as an upper limit on the points considered for the fit. This ignores tabled points which will not be realized in physical neutron stars.

The `MINPACK` nonlinear least-squares routine `LMDIF`, based on the Levenberg-Marquardt algorithm, is used to minimize the sum of squares of the difference between the logarithm of the pressure-density points in the specified density range and the logarithm of the piecewise polytrope formula, which is a linear fit in each region after the logarithms have been taken.

Even with a robust algorithm, the nonlinear fitting with varying dividing densities is sensitive to initial conditions. Multiple initial parameters for free fits are constructed using fixed-region fits of several possible dividing densities, and the global minimum of the resulting residuals is taken to indicate the best fit for the candidate equation of state.

For the set or parameters $\{\rho_i, K_i, \Gamma_i\}$ which define a piecewise polytrope model $p(\rho)$, we report the root mean square or RMS residual of the fit to m tabled points

ρ_j, p_j:

$$\text{residual} = \sqrt{\frac{1}{m}\sum_{j=1}^{m}\{\log_{10}(p_j/p(\rho_j))\}^2} \tag{3.12}$$

We begin with a single polytropic region in the core, specified by the two parameters ρ_1 and Γ_1, with K_1 fixed as in Eq. (3.11). This is referred to as a one free piece fit. We consider also two polytropic regions within the core, which are specified with the four parameters $\{\rho_1, \Gamma_1, \rho_2, \Gamma_2\}$, as well three polytropic regions specified by the six parameters $\{\rho_1, \Gamma_1, \rho_2, \Gamma_2, \rho_3, \Gamma_3\}$. While some equations of state are well approximated with a single high-density polytrope, others require three pieces to accurately capture the behaviour of phase transitions at high density.

The six parameters required to specify three free polytrope pieces seems to push the bounds of what may be reasonably constrained by a small set of astrophysical measurements. We can reduce the number of parameters by fixing the densities which delimit the polytropic regions within the core. A three fixed piece fit, using three polytropic regions but with fixed $\rho_2 = 10^{14.65}\,\mathrm{g/cm^3}$ and $\rho_3 = 10^{15.05}\,\mathrm{g/cm^3}$, is specified by the four parameters ρ_1, Γ_1, Γ_2, and Γ_3. The choice of ρ_2 and ρ_3 is discussed in Sec. 3.3.3. Note that the density ρ_1 of departure from the fixed low-density equation of state is still fitted by this scheme, although we later re-express this degree of freedom as p_2, the pressure at ρ_2, using

$$p_2 = p_{\mathrm{crust}}(\rho_1)\left(\frac{\rho_2}{\rho_1}\right)^{\Gamma_1} \tag{3.13}$$

Below nuclear density

The equation of state below nuclear density is well-approximated (residual < 0.03 between $\rho = 10^3\,\mathrm{g/cm^3}$ and $\rho = 10^{14}\,\mathrm{g/cm^3}$) by four polytrope pieces, as given in Table 2. Roughly, the four regions correspond to nonrelativistic electron gas, relativistic electron gas, neutron drip, and from neutron drip to nuclear density. We will fix the crust EOS to this parameterization. Modelling a neutron star with a different crust, from realistic tables or fits to these tables, leads to changes in neutron-star properties such as radius of a few percent.

Table 2 : Crust EOS fit from SLY4 table below nuclear density. Polytropes from these tables yield p/c^2 in units of g/cm^3, given ρ in units ofg/cm^3. K_i does not have consistent units, Γ_i is dimensionless, and ρ_i is in g/cm^3. Figures are given to accuracy used in the neutron star structure calculations.

K_i	Γ_i	ρ_i
6.80109613e−09	1.58424999	0
1.06186086e−06	1.28732904	2.44033979e+07
5.32696797e+01	0.62223344	3.78358138e+11
3.99873692e−08	1.35692395	2.62780487e+12

3.3.2 Best fits to candidate EOS

Table 3 shows average and maximum RMS residuals over the set of 31 candidate equations of state for the three types of fit discussed in Sec. 3.3.1.

The hybrid quark EOS ALFC, which incorporates a QCD correction parameter for quark interaction, is the worst-fit table for the one piece fit, three piece fixed region fit, and three piece varying region fit. It has a residual from the two piece fit of 0.0438, somewhat less than the worst fit EOS, BALBN1H1, an effective potential EOS which includes all possible hyperons and has a two piece fit residual of 0.0555.

For equations of state without exotica such as hyperons, kaons, or quark matter, the four-parameter fit of two free polytrope pieces models the behaviour of candidates well. However, equations of state with exotica are not well fit by this type of analytic equation of state. Many require three polytrope pieces to capture the stiffening around nuclear density, a softer phase transition, and then final stiffening. The six parameters required to specify three free polytrope pieces seems to push the bounds of what may be reasonably constrained by a small set of astrophysical measurements. However, another four parameter fit can be made to all equations of state if the transition densities are held fixed for all candidate equations of state. The choice of fixed transition densities, and the advantages of such a parameterization over the two free piece fit, are discussed in the next section.

Table 3 : Average residuals resulting from fitting the set of candidate EOS with various types of piecewise polytropes. Free fits allow dividing densities between pieces to vary. The fixed three piece fit uses $10^{14.7}$ g/cm^3 or roughly $1.85\rho_{\rm nuc}$ and 10^{15} g/cm^3 or $3.70\rho_{\rm nuc}$ for all EOS. Tabled are the RMS residuals of the best fits averaged over the set of candidates. The set of 31 candidates includes 18 candidates containing only $npe\mu$ matter and 13 candidates with exotica such as hyperons, mesons, and/or quark matter. Fits are made to tabled points in the high density region between $10^{14.3}$ g/cm^3 or $0.74\rho_{\rm nuc}$ and the central density of a maximum mass TOV star calculated using that table.

Type of fit	All	$npe\mu$	$K/\pi/h/q$
Mean RMS residual			
One free piece	0.0388	0.0285	0.0538
Two free pieces	0.0156	0.0087	0.0258
Three fixed pieces	0.0134	0.0096	0.0189
Three free pieces	0.0076	0.0054	0.0107
Standard deviation of RMS residual			
One free piece	0.0224	0.0157	0.0223
Two free pieces	0.0153	0.0059	0.0187
Three fixed pieces	0.0108	0.0062	0.0134
Three free pieces	0.0084	0.0039	0.0116

3.3.3 Fixed region fit

A good fit with minimal number of parameters is found for three regions with a division between first and second piece fixed at $\rho_2 = 10^{14.7}\,{\rm g/cm^3}$ and a division between second and third piece fixed at $\rho_3 = 10^{15.0}\,{\rm g/cm^3}$. The equation of state is specified by choosing the adiabatic indices $\{\Gamma_1, \Gamma_2, \Gamma_3\}$ in each region, and the density of departure from the fixed crust equation of state ρ_1.

With this scheme, best fit parameters for each considered equation of state tables give a residual of 0.04 or better, with the average residual over 31 candidate EOS of 0.013.

For a range of candidate dividing density choices varying both the lower dividing point ρ_2 and the higher dividing point ρ_3, three fixed region four-parameter fits were made to each of a set of 31 equation of state tables, and the RMS residuals of the fits calculated. The dividing densities were chosen to minimize the average RMS residuals over the set of candidate equations of state, as plotted in Fig. 7. For two

Figure 7 : Considering subsets of EOS with and without exotica shows a fairly robust choice of dividing densities. A mean of residuals over a set of candidate EOS are plotted for variations in dividing density. The left three curves show mean residual for varying ρ_2, as ρ_3 is fixed at 10^{15} g/cm^3. The right three curves show mean residual for varying dividing ρ_3, as ρ_2 is fixed at $10^{14.7}$ g/cm^3.

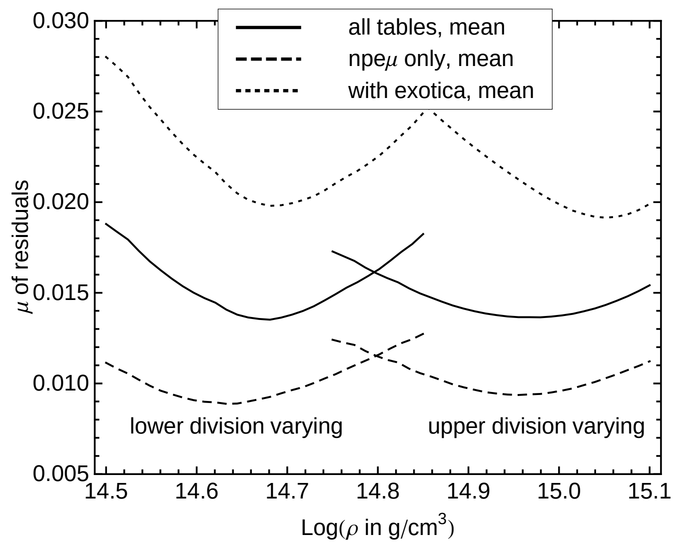

dividing densities, this is a two-dimensional minimization problem, which was solved by alternating between minimizing average RMS residual for upper or lower density while holding the other density fixed. The location of the best dividing points is fairly robust over the subclasses of equations of state.

For fixed crust equation of state, the parameter ρ_1 can be reinterpreted as specifying an overall pressure shift for an equation of state with given Γ_1, Γ_2, and Γ_3. Instead of ρ_1, pressure at any given density can be used to specify the fixed region piecewise polytrope in the core.

In this case, the pressure at $\rho_2 = 1.85\rho_{\rm nuc}$ was chosen to anchor the high-density equation of state, as empirical work by Lattimer and Prakash [25] indicates that pressure near this density determines the radius of $1.4M_{.}$ neutron stars, and thus may have a more direct relation to astrophysical properties and inspiral dynamics of neutron-stars near this mass. As this is the pressure at the start of the second interval, we refer to it as p_2. It is given in terms of fit parameters in Eq. (3.13).

The following considerations dictate our choice of the four-parameter space associated with three polytropic pieces with two fixed dividing densities. First, as mentioned above, we regard the additional two parameters needed for three free pieces as too great a price to pay for the moderate increase in accuracy. The comparison, then, is between two four-parameter spaces: polytropes with two free pieces and polytropes with three pieces and fixed dividing densities.

Here there are two key differences. Observations of pulsars that are not accreting are observations of stars with masses below 1.45 $M_\odot$, and the central density of these stars is below ρ_2 for almost all equations of state; then only the three parameters $\{p_2, \Gamma_1, \Gamma_2\}$ of the fixed piece parameterization are required to specify the equation of state for moderate mass neutron stars. This class of observations can then be treated as a set of constraints on a 3-dimensional parameter space. Similarly, because maximum-mass neutron stars ordinarily have most matter in regions with densities greater than the first dividing density, their structure is insensitive to the first adiabatic index. The three piece parametrization does a significantly better job above ρ_2 because phase transitions above that density require a third polytropic index Γ_3; if the remaining three parameters can be determined by pulsar observations, then observations of more massive, accreting stars can constrain Γ_3.

The best fit parameter values are shown in Fig. 8. The worst fits of the fixed region fit are the hybrid quark EOS ALFC and ALF1, and the hyperon-incorporating EOS BALBN1H1. For BALBN1H1, the relatively large residual is due to the fact that the best fit dividing densities of BALBN1H1 differ strongly from the average best dividing densities. Although BALBN1H1 is well fit by three pieces with floating densities, the reduction to a four-parameter fit limits the resolution of equations of state with such structure. The hybrid quark equations of state, however, have more complex structure that is difficult to resolve accurately with a small number of polytropic pieces. Still, the best-fit polytrope EOS is able to reproduce the neutron star properties predicted by the hybrid quark EOS.

In Appendix B, Table 13 shows the various neutron star structure characteristics, calculated according to Chapter 2, compared to the values of the best-fit piecewise polytrope parameterization for the core. Table 4 below lists average differences between observables for models computed with a candidate EOS and for models computed with the corresponding best-fit three-fixed-region EOS.

Table 4 : Average % difference between observables calculated using tabulated EOS and with the corresponding parameterized EOS. $M_{\max}$ is the maximum nonrotating mass configuration. $z_{\max}$ is the corresponding maximum gravitational redshift. $f_{\max}$ is the maximum rotation frequency from the Haensel-Zdunik empirical formula with updated coefficient. $R_{1.4}$ is the radius of a 1.4 $M_\odot$ star in units of km. $I_{1.338}$ is the moment of inertia for a 1.338 $M_\odot$ star in units of 10^{45} g cm^2. $v_{s,\max}$ is the maximum adiabatic speed of sound below the central density of the maximum mass neutron star.

$M_{\max}$	$z_{\max}$	$f_{\max}$	$R_{1.4}$	$I_{1.338}$	$v_{s,\max}$
0.99	2.01	1.98	1.25	1.63	5.58

Figure 8 : Parameterized EOS fits to the set of 31 candidate EOS tables. $\Gamma_2 < 3.5$ and $\Gamma_3 < 2.5$ for all equations of state with exotica. As discussed in the text, the shaded region corresponds to core equations of which do not match continuously onto the fixed crust.

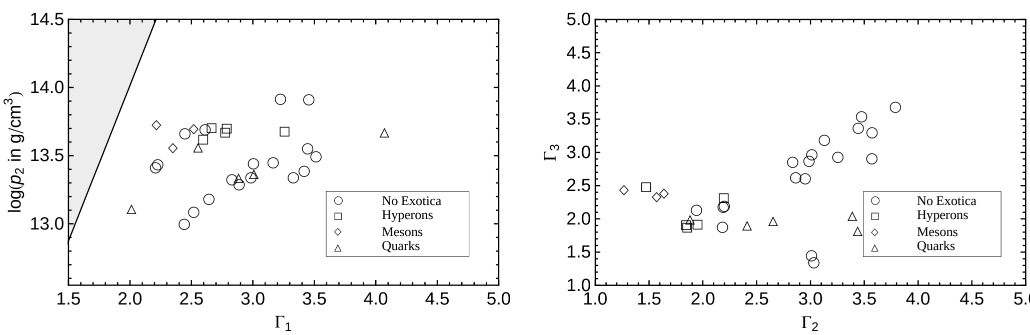

3.4 Constraining EOS parameters with astrophysical observations

Given this fixed-region parameterization, we can whittle down the allowed parameter space with constraints from neutron-star observations. We will examine constraints related to the mass configuration: causality below the central density of the maximum mass star, maximum mass, maximum gravitational redshift, and maximum spin frequency respectively. We will then examine constraints from possible future observations: the simultaneous measurement of mass and moment of inertia, and mass and radius. Finally we will combine the constraints from causality, maximum mass, and a future moment of inertia measurement.

In the discussion below we consider a range of parameters that includes the best fits to all 31 tabulated equations of state considered above: $10^{12.55}\,\mathrm{g/cm^3} < p_2 < 10^{14.5}\,\mathrm{g/cm^3}$, $1.4 < \Gamma_1 < 5.0$, $1.0 < \Gamma_2 < 5.0$, and $1.0 < \Gamma_3 < 5.0$. This parameter space is the region displayed in Fig. 8.

The shaded region corresponds to parameter values that generate a core EOS which does not connect with the fixed crust equation of state. This occurs when the adiabatic index Γ_1 is small and the pressure p_2 is large, so that the pressure in the parameterized core EOS, when extended back to low densities, is always greater than that of the fixed crust equation of state specified in Sec. 3.3.1.

Equations of state with large variation in adiabatic index can lead to the existence of a separate sequence of stable stars above the maximum central density for the normal neutron star sequence but overlapping in mass range. This behaviour is seen in models considered by Glendenning and Kettner [9], and similar behaviour is exhibited in work by Bejger et al. [31] and Zdunik et al. [30] in models based on piecewise polytrope equations of state used to model phase transitions. A discussion of the stability of such sequences is given in Sec. 2.1.2.

With the fixed-region parameterized EOS, two stable neutron-star sequences can exist when Γ_2 is less than ~ 2 and Γ_1 and Γ_3 are greater than ~ 2, mimicking a phase transition through a mixed-phase state. A slice of the four-dimensional parameter space with constant Γ_1 and Γ_3 is displayed in Fig. 9. The shaded region corresponds to EOS that have two stable sequences. Contours giving constant maximum mass for $1.7M_\odot$ and $2.0M_\odot$ are also shown. In the shaded region there are two contours in the parameter space for each value of maximum mass, one attaining the given value at the first maximum and the other at the second maximum of a given EOS.

We pick out six EOS on the contours of constant maximum mass and plot the corresponding mass-radius curves in the right panel of Fig. 9. EOS A, D, and F lie on the boundary between EOS with one maximum mass and EOS with two maximum masses. On the lower boundary (containing EOS A and D), the lower density maximum mass first appears. On the upper boundary (containing EOS F), the higher density sequence becomes stable. EOS E, at the intersection of the upper density and lower density maximum mass contours, has two local maximum masses with the same mass.

Figure 9 : A region in parameter space where two stable neutron-star sequences can occur is shaded in the left figure. Contours of constant maximum mass are also shown for each of the two local maxima. The higher central density maximum mass contour is solid while the lower central density maximum mass contour is dashed. Mass-radius curves are plotted for several EOS in the right panel, with stable maxima shown using solid dots. A, D, and F have a single maximum mass, while B and E have two stable regions.

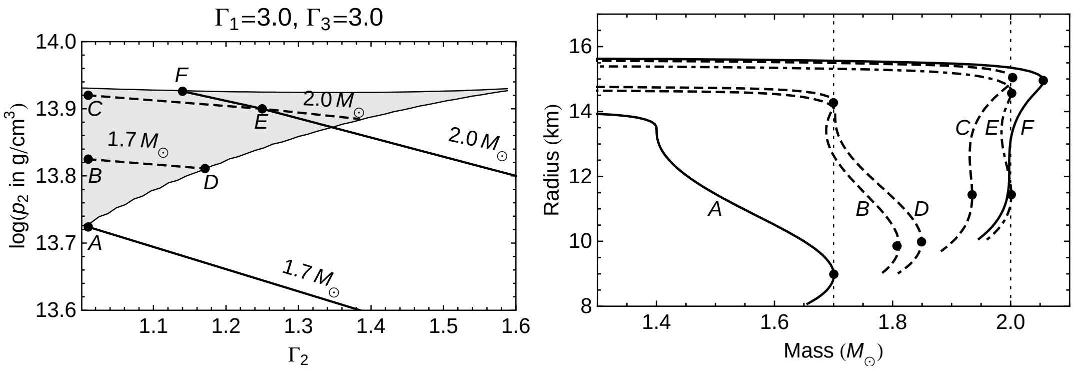

3.4.1 Causality

For an equation of state to be physically reasonable, the adiabatic speed of sound cannot exceed the speed of light. An EOS is ruled out by causality if $v_s > 1$ for densities below the central density $\rho_{\rm max}$ of the maximum-mass neutron star for that equation of state. An equation of state that becomes acausal only at densities $\rho > \rho_{\rm max}$ can always be altered to a causal EOS; because the original and altered EOS yield identical sequences of neutron stars, causality should not be used to rule out parameters that give formally acausal EOS above $\rho_{\rm max}$.

We note from the table of best-fit accuracy in Appendix B that none of the fits to the candidate EOS mispredict whether the candidate EOS is causal or acausal by more than 11% of the candidate's $v_{s,\rm max}$. We also note that for the tabled EOS with a difference in $v_{s,\rm max}$ between the fit and candidate EOS of more than 11% (at worst 18.6% for ALFC), the maximum speed of sound is significantly smaller than the speed of light. We therefore consider $v_{s,max} < 1 + 2\sigma = 1.12$ a sufficient constraint.

The causality constraint is shown in Fig. 10 projected into Γ_2-Γ_3-p_2 space. We use both a surface of $v_{s,\rm max} = 1$ as well as a surface of $v_{s,\rm max} = 1+2\sigma = 1.12$ corresponding to 2 standard deviations in the error between $v_{s,\rm max}$ of a tabled EOS candidates its best fit parameterization. The surface has two distinct regions, corresponding to p_2

below and above $\sim 10^{14}$ g/cm^3.

For $p_2 < 10^{14}$ g/cm^3 the surface is almost completely independent of the value of Γ_1. The small pressure at ρ_2 limits the speed of sound in the region $\rho_1 < \rho < \rho_2$ to causal values, no matter how the adiabatic index Γ_1 in that region is varied. In this low p_2 region, Γ_3 is restricted to be less than roughly 3.

In addition, for large Γ_2 and small Γ_3, there is a section of parameter space ruled out because this combination of parameters causes a large discontinuity in the speed of sound at the transition ρ_3 between Γ_2 and Γ_3. In this density region the speed of sound jumps above the speed of light and then drops down.

Jumps in the speed of sound are partly an artifact of using a piecewise polytrope parameterization, as the EOS has a discontinuous first derivative at the dividing densities. However, even with more realistic smoothing, such a large change in the adiabatic index will produce a spike in the speed of sound. We argue that using a surface of $v_{s,\max} = 1 + 2\sigma$ instead of $v_{s,\max} = 1$ is sufficient to account for the unrealistic jumps in the sound speed.

Finally for this lower p_2 region, we note that for small Γ_2 and moderate values of p_2 (the extreme right of Fig. 10) two stable sequences are allowed. We require $v_{s,max}$ to satisfy the constraint for both stable regions, to ensure that all stable neutron stars allowed by the EOS will be causal. This rules out EOS that are causal for maxima at a low value of ρ_c, but become acausal before the central density of a second stable maximum.

For $p_2 > 10^{14}$ g/cm^3, the central density of the maximum mass star is below ρ_3, so Γ_3 becomes irrelevant. However with larger pressure at ρ_2 the larger values of Γ_1 are able to produce acausal sound velocities. We show constraint surfaces for two values of Γ_1. For the smaller fixed $\Gamma_1 = 2.1$, a larger p_2 leads to even smaller ρ_c for the maximum mass, and all values of Γ_2 are allowed. If Γ_1 is larger, there exists a maximum p_2 above which all EOS become acausal before the central density of the maximum mass.

3.4.2 Maximum mass

The most stringent observational constraint on the EOS parameter space is set by the largest observed neutron-star mass. Unfortunately, the highest claimed masses

Figure 10 : Causality constraints are shown for two values of Γ_1. The shaded surface separates the EOS parameter space into a region behind the surface allowed by causality (labelled $v_s < c$) and a region in which corresponding equations of state violate causality (labelled $v_s > c$). A second, outlined surface shows a weaker constraint to accommodate the expected error in matching a parametrized EOS to a candidate EOS. With σ the standard deviation in v_s between an EOS and its parameterized representation, the outlined surface depicts $v_s = 1 + 2\sigma = 1.116$ constraint.

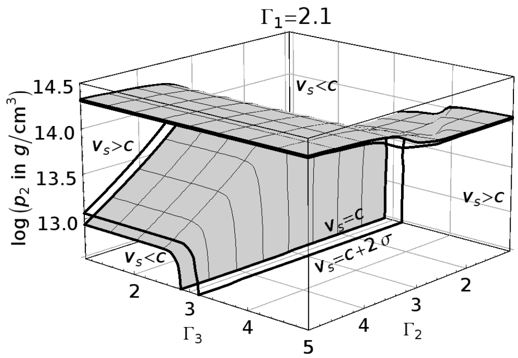

are also subject to the highest uncertainties and systematic errors. The most reliable measurements come from observations of radio pulsars in binaries. For double neutron-star systems these cluster around 1.4 $M_\odot$, with typical uncertainties a few times 0.01 $M_\odot$ and small systematic errors [50]. Recent observations of millisecond pulsars in globular clusters with non-neutron star companions have yielded higher masses: With 95% confidence either Ter 5I or Ter 5J was found to be above 1.68 $M_\odot$ [51], and more recently 95% confidence limits were obtained for M5B and NGC 6440B of 1.72 $M_\odot$ and 2.36 $M_\odot$ respectively [52, 53]. However these systems are more prone to systematic errors: The pulsar mass is obtained from assuming that the periastron advance of the orbit is due to general relativity. Periastron advance can also arise from rotational deformation of the companion, which is negligible for a neutron star but could be much greater for the latter pulsars which have white dwarf or main sequence star companions. Of the massive globular cluster pulsars, M5B is probably the most reliable due to the optical faintness of the companion. We will constrain the EOS using the interpretation that 1.7 $M_\odot$ neutron stars almost certainly exist, so that is a minimal constraint on the maximum mass. We also consider 2.0 $M_\odot$ and 2.3 $M_\odot$ as possible constraints to be confirmed by future observations.

Since all of the candidate high-mass pulsars are spinning significantly more slowly than the fastest known pulsar (at 716 Hz), considering the maximum mass for non-rotating neutron stars is sufficient. Corresponding to each point in the parameter space is a sequence of neutron stars based on the associated parametrized EOS; and a point of parameter space is ruled out if the corresponding sequence has maximum mass below the largest observed mass. We exhibit here the division of parameter space into regions allowed and forbidden by given values of an largest observed mass.

We plot contours of constant maximum mass in Fig. 11. Because equations of state below a maximum mass contour produce stars with lower maximum masses, the parameter space below these surfaces is ruled out. The error in the maximum mass between the candidate and best fit equations of state is, to one standard deviation, 1.0%, so the parameters that best fit the true equation of state are unlikely to be below this surface.

The surfaces of Fig. 11 have minimal dependence on Γ_1, indicating that the maximum mass is determined mostly by features of the equation of state above ρ_2. In Fig. 11 we have set Γ_1 to the least constraining value, i.e., that which gives the largest maximum mass, at each point in $\{p_2, \Gamma_2, \Gamma_3\}$ space. Varying Γ_1 causes the contours to shift up, constraining the parameter space further, by a maximum of $10^{0.2}$ g/cm^3. The dependence of the contour on Γ_1 is largest for $\Gamma_2 < 2$ and decreases significantly for larger Γ_2.

We note that the dependence of the maximum mass on Γ_3 decreases as the maximum mass increases. This happens because the central density of the maximum mass star decreases with increasing p_2, so the fraction of matter above the transition density ρ_3 decreases. In Fig. 11, contours of constant maximum mass vary less with Γ_3 for higher maximum masses. Note also that, for $\Gamma_2 \lesssim 2$ and $\Gamma_3 \lesssim 3$ or 4, the maximum mass is almost purely a function of p_2.

As discussed above, some of the equations of state produce two stable neutron-star sequences resulting in two local maximum masses. As shown in Fig. 9, this causes a contour in parameter space of constant maximum mass to split into two surfaces, one surface of parameters which has this maximum mass at the lower ρ_c local maximum and another surface of parameters which has this maximum mass at higher ρ_c branches. Since such equations of state allow stable models up to the largest of their local maxima, we use the least constraining surface (representing the globally maximum mass) when ruling out points in parameter space. This is usually, but not

Figure 11 : The above surfaces represent the subset of $\{p_2, \Gamma_2, \Gamma_3\}$ that produce the given maximum mass. Γ_1 is set to the least constraining value, which gives the largest possible maximum mass at each point in the space. The lower solid surface represents $M_{\max} = 1.7\ M_\odot$, the middle outlined surface represents $M_{\max} = 2.0\ M_\odot$, and the upper outlined surface represents $M_{\max} = 2.3\ M_\odot$. The observation of, for example, a 2.3 $M_\odot$ mass neutron star constrains the EOS to lie above the surface in parameter space for which $M_{\max} = 2.0 M_\odot$

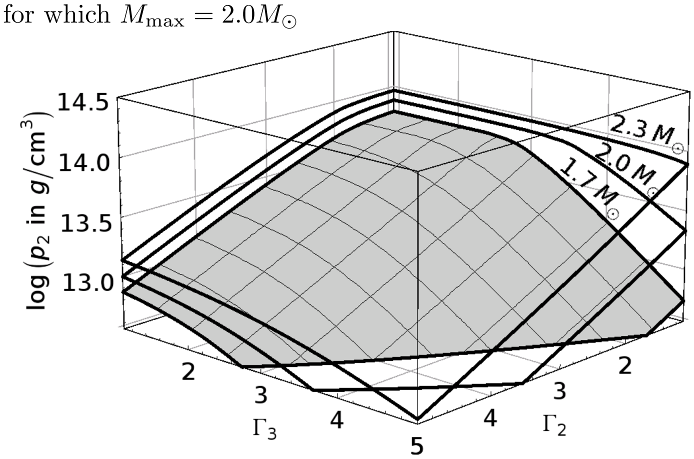

always, the surface containing EOS which reach the constant maximum mass at the higher central density (see EOS along the segment CE in Fig. 9 for examples where the lower density maximum mass is larger than the higher density maximum mass).

3.4.3 Gravitational redshift

Another observation that can constrain the parameter space is the gravitational redshift of spectral lines from the surface of a neutron star.

Cottam, Paerels, and Mendez [54] claim to have observed spectral lines from EXO 0748-676 with a gravitational redshift of $z = 0.35$. This is a difficult measurement, involving stacking (incoherently adding power) of spectra across several x-ray bursts, and thus subject to systematic errors. With three spectral lines agreeing on the redshift this measurement is more reliable than other claims involving only one line. However, doubt is cast by the fact that the claimed lines have not been seen in subsequent bursts [55].

There is a claim of a simultaneous mass-radius measurement of this system using Eddington-limited photospheric expansion x-ray bursts [56] which would rule out many equations of state. This claim is controversial because the 95% confidence interval is too wide to rule out much and the potential for systematic errors is understated. However, the gravitational redshift is consistent with the earlier claim of 0.35. Thus we treat $z = 0.35$ as a tentative constraint, and also consider $z = 0.45$ to get a feel for how high a redshift is required to greatly constrain equations of state (in the absence of separate mass and radius measurements).

Our parameterization can reproduce the maximum redshift of tabulated equations of state to 2.0% (1σ). Fig. 12 displays surfaces of constant redshift $z = 0.35$ and $z = 0.45$ for the least constraining value of $\Gamma_1 = 5$, which yields the largest redshift for fixed values of the other parameters. Surfaces with different values of Γ_1 are virtually identical for $p_2 < 10^{13.5}$ g/cm^3, but diverge for higher pressures. Equations of state with parameters in front of the $z = 0.35$ surface are allowed by the potential $z = 0.35$ measurement. The $z = 0.45$ surface shows that, without an upper limit on Γ_1, significantly higher redshifts are needed to constrain the parameter space. The majority of the parameter space ruled out by $z = 0.35$ is already ruled out by the $M_{\max} = 1.7\ M_\odot$ constraint displayed in Fig. 11.

Figure 12 : The above surfaces represent the set of parameters that result in a maximum redshift of $z = 0.35$ for the solid surface and $z = 0.45$ for the outlined surface. Γ_1 is fixed at the least constraining value of 5.0.

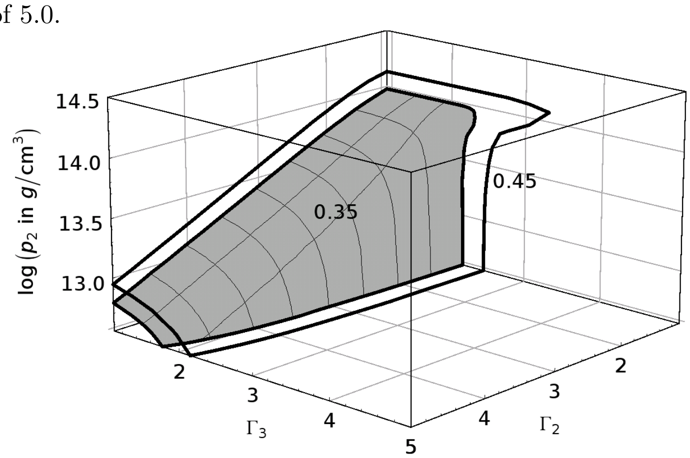

3.4.4 Maximum Spin

Observations of rapidly rotating neutron stars can also constrain the equation of state. The highest uncontroversial spin frequency is observed in pulsar Ter 5ad at

716 Hz [57]. There is a claim of 1122 Hz inferred from oscillations in x-ray bursts from XTE J1239−285 [58], but this is controversial: the statistical significance is relatively low, the signal could be contaminated by the details of the burst mechanism such as fallback of burning material, and the observation has not been repeated. Thus we use 716 Hz as a hard constraint, and ask what would happen if 1122 Hz were verified.

Currently, maximum rotation is estimated from the maximum spherical mass spherical model parameters according to the empirical formula of Haensel and Zdunik [20], with the updated coefficient discussed in Sec. 2.3.1. Preliminary work using `rns` over the full parameter space, using the methods of the same section, yields very similar constraint surfaces.

As with the maximum mass, the maximum frequency is most dependent on the parameter p_2. However, the frequency constraint complements the maximum mass constraint by placing an upper limit on p_2 over the parameter space, rather than a lower limit.

We plot surfaces of parameters giving maximum rotation frequencies of 1500 Hz and 1300 Hz in Fig. 13. The region of parameter space above the maximum observed spin surface is excluded; the least constraining value of $\Gamma_1 = 5$ is fixed. The surface corresponding a rotation of 716 Hz does not constrain the parameter values shown. The minimum observed rotation rate necessary to place a firm upper limit on p_2 is roughly 1300 Hz. A surface of $f_{\max} = 1500$ Hz for $\Gamma_3 = 5$ is also displayed in Fig. 13 to demonstrate that much higher rotation frequencies must to be observed in order to place strong limits on the parameter space.

3.4.5 Moment of inertia of a 1.338 $M_\odot$ neutron star

The moment of inertia of the double pulsar system PSR J0737−3039A may be determined to an accuracy of 10% within the next few years [59]. The mass of this star is also known to be precisely $M = 1.338\ M_\odot$. This is significant because unlike observations of a star's mass, redshift, or frequency alone, we will not need to compare the measured value against the full range of stable models predicted by a given EOS. Instead, a single value of $I_{1.338}$ is predicted by each EOS. The set of allowed parameters will be constrained to lie on the surface of constant $I_{1.338}$ itself (within the measured error) rather than to one side of the surface. Our parameterized EOS reproduces the moment of inertia of the 31 candidate equations of state to within

Figure 13 : The above surfaces represent the set of parameters that result in a maximum spin frequency of 1300 Hz for the outlined surface and 1500 Hz for the solid surface. For these surfaces $\Gamma_1 = 5$, the least constraining choice.

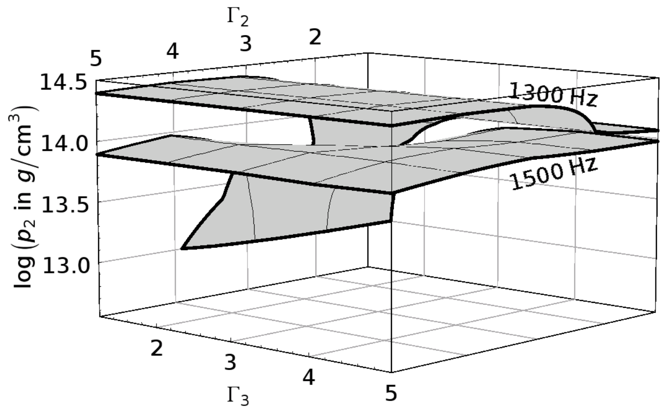

1.3% (1σ), so parametrization error will not contribute significantly to the thickness of the surface. Effectively the dimension of the possible parameter space is reduced from from 4 to 3.

As examples we plot surfaces of constant moment of inertia in Fig. 14 which span the range of moments of inertia predicted by the tabulated equations of state considered in this paper. For almost all equations of state in our parameter space, the central density of a 1.338 $M_\odot$ star is below the transition density ρ_3. Thus the surfaces of constant moment of inertia have negligible dependence on Γ_3, the adiabatic index above ρ_3. The lower solid surface of Fig. 14 represents $I_{1.338} = 1.0 \times 10^{45}\ \mathrm{g\,cm^2}$. This surface has very little dependence on Γ_1 because it represents more compact stars, with most of the mass at higher densities $\rho > \rho_2$. Such compact stars do depend slightly on Γ_3, shown by the slightly higher surface in Fig.14. The middle outlined surface represents $I_{1.338} = 1.5 \times 10^{45}\ \mathrm{g\,cm^2}$, and is almost a surface of constant p_2. The top outlined surface represents $I_{1.338} = 2.0 \times 10^{45}\ \mathrm{g\,cm^2}$. This surface has very little dependence on Γ_2, because it contains larger stars with most of the mass in a lower density state with $\rho < \rho_2$.

3.4.6 Simultaneous determination of radius and mass

If the mass of a neutron star is already known, a measurement of the radius will constrain the equation of state to a surface of constant radius in the 4-dimensional

Figure 14 : The above surfaces represent sets of parameters that result in a star with a mass of 1.338 $M_\odot$ and a fixed moment of inertia. $I_{1.338} = 1.0 \times 10^{45}$ g cm^2 for the lower solid surface and slightly higher outlined surface showing the extent of the Γ_3 dependence. $I_{1.338} = 1.5 \times 10^{45}$ g cm^2 for the middle outlined surface. $I_{1.338} = 2.0 \times 10^{45}$ g cm^2 for the top outlined surface. The wedge at the back right is the region where the parameterized core EOS does not connect with the fixed crust EOS, as shaded in Fig. 8.

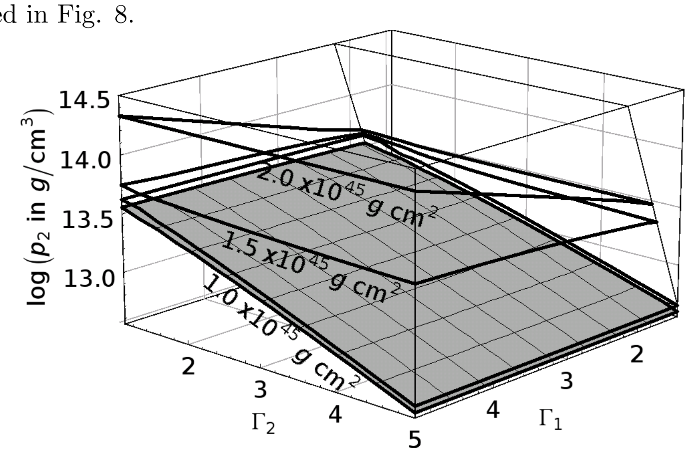

parameter space. The thickness of the surface will be dominated by the uncertainty in the radius and mass measurements, as our parameterization produces the same radius as the candidate equations of state to within 1.6% (1σ). We plot surfaces of constant radius for a 1.4 $M_\odot$ star which span the entire of radii predicted by the candidate equations of state in Fig. 15. As with moment of inertia, the radius depends negligibly on Γ_3 for all but the most compact stars of radius < 10 km. For the smallest radius example, the variation over Γ_3 is shown by the slightly higher outlined surface with $\Gamma_3 = 5$ above shaded surface with $\Gamma_3 = 1.2$.

The constraints from the radius of a $M = 1.4\ M_\odot$ star have similar behaviour to the constraints from the moment of inertia of a $M = 1.338\ M_\odot$ star.

3.4.7 Combining constraints

We can combine several of the above constraints to obtain tighter restrictions of the parameter space. In this section we focus on the constraints from maximum mass, causality, and moment of inertia of J0737−3039A, which will be most useful in constraining the parameter space.

To find the allowed region in our parameter space we tabulate all sets of parameters that produce neutron stars that satisfy causality, have a mass less than some choice of

Figure 15 : The above surfaces represent the set of parameters that result in a star with a mass of 1.4 $M_\odot$ and a fixed radius. $R = 9$ km for the lower solid surface and a slightly higher outlined surface showing the limits $\Gamma_3 = 1.2$ and $\Gamma_3 = 5$ respectively. $R = 12$ km for the middle outlined surface. $R = 16$ km for the top outlined surface. The wedge on the back right is the region region where the parameterized core EOS does not connect with the known crust EOS, as shaded in Fig. 8

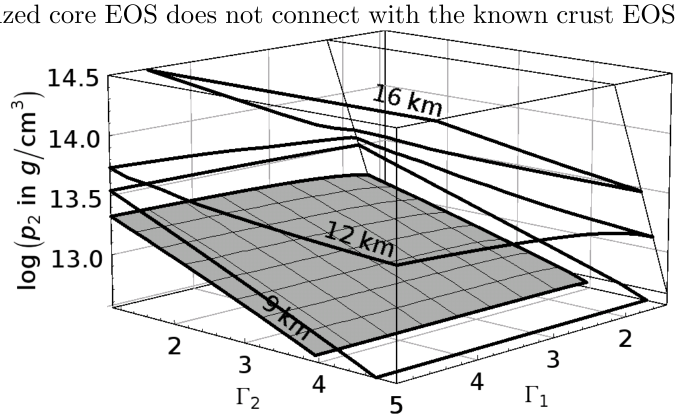

maximum mass (we consider $M_{\max} = 1.7 M_\odot$, as well as possible future constraints of $M_{\max} = 2.0 M_\odot$ and $2.3 M_\odot$) and have a given moment of inertia for a 1.338 $M_\odot$ star. This gives us a volume in Γ_2-Γ_3-p_2 space (see Fig. 16). The thickness of the volume corresponds to the dependence of the moment of inertia on Γ_1: For small moments of inertia there is negligible dependence on Γ_1 so the allowed volume in Fig. 16 is thin. As the moment of inertia increases, the thickness of the allowed volume in the parameter space increases due to possible variation of Γ_1.

In Fig. 17 we show projections of this volume into the Γ_2-Γ_3 plane for three values of the moment of inertia which span the range predicted by the candidate equations of state. We also show the constraints from three different mass observations to show the allowed region in parameter space if higher mass stars are confirmed.

If $I_{1.338} = 1.0 \times 10^{45}$ g cm^2 for J0373-3039A and the maximum mass is known to be at least 1.7 $M_\odot$, Γ_3 is restricted to lie within a small range, while Γ_2 is unconstrained. For larger observed masses, the constraint is even more stringent; stars with a mass greater than roughly 1.9 $M_\odot$ are incompatible with a moment of inertia of $I_{1.338} = 1.0 \times 10^{45}$ g cm^2 for J0737$-$3039A, unless the parameter space is widened to include implausibly large values of Γ_2.

For a moderate moment of inertia, $I_{1.338} = 1.5 \times 10^{45}$ g cm^2, both Γ_3 and Γ_2 are constrained. If higher mass stars are confirmed, then the allowed region in parameter

Figure 16 : The allowed volume in Γ_2-Γ_3-p_2 space for two different values of the moment of inertia of J0737−3039A combined with the maximum mass constraint from a 1.7 $M_\odot$ star and causality ($v_{s,max} = 1 + 2\sigma$). The thickness of the allowed region comes from the possible range of Γ_1.

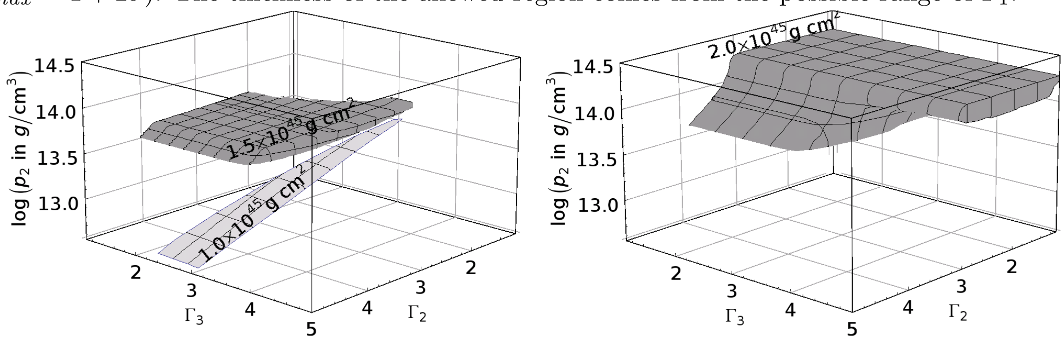

space is restricted further for this value of I. In particular, a 2.3 $M_\odot$ star would roughly require that $3 < \Gamma_2 < 4$ and $\Gamma_3 < 3$.

A large moment of inertia, $I_{1.338} = 2.0 \times 10^{45}$ g cm^2, requires EOS with large maximum masses, so the parameters are additionally restricted only by the causality constraint. The maximum mass constraint cannot rule out small values of Γ_2 and Γ_3 unless masses greater than 2.3 $M_\odot$ are observed.

The allowed range for p_2 as a function of the moment of inertia of J0737−3039A is shown in Fig. 18. It should be noted that for small moments of inertia, as shown in Fig. 16, the allowed volume in Γ_2-Γ_3-p_2 space is nearly two dimensional. If the moment of inertia is measured to be this small, then the EOS would be better parameterized with a linear combination $\alpha \log_{10}(p_2) + \beta\Gamma_2$ instead of two separate parameters Γ_2 and $\log_{10}(p_2)$.

Figure 17 : The allowed values of Γ_2 and Γ_3 for given values of moment of inertia for the double pulsar member J0737−3039A. $I = 1.0 \times 10^{45}$ g cm^2 in the top left figure. $I = 1.5 \times 10^{45}$ g cm^2 in the top right figure. $I = 2.0 \times 10^{45}$ g cm^2 in the bottom figure. In each figure the upper curves are the $v_s = 1$ and $v_s = 1 + 2\sigma = 1.11$ causality constraints. The largest value of I requires parameters compatible with maximum mass over $2.3 M_\odot$; the smallest value is only compatible with maximum masses below roughly $1.9 M_\odot$.

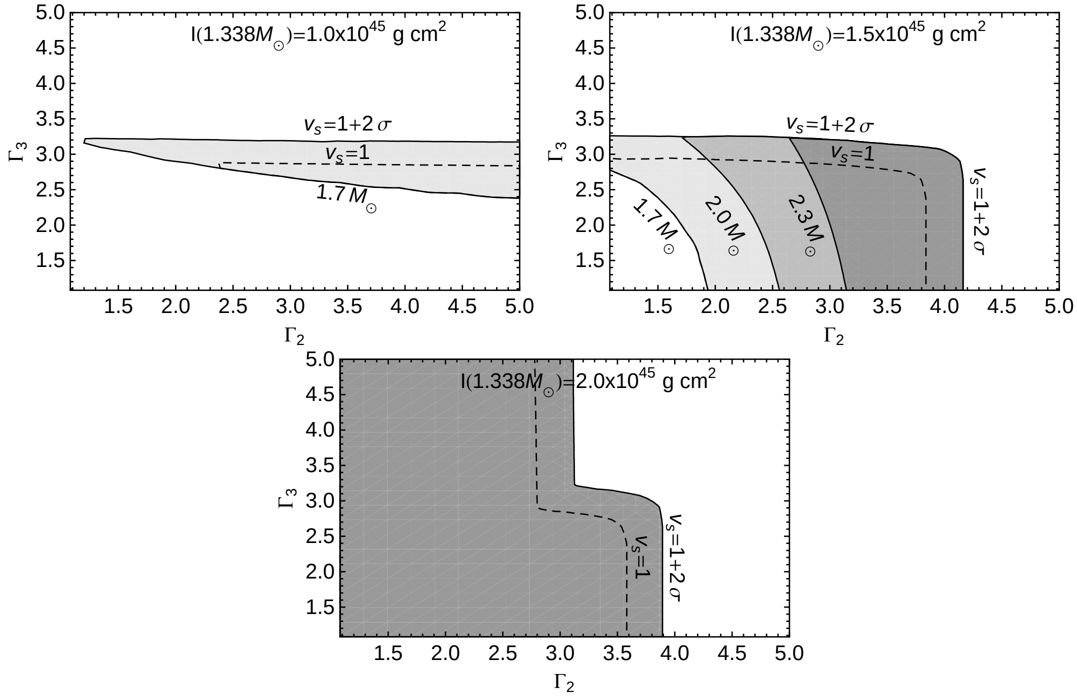

Figure 18 : The allowed range of p_2 as a function of the moment of inertia of J0737−3039A when combined with causality ($v_{s,max} = 1 + 2\sigma$) and observed mass constraints. The entire shaded range is allowed by a 1.7 $M_\odot$ star observation. The medium and dark shades are allowed if a 2.0 $M_\odot$ star is confirmed. Only the darkest shade is allowed if a 2.3 $M_\odot$ star is confirmed.

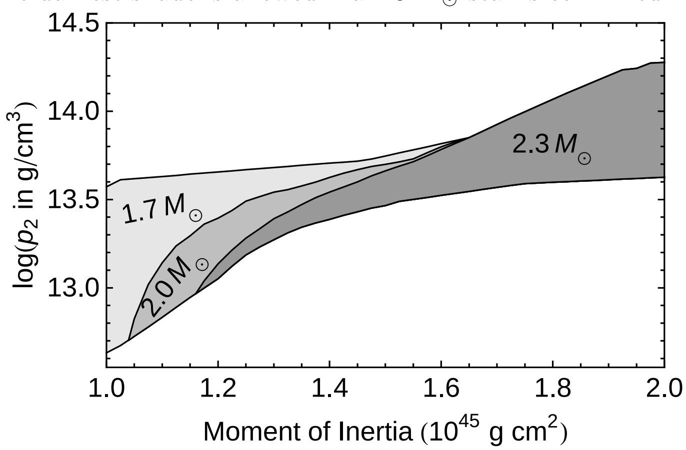

Part II

Quasiequilibrium and helical symmetry

Chapter 4

Quasiequilibrium approximations

4.1 Quasiequilibrium sequences and initial data

For numerical simulations, it is most common to consider a Cauchy problem in general relativity, where initial data on a spacelike slice is numerically evolved along a timelike coordinate. In the initial value problem of general relativity, as in electromagnetism, there are constraints that the initial fields must satisfy to be consistent with the Einstein equations on the full spacetime. Furthermore, to gain physical insight from the simulations, one wishes to specify an astrophysically realistic configuration of matter and fields on the slice.

Methods of specifying astrophysically realistic initial data generally rely on a quasiequilibrium approximation to the radiating problem: when the radiation timescale is small compared to orbital timescales and, as in the post-Newtonian equations of motion for binary systems, the motion is assumed to be instantaneously circular.

When used as initial data for numerical simulations, the circular orbit approximation leads to an unphysical eccentricity in the evolving orbits as it neglects the infall of the two masses. Various groups currently use an empirically tuned radial velocity, modifying the circular-orbit initial data, to minimize this issue.

An expanded recent treatment of quasiequilibrium initial data is in Gourgoulhon's review [60], with notation chosen to align with the upcoming treatment of helically symmetric initial data beyond conformal flatness in Sec. 4.4, which will follow that of [61, 62, 63]. We refer also to notes of Friedman and Uryu [64, 65].

4.2 3+1 decomposition

We consider a globally hyperbolic spacetime $\{M, g_{\alpha\beta}\}$, foliated by a family $(\Sigma_t)_{t\in\mathbb{R}}$ of spacelike Cauchy hypersurfaces parametrized by the coordinate t. At each point, the generator of time translations $t^\alpha = \partial_t$ can be written in terms of the future pointing normal n^α to the slice Σ_t as

$$t^\alpha = \alpha n^\alpha + \beta^\alpha. \tag{4.1}$$

with lapse α and shift β^α, $\beta^\alpha n_\alpha = 0$.

The spatial metric γ_{ab} on each slice Σ_t is the restriction to Σ_t of the projection tensor $\gamma_{\alpha\beta}$ orthogonal to n_α,

$$\gamma_{\alpha\beta} = g_{\alpha\beta} + n_\alpha n_\beta, \tag{4.2}$$

and has an associated covariant derivative D_α. The extrinsic curvature of each Σ_t is

$$K_{ab} = -\frac{1}{2}\pounds_n \gamma_{ab}, \tag{4.3}$$

where the Lie derivative $\pounds_n$ with respect to n^α operating on *spatial* tensors such as γ_{ab} has the meaning

$$\pounds_n \gamma_{ab} = \frac{1}{\alpha}\partial_t \gamma_{ab} - \frac{1}{\alpha}\pounds_\beta \gamma_{ab}, \tag{4.4}$$

with $\partial_t \gamma_{ab}$ the pullback of $\pounds_t \gamma_{\alpha\beta}$ to Σ. K will refer to the trace $K = \gamma^{ij} K_{ij}$.

We can specify the full metric $g_{\alpha\beta}$ in terms of the fixed coordinate t, the spatial metric $\gamma_{ij}(t)$, and the lapse $\alpha(t)$ and shift $\beta^i(t)$. In the chart $\{t, x^i\}$ where Σ_t is a surface of constant t, the metric is

$$ds^2 = -\alpha^2 dt^2 + \gamma_{ij}(dx^i + \beta^i dt)(dx^j + \beta^j dt). \tag{4.5}$$

The Einstein equations $G_{\alpha\beta} = 8\pi T_{\alpha\beta}$ are decomposed with respect to the foliation by projecting onto or perpendicular to the slices Σ_t. The projection perpendicular to the slices with $n^\alpha n^\beta$ is the Hamiltonian constraint. The projections with $n^\alpha \gamma^\beta_\gamma$ are the three momentum constraints. The projections onto to the slices with $\gamma^\alpha_\gamma \gamma^\beta_\delta$ are the six evolution equations.

Initial data on a slice is generally specified by the spatial metric γ_{ij} and the extrinsic curvature K_{ij}. Note that the extrinsic curvature can be determined, for a given foliation, by γ_{ij}, $\partial_t \gamma ij$, the lapse α, and the shift β^i using Eq. (4.3).

Arbitrary initial data that satisfies the four constraint equations can be consistently evolved using the six evolution equations. The challenge becomes choosing which components to fix by solving constraint equations and which to otherwise specify to give astrophysically realistic data.

4.3 Conformally flat initial data

A common approximation used for initial data is that the initial slice has a spatial metric γ_{ab} conformal with a flat metric. Initial data calculated in this way is referred to as conformally flat initial data. Conformally flat initial data agrees with first order post-Newtonian calculations, but one recovers full GR results only in static and spherically symmetric cases. In a spatially conformally flat spacetime, there is no radiation.

In the conformal decomposition, we introduce a conformal metric $\tilde{\gamma}_{ab}$ and conformal factor Ψ satisfying

$$\gamma_{ab} = \Psi^4 \tilde{\gamma}_{ab} \tag{4.6}$$

with the condition that $\det\tilde{\gamma}_{ab} = \det f_{ab}$, with f_{ab} a flat background metric on the spatial slice Σ_t. $\tilde{\gamma}_{ab}$ contains five degrees of freedom. The flat background reference metric allows use of arbitrary coordinate types including Cartesian and spherical.

The method of finding conformally flat initial data with the Isenberg-Wilson-Matthews formulation (using $K = 0$) will be described in a way that will be generalized to waveless and helically symmetric formulations in Sec. 4.4.

The approximation of conformal flatness restricts to the case $\tilde{\gamma}_{ab} = f_{ab}$.

$$ds^2 = -\alpha^2 dt^2 + \psi^4 f_{ij}(dx^i + \beta^i dt)(dx^j + \beta^j dt), \tag{4.7}$$

We must solve for five metric functions $\{\alpha, \beta^i, \psi\}$, which can be done using the Hamiltonian constraint and the three momentum constraints, with the remaining degree of freedom specified to satisfy trace of the projection of $G_{\alpha\beta} = 8\pi T_{\alpha\beta}$ onto Σ_t with $\gamma^{\alpha\beta}$

Let $\overset{\circ}{\Delta}$ be the Laplacian of the flat metric f_{ab}, defined by $\overset{\circ}{\Delta} = \overset{\circ}{D}{}^c \overset{\circ}{D}_c$, where $\overset{\circ}{D}$ is the conformal derivative compatible with f_{ab}. The vacuum part of the equations used can be written

$$G_{\alpha\beta}n^\alpha n^\beta \;=0\;:\;\; \overset{\circ}{\Delta}\psi + \frac{\psi^5}{8}\left(A_{ab}A^{ab} + \frac{2}{3}K^2\right) = 0, \tag{4.8}$$

$$G_{\alpha\beta}\gamma_a{}^\alpha n^\beta \;=0\;:\;\; \overset{\circ}{\Delta}\tilde{\beta}_a + \frac{1}{3}\overset{\circ}{D}_a\overset{\circ}{D}_b\tilde{\beta}^b + 2\alpha A_a{}^b\overset{\circ}{D}_b \ln\frac{\psi^6}{\alpha} - \frac{4}{3}\alpha\overset{\circ}{D}_a K = 0, \tag{4.9}$$

$$G_{\alpha\beta}\gamma^{\alpha\beta} = 0 \;\;:\;\; \overset{\circ}{\Delta}(\alpha\psi) + \psi^5 \pounds_{t-\beta}K - \alpha\psi^5\left(\frac{7}{8}A_{ab}A^{ab} + \frac{5}{12}K^2\right) = 0. \tag{4.10}$$

in terms of the trace free part of the extrinsic curvature $K_{\alpha\beta}$:

$$A_{ab} := K_{ab} - \frac{1}{3}\gamma_{ab}K \tag{4.11}$$

We also specify $K = 0 = \partial_t K$, the maximal slicing gauge condition.

When the spatial metric is conformally flat, the above equations do not contain time derivatives of the spatial metric. Then Eqs. (4.8–4.10) are a system of elliptic equations that can be solved iteratively, using Green's functions for $\overset{\circ}{\Delta}$ to impose boundary conditions accurate far from the sources. These equations are the basis for the numerical initial data codes described in [66, 67].

All terms except for the flat Laplacian $\overset{\circ}{\Delta}$ are collected in the source, writing the equations in the general form $\overset{\circ}{\Delta}\psi = S_\psi$, $\overset{\circ}{\Delta}\alpha = S_\alpha$, ... Then the integral form of each PDE is written, using a Green's function $G(x,x')$ of the flat Laplacian,

$$\begin{aligned}\psi(x) = &-\frac{1}{4\pi}\int_V G(x,x')S(x')d^3x' \\ &+\frac{1}{4\pi}\int_{\partial V}\left[G(x,x')\nabla\psi(x') - \psi(x')\nabla' G(x,x')\right]d^3x'.\end{aligned} \tag{4.12}$$

To solve the nonlinear problem, one iterates from an initial approximate solution, updating the effective sources $S_{\psi,n}$, $S_{\alpha,n}$, ... at each step with the solutions ψ_{n-1}, α_{n-1}, ..., of the previous iteration.

The source is assumed to be stationary in the rotating frame. While this condition is simplest for perfect fluid sources co-rotating with the orbital motion, it allows nonzero velocity of fluid elements if the overall fluid profile remains stationary in the rotating frame. Irrotational neutron stars can thus be constructed by specifying a irrotational velocity potential.

4.4 Helical symmetry: beyond conformal flatness

A way to go beyond spatial conformal flatness is to construct an analog in full GR of Newtonian binaries that are stationary in a rotating frame. In general relativity, these models are helically symmetric spacetimes [68, 69], with stationarity enforced using equal amounts of ingoing and outgoing radiation. Binary black holes of this kind were first discussed by Blackburn and Detweiler [70], and models involving non-linear scalar wave equations have been studied by a group of researchers organized by Price [71, 72, 73, 74, 75, 76]. Because the power radiated by a helically symmetric binary is constant in time, the spacetime cannot be asymptotically flat. At distances large compared to $1/\Omega$, however, the spacetime of a binary system with a helical Killing vector approximates asymptotic flatness—until, at a radius of about $10^4 M$ for neutron-star models of mass M, the enclosed energy in gravitational waves becomes comparable to the mass of the binary components.

The helical symmetry approximation is similar to a 3rd post-Newtonian approximation in which the 2.5 post-Newtonian radiation is omitted. It is designed to improve the accuracy of initial data in the near zone, where the Coulomb part of the fields dominates the radiative part, by including terms that ignored when assuming spatial conformal flatness.

4.4.1 Formulation

We extend the metric to allow departures h_{ij} from the flat spatial metric f_{ij}

$$ds^2 = -\alpha^2 dt^2 + \psi^4 (f_{ij} + h_{ij})(dx^i + \beta^i dt)(dx^j + \beta^j dt). \tag{4.13}$$

maintaining the conformal conditions $\gamma_{ab} = \psi^4 \tilde{\gamma}_{ab}$ and $\det\tilde{\gamma} = \det f$, so that $\det h = 0$. We also introduce the departures h^{ab} with raised indices such that

$$\tilde{\gamma}_{ab} - f_{ab} = h_{ab}\,, \quad \tilde{\gamma}^{ab} - f^{ab} = h^{ab}. \tag{4.14}$$

Note that $h_{ab}h^{bc} \neq \delta_a^c$.

We now solve for $\{\alpha, \beta^a, \psi, h_{ab}\}$. We use the Hamiltonian and momentum constraints, which are elliptic equations as expressed in the conformally flat case in Eqs. (4.8–4.10). We then add the remaining components of the spatial projections of the Einstein equations, the trace-free parts

$$(G_{\alpha\beta} - 8\pi T_{\alpha\beta})\left(\gamma_a{}^\alpha \gamma_b{}^\beta - \frac{1}{3}\gamma_{ab}\gamma^{\alpha\beta}\right) = 0. \tag{4.15}$$

We again choose maximal slicing $K = 0$, and for the non-flat spatial metric specify the generalized Dirac gauge

$$\mathring{D}_a h^{ab} = 0. \tag{4.16}$$

While Eq. (4.10) is elliptic [61], Eq. (4.15) has the form

$$(G_{\alpha\beta} - 8\pi T_{\alpha\beta})\left(\gamma_a{}^\alpha \gamma_b{}^\beta - \frac{1}{3}\gamma_{ab}\gamma^{\alpha\beta}\right) = \mathcal{E}_{ab} - \frac{1}{3}\gamma_{ab}\gamma^{cd}\mathcal{E}_{cd} = 0, \tag{4.17}$$

with

$$\mathcal{E}_{ab} := -\pounds_n K_{ab} + {}^3R_{ab} + KK_{ab} - 2K_{ac}K_b{}^c - \frac{1}{\alpha}D_a D_b \alpha - 8\pi S_{ab}, \tag{4.18}$$

where ${}^3R_{ab}$ is the Ricci tensor on Σ associated with γ_{ab}, and S_{ab} is the projection of the energy stress tensor, $S_{ab} := T_{\alpha\beta}\gamma_a{}^\alpha\gamma_b{}^\beta$. Two derivatives of the timelike coordinate appear in $-\pounds_n K_{ab}$, coming from two applications of the Lie derivative with respect to the normal vector n^α—the first of which is seen in Eq. (4.3). Thus this equation has a principle part which is hyperbolic in character. To solve on a single initial slice, we impose a condition on the time derivative: the spacetime must be (instantaneously) helically symmetric.

4.4.2 Helical symmetry

A helical symmetry vector $k^\alpha = t^\alpha + \Omega\phi^\alpha$ is defined. It is related to the usual 3+1 slicing by

$$k^\alpha = \alpha n^\alpha + \omega^\alpha, \tag{4.19}$$

where ω^α is a shift vector which is rotating from the perspective of observers along t^α

$$\omega^\alpha = \beta^\alpha + \Omega\phi^\alpha. \tag{4.20}$$

Helical symmetry, $\pounds_k g_{\alpha\beta} = 0$, leads to conditions on the 3-metric and the extrinsic curvature,

$$\pounds_k \gamma_{ab} = 0, \quad \pounds_k K_{ab} = 0. \tag{4.21}$$

which, from Eq. (4.19), imply

$$\pounds_n \gamma_{ab} = -\frac{1}{\alpha}\pounds_\omega \gamma_{ab}, \quad \text{and} \quad \pounds_n K_{ab} = -\frac{1}{\alpha}\pounds_\omega K_{ab}. \tag{4.22}$$

The use of these relations in Eq. (4.15) translates it into a form which is mixed hyperbolic-elliptic. The principle part of the equation has the form of a Helmholtz equation. The mixed character, by itself, is not a barrier to convergent solutions using elliptical methods, as will be seen in Chapter 5.

4.4.3 Waveless approximation: elliptic equations for h_{ab}

Successful initial data codes of Uryu et al. [63] use a modified condition on the spatial metric to convert Eq. (4.15) to a fully elliptic equation. This waveless code differs from the helically symmetric code by the requirement that $\tilde{\gamma}_{ab}$ have vanishing derivative along t^α, rather than vanishing derivative along k^α. However, the source motion is still required to be helically symmetric.

These requirements result in elliptic equations for the field variables, including the non-conformal part of the 3-metric $h_{ab} = \tilde{\gamma}_{ab} - f_{ab}$. As the time derivative of the conformal metric vanishes, the extrinsic curvature is associated with the non-rotating shift β^a,

$$K_{ab} = -\frac{1}{2}\pounds_n \gamma_{ab} = \frac{1}{2\alpha}\pounds_\beta \gamma_{ab}, \tag{4.23}$$

instead of the rotating shift ω^a as in (4.22).

4.4.4 Fully helical: Helmholtz equation for h_{ab}

By isolating the terms, $\Box h_{ab} := (-\partial_t^2 + \mathring{D}^a \mathring{D}_a) h_{ab}$, that occur in $\mathcal{E}_{ab}$ in Eq. (4.18), one can rewrite Eq. (4.17) in the form

$$\Box h_{ab} = \mathcal{S}_{ab}, \tag{4.24}$$

where $\Box$ is the flat d'Alembertian operator and $\mathring{D}^a := f^{ab}\mathring{D}_b$. Then helical symmetry of the conformal metric, $\pounds_k \tilde{\gamma}_{ab} = \pounds_k h_{ab} = 0$, results in the operator

$$\Box h_{ab} = -\partial_t^2 h_{ab} + \mathring{D}^c \mathring{D}_c h_{ab} = (\mathring{\Delta} - \Omega^2 \pounds_\phi^2) h_{ab}, \tag{4.25}$$

where the flat Laplacian is again defined by $\mathring{\Delta} = \mathring{D}^c \mathring{D}_c$.

Even when one uses the Cartesian components h_{ij} of h_{ab}, however, $\mathring{\Delta}-\Omega^2\pounds_\phi^2$ does not coincide with the Helmholtz operator, because $\partial_\phi h_{ij}$ is a Cartesian component of $\boldsymbol{\phi}\cdot\mathring{\boldsymbol{D}}h_{ab}$, not of $\pounds_{\boldsymbol{\phi}}h_{ab}$. To isolate the Helmholtz operator $\mathcal{L}=\mathring{\Delta}-\Omega^2\partial_\phi^2=\mathring{\Delta}-\Omega^2(\boldsymbol{\phi}\cdot\mathring{\boldsymbol{D}})^2$, we write $\partial_\phi:=\boldsymbol{\phi}\cdot\mathring{\boldsymbol{D}}$ and find

$$\pounds_{\boldsymbol{\phi}}^2\tilde{\gamma}_{ab}=\partial_\phi^2\tilde{\gamma}_{ab}\,+\,(\partial_\phi\tilde{\gamma}_{ac}+\pounds_{\boldsymbol{\phi}}\tilde{\gamma}_{ac})\mathring{D}_b\phi^c\,+\,(\partial_\phi\tilde{\gamma}_{cb}+\pounds_{\boldsymbol{\phi}}\tilde{\gamma}_{cb})\mathring{D}_a\phi^c, \tag{4.26}$$

where a relation $\phi^c\mathring{D}_c(\mathring{D}_a\phi^b)=0$ is used. Moving all terms in Eq. (4.26) except $\partial_\phi^2\tilde{\gamma}_{ab}$ from the LHS to the RHS of Eq. (4.24), we obtain the Helmholtz form

$$\begin{aligned}\mathcal{L}h_{ab}=\bar{\mathcal{S}}_{ab}:=2\left(\bar{\mathcal{E}}_{ab}-\frac{1}{3}\tilde{\gamma}_{ab}\tilde{\gamma}^{cd}\bar{\mathcal{E}}_{cd}\right)&\\ -\frac{1}{3}\tilde{\gamma}_{ab}\mathring{D}^e h^{cd}\mathring{D}_e h_{cd}+\frac{1}{3}\tilde{\gamma}_{ab}\Omega^2\partial_\phi h^{cd}\partial_\phi h_{cd},&\end{aligned} \tag{4.27}$$

where the barred expression $\bar{\mathcal{E}}_{ab}$ is defined by

$$\begin{aligned}\bar{\mathcal{E}}_{ab}:=\ &R^{\rm NL}_{ab}+{}^3\tilde{R}^{\psi}_{ab}-\frac{1}{\alpha}D_aD_b\alpha-2\psi^4\tilde{A}_{ac}\tilde{A}_b{}^c-8\pi S_{ab}\\ &+\frac{1}{2}\left(\frac{\psi^4}{\alpha^2}-1\right)\Omega^2\partial_\phi^2h_{ab}+\frac{\psi^4}{\alpha^2}\,\Omega\left(\pounds_\phi\pounds_\beta\tilde{\gamma}_{ab}+\frac{1}{2}\pounds_{[\beta,\phi]}\tilde{\gamma}_{ab}\right)\\ &+\frac{\psi^4}{2\alpha^2}\,\Omega^2\left[(\partial_\phi\tilde{\gamma}_{ac}+\pounds_{\boldsymbol{\phi}}\tilde{\gamma}_{ac})\mathring{D}_b\phi^c\,+\,(\partial_\phi\tilde{\gamma}_{cb}+\pounds_{\boldsymbol{\phi}}\tilde{\gamma}_{cb})\mathring{D}_a\phi^c\right]\\ &+\frac{\psi^4}{2\alpha^2}\,\pounds_\beta\pounds_\beta\tilde{\gamma}_{ab}\,+\,\frac{\psi^4}{\alpha}\tilde{A}_{ab}\,\pounds_\omega\ln\frac{\psi^8}{\alpha}.\end{aligned} \tag{4.28}$$

In this expression for $\bar{\mathcal{E}}_{ab}$, the coordinate conditions $K=0$ and $\mathring{D}_b\tilde{\gamma}^{ab}=0$, mentioned above, are imposed; and the trace-free part A_{ab} of the extrinsic curvature, $A_{ab}:=K_{ab}-\frac{1}{3}\gamma_{ab}K$, is introduced in the rescaled form $\tilde{A}_{ab}:=\psi^{-4}A_{ab}$. The terms $R^{\rm NL}_{ab}$ and ${}^3\tilde{R}^{\psi}_{ab}$ arise from the conformal decomposition of the Ricci tensor, given in Ref. [61].

The source (4.28) can be written concisely without separating the second derivative term $\partial_\phi^2h_{ab}$ explicitly as above. Applying the helical symmetry condition (4.22) to Eq. (4.18) and subtracting $\partial_\phi^2h_{ab}$ term from both sides of Eq. (4.17), the source term of Eq. (4.27) can be rewritten

$$\begin{aligned}\bar{\mathcal{E}}_{ab}:=\ &\frac{1}{\alpha}\pounds_\omega(\psi^4\tilde{A}_{ab})-\frac{1}{2}\Omega^2\partial_\phi^2h_{ab},\\ &+R^{\rm NL}_{ab}+{}^3\tilde{R}^{\psi}_{ab}-\frac{1}{\alpha}D_aD_b\alpha-2\psi^4\tilde{A}_{ac}\tilde{A}_b{}^c-8\pi S_{ab}\end{aligned} \tag{4.29}$$

which is equivalent to the above source term (4.28).

The nonlinear Helmholtz equation (4.27) can be solved with an iterative Green's function method for the Helmholtz operator $\mathcal{L}$ similar to that described for the Laplacian $\mathring{\Delta}$ in Sec. 4.3. Decomposing the fields into spherical harmonics gives an elliptic equation for each harmonic, as will be seen explicitly for a toy scalar field model in Chapter 5.

4.4.5 Helical/Waveless: elliptic equation for h_{ab}

Instead of isolating the Helmholtz operator for iteration, one can formally isolate the elliptic $\mathring{\Delta}$ operator and solve the equation iteratively using the elliptic solver of the waveless approximation code. With this grouping of terms, the helical symmetry condition (4.22) is applied to Eq. (4.18). This the term $\pounds_\omega K_{ab}$ as part of the effective source, and the Laplacian of h_{ab} is separated out from ${}^3R_{ab}$. With gauge conditions $K = 0$ and $\mathring{D}_b\tilde{\gamma}^{ab} = 0$, as before, we have

$$\mathring{\Delta}h_{ab} = 2\left(\widehat{\mathcal{E}}_{ab} - \frac{1}{3}\tilde{\gamma}_{ab}\tilde{\gamma}^{cd}\widehat{\mathcal{E}}_{cd}\right) - \frac{1}{3}\tilde{\gamma}_{ab}\mathring{D}^e h^{cd}\mathring{D}_e h_{cd}, \tag{4.30}$$

where $\widehat{\mathcal{E}}_{ab}$ is given by

$$\widehat{\mathcal{E}}_{ab} := \frac{1}{\alpha}\pounds_\omega(\psi^4\tilde{A}_{ab}) + R^{\rm NL}_{ab} + {}^3\tilde{R}^{\psi}_{ab} - \frac{1}{\alpha}D_aD_b\alpha - 2\psi^4\tilde{A}_{ac}\tilde{A}_b{}^c - 8\pi S_{ab}. \tag{4.31}$$

In Eq. (4.31), the first term appears instead of the last three lines in Eq. (4.28).

We find that the helically symmetric code does not converge in this method when we solve the above set of equations on Σ with a boundary that extends several wavelengths (or more) beyond the source. We were, however, able to obtain a converged solution when exact helical symmetry is imposed only in the near zone, within about a wavelength from the source, and the waveless approximation is used for larger r, effectively setting boundary conditions at the boundary of the helically symmetric inner zone.

For the near-zone helically symmetric solution, the change from helical symmetry to the waveless formulation at about one wavelength from the source implies the condition for K_{ab}

$$K_{ab} = \begin{cases} \dfrac{1}{2\alpha}\pounds_\omega\gamma_{ab} = \dfrac{1}{2\alpha}\left(\pounds_\beta\gamma_{ab} + \Omega\pounds_{\boldsymbol{\phi}}\gamma_{ab}\right), \text{ for } & r < f\dfrac{\pi}{\Omega}, \\ \\ \dfrac{1}{2\alpha}\pounds_\beta\gamma_{ab}, & \text{for } \ r \geq f\dfrac{\pi}{\Omega}, \end{cases}$$

where π/Ω is the approximate wavelength of the $l = m = 2$ gravitational wave mode. The constant f, the coordinate radius of the helically symmetric zone in units of π/Ω, is restricted to $f \lesssim 1$ for convergence.

4.4.6 Numerical solutions

The numerical code is based on the finite difference code developed in Refs. [66, 63]. The code extends a KEH iteration scheme, introduced for quickly rotating stars in Chapter 2, to the binary neutron star computation. Cartesian components of the field equations are solved numerically on spherical coordinate grids, r, θ, and ϕ. An equally spaced grid is used from the centre of orbital motion to $5R_0$ where there are 16 or 24 grid points per R_0; from $5R_0$ to the outer boundary of computational region a logarithmically spaced grid has 60 or 90, where R_0 is the coordinate radius of a compact star along a line passing through the centre of orbit to the centre of a star. Accordingly, for θ and ϕ there are 32 or 48 grid points each from 0 to $\pi/2$. The Green's function method is applied to a spherical harmonic decomposition of the fields, with multipoles summed up to $l = 32$ [66].

The source is modelled by a perfect fluid having polytropic equation of state, $p = K\rho^\Gamma$, with ρ the baryon density. We display results for the choices $\Gamma = 2$, appropriate to neutron star matter; for compactness of a star in isolation $(M/R)_\infty = 0.14$; and for half the binary separation $d/R_0 = 1.375$.

In solving the Einstein equation with full helical symmetry, however, convergence is achieved only in the near zone, and we impose boundary conditions by matching to an exterior waveless solution outside a coordinate radius $r = f\pi/\Omega$.

For $f \lesssim 1$, the code converges, yielding a helically symmetric solution in the near zone $r \leq f\pi/\Omega$. As shown in Fig. 19, the solution is *nearly identical* to the waveless solution. The right panel shows a difference larger than 1% only when the metric component itself is smaller than 0.03; as a percentage of $h_{ij}(r = 0)$, the difference is everywhere less than 1%. The threshold of the value of f for convergence is $0.7 \lesssim f \lesssim 1$ depending on the binary separation, compactness and resolution of finite differencing.

We may expect from the result that, with boundary conditions that minimize the amplitude of gravitational waves, the exact helical solution will be close to the waveless solution near the source. This is a hopeful outcome: The waveless and helically symmetric formalisms are each intended to give a solution whose inaccuracy arises from neglecting gravitational waves, and they should give nearly identical results in the near zone where the gravitational wave amplitude is small compared to the Coulomb fields.

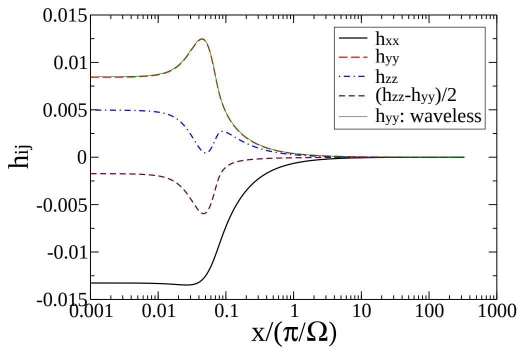

Figure 19 : Left panel: Plot of components h_{ij} along the x-axis normalized by π/Ω, the wavelength of the $l = m = 2$ mode. The solution to Eq. (4.30) with the mixed helical and waveless source of Eqs. (4.31) and (4.32), and the h_{yy} component of the waveless solution are shown. Right panel: The fractional difference of these two solutions is plotted for selected components of h_{ij} for $r < 10\pi/\Omega$. The fractional errors increase for larger r because the values of the components h_{ij} are themselves small. A compact star extends from $x/(\pi/\Omega) = 0.0125$ to 0.079, the boundary of computational region is set to $10^4 R_0 \sim 332\pi/\Omega$, and the cutoff constant f in Eq. (4.32) is set to $f = 0.7$.

The comparison of helical/waveless and waveless results suggests that, in modelling binary neutron stars, comparable accuracy will result from codes that match a helically symmetric solution to a waveless solution, from a purely waveless code, and from a helically symmetric code. From a more mathematical perspective, however, finding a solution that has exact helical symmetry on the full spacetime is an appealing goal. However, the helically symmetric code fails to converge if we extend the outer radius beyond a few wavelengths. In the next chapter, I will discuss the use of toy models to isolate terms that appear responsible for divergence outside the near zone, in an attempt to find methods which can expand the convergence of the helically symmetric binary neutron star code.

Chapter 5

Toy model of helical symmetry

5.1 Introduction

The approximation of full helical symmetry is designed to improve the accuracy of initial data in the near zone, where the coulomb part of the fields is much larger than the radiative part, by including terms ignored in assuming spatial conformal flatness. Solutions with exact helical symmetry and waveless solutions should each be accurate in the near zone, and the work described in Chapter 4 finds that they coincide.

We present results from a number of related nonlinear scalar field models in which convergence requires either a small coefficient of the nonlinear term or a boundary close to the source. The results of these toy models are surprising in two ways. First, convergence of the scalar-field models is most strongly affected by the sign of the source term, with one choice of sign yielding a convergent solution for remarkably large values of the nonlinear terms we examined. For the other sign, convergence requirements set an upper limit on the coefficient of the nonlinear term.

Second, convergence does not depend strongly on the iterative method used to solve the equation, on whether one uses, for example, a Newton-Raphson iteration or an iteration based on a Green function that inverts only a convenient part of the second-order nonlinear operator.

5.2 Scalar Field Model

Can we improve convergence of helically symmetric code through a modification of the algorithm? Is the KEH iteration insufficient? In this section we turn to toy scalar field models for helically symmetric spacetimes, with the addition of nonlinear terms that mimic those found in Uryu's formulation of the Einstein equations. We compare the iteration method used in the Uryu code to more sophisticated methods developed by Andrade et al. [74] and further by Bromley, Owen, and Price [76].

The Uryu code uses the KEH method of splitting off the flat-space operator for direct iteration. Similar KEH codes were developed at UWM for the scalar field with this method, which is the same as the 'direct iteration' of [74] and [76], although implemented with spherical harmonic instead of Fourier decomposition. As mentioned in [74], this method is expected to break down for very strong nonlinearities. The alternate numerical methods we compare use a Newton-Raphson type of iteration instead of direct iteration. The finite difference code linearizes the full operation at each iteration as a more robust but computationally intensive method, and the eigenspectral method of [76] uses coordinates adapted to the particular problem for a similar, but less computationally intensive, iteration procedure.

By determining the range of convergence for representative nonlinear terms, we identify problematic nonlinearities in the full Einstein equations and possible methods for accommodating them.

5.3 Problem specification

We consider a scalar field ψ on Minkowski space, satisfying a wave equation with a source s that mimics two objects in circular orbit and with a nonlinear term $\mathcal{N}[\psi]$, whose strength is adjusted by a coefficient λ:

$$\Box\psi - \lambda\mathcal{N}[\psi] = s. \tag{5.1}$$

We use three different nonlinear terms: $\mathcal{N}[\psi] = \psi^3$, $\mathcal{N}[\psi] = |\nabla\psi|^2$ with ∇ the spatial gradient, and $\mathcal{N}[\psi] = \psi\Box\psi$, chosen to represent the types of nonlinear terms that appear in dynamical components of the field equations.

The source s is a sum of two 3-dimensional Gaussian distributions,

$$s(t,r,\theta,\phi) = \sum_{\pm} \frac{q}{\sqrt{(2\pi)^3}} \ \exp\left(-\frac{(\mathbf{r} \pm \mathbf{R(t)})^2}{\sigma^2}\right), \tag{5.2}$$

centred about points $\pm\mathbf{R}$, $\mathbf{R}(t) = a\,[\cos(\Omega t)\hat{\mathbf{x}} + \sin(\Omega t)\hat{\mathbf{y}}]$, each a distance a from the origin and each having spread σ^2 and total charge q. The source s is stationary in a frame moving with angular velocity Ω; that is, it is Lie-derived by the helical Killing vector

$$k^\alpha = t^\alpha + \Omega\phi^\alpha \tag{5.3}$$

of Minkowski space, where t^α and ϕ^α (equivalently ∂_t and ∂_ϕ) are generators of time-translations and of rotations in the plane of the binary source.

One can regard the scalar-field models as toy models of neutron stars of mass M, if the charge q of each Gaussian source is identified with $4\pi M$. In gravitational units (G=c=1), all quantities of a binary star system can be specified in terms of M. In the models presented below, we set $q = 1$, $a = 1$, $\sigma = 0.5$, and $\Omega = 0.3$, corresponding to a binary system of mass M, stellar separation $2a = 8\pi M$, stellar radius $\sigma = 2\pi M$, and velocity $v = a\Omega = 0.3$.

A helically symmetric solution, like a genuinely stationary solution, is given by its value on a spacelike slice and the field equation (5.1) can be written in a form that involves only spatial derivatives. That is, using the symmetry relation

$$\pounds_k\psi = (\partial_t + \Omega\partial_\phi)\psi = 0 \tag{5.4}$$

to replace time derivatives by ϕ derivatives, one can rewrite Eq. (5.1) at $t = 0$ in the spatial form,

$$(\nabla^2 - \Omega^2\partial_\phi^2)\Psi - \lambda\mathcal{N}[\Psi] = S, \tag{5.5}$$

where

$$\Psi(r,\theta,\phi) = \psi(t=0,r,\theta,\phi),\ \ S(r,\theta,\phi) = s(t=0,r,\theta,\phi). \tag{5.6}$$

Then

$$\psi(t,r,\theta,\phi) = \Psi(r,\theta,\phi - \Omega t). \tag{5.7}$$

The operator

$$\mathcal{L} := \nabla^2 - \Omega^2\partial_\phi^2 \tag{5.8}$$

has a mixed character, elliptic inside the light cylinder $\Omega\sqrt{x^2+y^2}=1$, hyperbolic outside. Some difficulties in finding numerical solutions stem from this behaviour. In finding an iterative solution, one inverts the operator $\mathcal{L}$, but $\mathcal{L}$ is not negative, and it lacks the contraction property that underlies the convergence of iterative schemes used to invert nonlinear elliptic equations and to prove existence of exact solutions.

5.4 Methods used in model problems

5.4.1 KEH method

In the KEH method one splits off the linear, flat-space operator $\mathcal{L}$ and inverts it by a choice $\mathcal{L}^{-1}$ of Green function. The iterative solution, beginning with $\Psi_0 = \mathcal{L}^{-1}S$, is then given by

$$\Psi_{n+1} = \Psi_0 + \lambda\mathcal{L}^{-1}\mathcal{N}[\Psi_n] \tag{5.9}$$

Although $\mathcal{L}$ is not elliptic, the operator associated with each spherical harmonic is the elliptic Helmholtz operator:

$$\mathcal{L}[\Psi_{lm}(r)Y_{lm}] = [\nabla^2 + m^2\Omega^2][\Psi_{lm}(r)Y_{lm}]. \tag{5.10}$$

The corresponding radial operator

$$\frac{d^2}{dr^2} + \frac{2}{r}\frac{d}{dr} - \frac{l(l+1)}{r^2} + m^2\Omega^2 \tag{5.11}$$

has as its eigenfunctions the spherical Bessel functions, from which a Green function is constructed. We choose as $\mathcal{L}^{-1}$ the form that, for a bounded source, yields the half-advanced+half-retarded solution, namely

$$\mathcal{L}^{-1}S := \sum_{lm}\int dr' S_{lm}(r')g_{lm}(r,r')Y_{lm}(\theta,\phi), \tag{5.12}$$

with

$$g_{l0} = \frac{1}{2l+1}\frac{r_<^l}{r_>^{l+1}}, \qquad g_{lm} = m\Omega j_l(m\Omega r_<)n_l(m\Omega r_>),\ m\neq 0. \tag{5.13}$$

Here $r_< = \min(r,r')$, $r_> = \max(r,r')$, and $j_l(x)$ and $n_l(x)$ are the spherical Bessel functions of the first and second kinds.

At each iteration, the nonlinear term $\mathcal{N}[\Psi_n]$ serves as an effective source. The polynomial nonlinear function Ψ^3 is most easily computed by shifting from $\Psi_{lm}(r)$

back into $\Psi(r,\theta,\phi)$ and cubing at each point, while the derivative-based nonlinear terms, $|\nabla\Psi|^2$ and $\Psi\Box\Psi$, are calculated using the properties of the spherical harmonics.

Finally, as is usual in codes to solve nonlinear elliptic equations, we use softening and continuation to extend the range of convergence to larger values of λ. That is, instead of using Ψ_{n+1} as defined in Eq. (5.9), we can use a softened Ψ^{ω}_{n+1} defined by

$$\Psi^{\omega}_{n+1} = \omega\Psi_{n+1} + (1-\omega)\Psi_n. \tag{5.14}$$

where the softening parameter ω typically ranges from 1 (no softening) to 0.1. Given a converged field solution for some nonlinearity with small λ, it is sometimes possible to use continuation to obtain a solution for larger λ: The converged solution to Eq. (5.5) with small λ is used as the initial field Ψ_0 for the iteration of Eq. (5.9) for larger λ. In this way one moves along a sequence of solutions with increasing values of λ. The effectiveness of softening and convergence is explored in Sec. 5.6.

5.4.2 Finite difference and eigenspectral methods

The finite difference code uses an iteration based on the Newton-Raphson method, with numerical approximations that reduce it in part to a secant method. Write the equation to be solved as

$$F = \mathcal{L}\Psi - \lambda\mathcal{N}[\Psi] - S = 0. \tag{5.15}$$

Numerically, Ψ is given by a set of values Ψ_i on the three-dimensional spatial slice. Given an initial field value Ψ_i, each iterative step generates a modification $\delta\Psi_i$ by inverting

$$J_{ij}\delta\Psi_j = -F_i \tag{5.16}$$

where J_{ij} is the Jacobian

$$J_{ij} = \frac{\partial F_i}{\partial \Psi_j}. \tag{5.17}$$

The Helmholtz operator has the form $(\mathcal{L}\Psi)_i = L_{ij}\Psi_j$ where L_{ij} is constructed from finite difference operations and incorporates boundary conditions. The corresponding part of J_{ij} is simple.

$$J_{ij} = \frac{\partial}{\partial\Psi_j}\left[L_{ik}\Psi_k - \lambda(\mathcal{N}[\Psi])_i - S_i\right] \tag{5.18}$$

$$= L_{ij} - \lambda\frac{\partial\mathcal{N}[\Psi]_i}{\partial\Psi_j}. \tag{5.19}$$

The nonlinear piece of the Jacobian is evaluated numerically by varying local field values to estimate derivatives.

The eigenspectral code [76] uses the same iterative scheme as the finite difference method, but it employs adapted coordinates and a discretized spectral decomposition. To specify the adapted coordinate system, we begin with rotating Cartesian coordinates $(\tilde{x}, \tilde{y}, \tilde{z})$ where the $\tilde{z}$-axis is the axis of rotation. The axes are rotated to a set

$$\tilde{X} = \tilde{y}, \quad \tilde{Y} = \tilde{z}, \quad \tilde{Z} = \tilde{x} \tag{5.20}$$

for which the $\tilde{Z}$-axis is a line through the centre of each source. The adapted coordinates are chosen to approach spherical polar coordinates, with Θ measured from the $\tilde{Z}$ axis, far from the sources. For each point $(\tilde{X}, \tilde{Y}, \tilde{Z})$, let r_1 and r_2 be the distances from the source centres, θ_1 and θ_2 corresponding angles from the $\tilde{Z}$ axis. Then,

$$r_1 = \sqrt{(\tilde{Z} - a)^2 + \tilde{X}^2 + \tilde{Y}^2}, \tag{5.21}$$

$$r_2 = \sqrt{(\tilde{Z} + a)^2 + \tilde{X}^2 + \tilde{Y}^2}. \tag{5.22}$$

The adapted coordinates are

$$\chi = \sqrt{r_1 r_2} \tag{5.23}$$

$$\Theta = \frac{1}{2}(\theta_1 + \theta_2) = \frac{1}{2}\tan^{-1}\left(\frac{2\tilde{Z}\sqrt{\tilde{X}^2 + \tilde{Y}^2}}{\tilde{Z}^2 - a^2 - \tilde{X}^2 - \tilde{Y}^2}\right) \tag{5.24}$$

$$\Phi = \tan^{-1}(\tilde{X}/\tilde{Y}). \tag{5.25}$$

The spectral decomposition involves the angular Laplacian of Θ and Φ,

$$D^2\Psi := \frac{1}{\sin\Theta}\frac{\partial}{\partial\Theta}\left[\sin\Theta\frac{\partial}{\partial\Theta}\right]\Psi + \frac{1}{(\sin\Theta)^2}\frac{\partial^2}{\partial\Phi^2}\Psi. \tag{5.26}$$

Note that D^2 is *not* the angular part of ∇^2 in adapted coordinates, but it agrees asymptotically with the usual angular Laplacian far from the source. Instead of the spherical harmonics of the continuum Laplacian D^2, the eigenspectral code uses the exact eigenvectors of the matrix L obtained by discretizing D^2 on the adapted coordinate grid $\{\Theta_i, \Phi_j\}$, labelling points by i and j. Angular derivatives are represented in L by second order finite differencing. With $[\sin\Theta D^2\Psi](\Theta_a, \Phi_b) \simeq \sum_{ij} L_{ab,ij}\Psi(\Theta_i, \Phi_j)$, the k-labelled normalized eigenvectors $Y_{ij}^{(k)}$ of the matrix $L_{ab,ij}$ satisfy

$$\sum_{ij} L_{ab,ij} Y_{ij}^{(k)} = -\Lambda^{(k)} \sin\Theta_a Y_{ab}^{(k)}, \tag{5.27}$$

$$\sum_{ij} Y_{ij}^{(k)} Y_{ij}^{(k')} \sin \Theta_i \Delta\Theta \Delta\Phi = \delta_{kk'}. \qquad (5.28)$$

We expand the field in terms of the eigenvectors $Y_{ij}^{(k)}$,

$$\Psi(\chi, \Theta_i, \Phi_j) = \sum_k a^{(k)}(\chi) Y_{ij}^{(k)}, \qquad (5.29)$$

and write the operator $\mathcal{L}$ in terms of adapted coordinates (Eqs. (8–17) of [76]). $\mathcal{L}\Psi$ is expressed in terms of eigenvectors $Y_{ij}^{(k)}$ (Eq. (31) of [76]),

$$\sum_k \left(\alpha_{k',k} \frac{d^2 a^{(k)}(\chi)}{d\chi^2} + \beta_{k',k} a^{(k)}(\chi) + \gamma_{k',k} \frac{d a^{(k)}(\chi)}{d\chi} \right) = S_{k'} \ , \qquad (5.30)$$

where the $\alpha_{k',k}, \beta_{k',k}$, and $\gamma_{k',k}$ involve angular derivatives of the $Y^{(k)}$ computed by finite differencing (Eqs. (41-43) of [76]). This equation for $a^{(k)}$ is iterated in the same fashion as in the finite difference method to find the solution with nonlinear terms.

If all harmonics were retained, the eigenspectral method would be the equivalent of the finite difference method in adapted coordinates, although in a different basis. The advantage of the adapted coordinates is that the distribution of points encodes most of the physically relevant information in the low-order harmonics. Its disadvantage is that higher order harmonics require an increasingly cumbersome formalism. The code is consequently limited to harmonics ≤ 2, saving enough memory to allow high resolution in the radial coordinate.

5.4.3 Boundary conditions

The KEH method at each iteration finds a solution which has standing wave behaviour for the flat space piece, imposing boundary conditions by the choice of Green's function. It is assumed that the flat-space boundary conditions are an adequate approximation to those of the full problem with nonlinearities added. There remains freedom to add a homogeneous solution at each iteration. This can be used to impose a stricter boundary condition, and estimate the effect an improper boundary condition has on the behaviour of the solution near the sources.

The eigenspectral and finite difference methods include boundary conditions in the finite difference matrix for the linear $\Box$ operator. Outgoing wave conditions are imposed on the edges of the grid by enforcing the Sommerfeld condition ($\partial_r \psi +$

$\partial_t\psi)_{r=r_{max}} = 0$, which becomes, after imposing helical symmetry and transforming to adapted coordinates,

$$\partial_\chi \Psi = -\Omega \left(\tilde{Z}\partial_{\tilde{X}}\Psi - \tilde{X}\partial_{\tilde{Y}}\Psi \right), \tag{5.31}$$

for $r \gg a$ where $\chi \to r$.

A solution for ingoing radiation can then be generated by a spatial inversion across the plane through the sources and perpendicular to their rotation. At each step, a periodic solution is constructed by superposing the ingoing and outgoing solutions.

5.5 Estimating numerical accuracy

Several types of numerical approximation in the KEH code produce inaccuracies that can be estimated by convergence testing. Most obvious is the choice of spatial grid in (r, θ, ϕ) on which numerical integration is performed. Very high resolution in θ and ϕ is easily obtained. The number of radial points is more problematic with our simple equally spaced grids. A Richardson extrapolation error estimate from varying radial grid spacing shows that a precision of 10^{-5} is estimated for runs comparing code results. Estimation of the range of λ giving convergent solutions is done at lower radial precision.

As the KEH method rests on the decomposition of the field into spherical harmonics, accuracy will depend on the number of harmonics retained in the numerical calculation. Examining the difference between results with an increasing number of harmonics retained shows that a good approximation is to use up to $l = 12$ in the code. The fractional difference between the field calculated with $l_{\max} = 12$ and the field including higher harmonics is less than 10^{-6} at each point.

In the toy models presented below, a solution is computed at each iteration using the half-advanced+half-retarded Green function (5.12). Because the linear field Ψ of a perpetually radiating source falls off like r^{-1}, the nonlinear terms $\mathcal{N} = (\nabla\Psi)^2$ and $\mathcal{N} = \Psi\Box\Psi$ that serve as effective sources for each iteration do not fall off fast enough for the integrals to converge, if the outer boundary extends to infinity. One can, however, pick out a solution that is independent of the outer boundary by fixing the value of Ψ at a finite radius R. That is, one can, at each iteration, add the homogeneous solution that maintains the specified value of Ψ at R. This has remarkably little effect on the field in the region close to the sources, with less that a 1% change in field strength for points with $r < 6$. This insensitivity of the near-zone field to the amplitude of the waves, when the source dominates the solution, is the reason a helically symmetric solution makes sense as an approximation to an outgoing solution.

The finite difference code is iterated to a 10^{-11} RMS difference in field between subsequent iterations. Analysis of errors and comparison to the eigenspectral code is found in [74].

5.5.1 Comparing codes

With different 3D grid patterns for the codes, it was most straightforward to compare results on rays through the volume of interest. We compared the results extrapolated to three axes: the x-axis through the centres of the two sources, the z-axis of rotation, and the third y-axis perpendicular to the x-axis in the plane of rotation. Both x and y axes show wave behaviour away from the sources; along the z axis ψ shows only Coulomb type effects Coulomb-type behaviour, because Y_{lm} vanishes on the axis when $m \neq 0$, and for $m = 0$, $\mathcal{L}\psi = \nabla^2\psi$. Some sample comparison plots are shown in Fig. 20.

The field values on the rays were interpolated for comparison. Differences between fields were divided by the average field value of the three codes to find relative error, as plotted in the insets of Fig. 20. We computed the RMS of this relative error for the grid points along each ray. These RMS values are expressed as percentages in Table 5. In the worst case, the RMS difference is 3% between codes.

We note that a smaller RMS difference on the rotation axis than on the source and perpendicular axes indicates that discrepancies in the wave region dominate, as in the FD-KEH comparison with $\mathcal{N}[\Psi] = \Psi^3$, $\lambda = 100$. In other cases, the error on all three axes is comparable, and there is some shift between codes seen even on the rotation axis, as in the FD-KEH comparison with $\mathcal{N}[\Psi] = |\nabla\Psi|^2$, $\lambda = 3$.

5.6 Measuring range of convergence

For each code, a series of runs varying the nonlinear amplitude λ determined the range of λ for which the code gave a convergent solution. The source distribution and boundary location were fixed.

Softening and continuation are used to extend the maximum absolute value of λ

Table 5 : A comparison of code output for scalar models. The values in the table give the percent RMS difference between Ψ-values from three numerical methods as in Fig. 1. The RMS differences were computed from the points along each principal axis.

	Source axis	Perp. axis	Rotation axis
Linear ($\mathcal{N}[\Psi] = 0$)			
FD to KEH	0.25	0.24	0.10
FD to ES	1.02	1.09	1.08
ES to KEH	1.07	1.15	1.11
$\mathcal{N}[\Psi] = \Psi^3$, $\lambda = 100$			
FD to KEH	3.56	3.44	0.21
FD to ES	1.22	1.67	1.14
ES to KEH	3.28	2.86	1.19
$\mathcal{N}[\Psi] = \Psi^3$, $\lambda = -2.2$			
FD to KEH	0.35	0.36	0.21
FD to ES	1.96	2.02	2.08
ES to KEH	1.77	1.99	1.92
$\mathcal{N}[\Psi] = \lvert\nabla\Psi\rvert^2$, $\lambda = 3$			
FD to KEH	1.73	1.47	1.33
FD to ES	1.39	1.80	1.44
ES to KEH	2.69	2.76	2.77
$\mathcal{N}[\Psi] = \lvert\nabla\Psi\rvert^2$, $\lambda = -100$			
ES to KEH	1.96	2.20	1.65
$\mathcal{N}[\Psi] = \Psi\Box\Psi$, $\lambda = -0.7$			
FD to KEH	0.53	0.48	0.20
FD to ES	1.06	1.13	1.13
ES to KEH	0.99	1.23	1.00

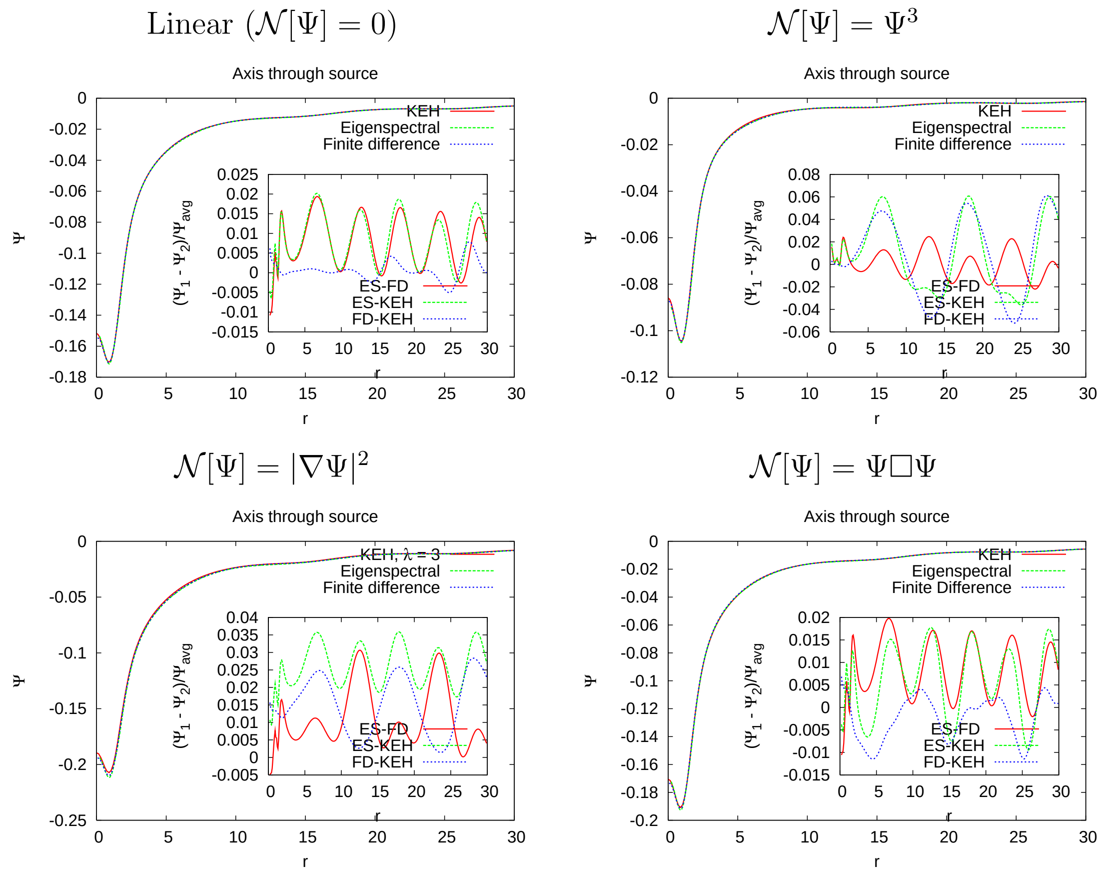

Figure 20 : The scalar field Ψ as a function of distance r from the origin in units of the orbital radii along the source axis. Each of the four panels corresponds to a unique model, as specified by the form of the nonlinear term, $\mathcal{N}$, written above it. In all cases, the angular frequency of rotation is $\Omega = 0.3$ and the source strengths are unity. The plots show results from the KEH method (solid curves), the eigenspectral method (dashed) and the finite difference code (dotted). The insets give more detailed comparisons between these results; the curves are the difference between pairs of solutions relative to the average field. Note that the eigenspectral method gives a periodic modulation relative to the other methods, as a result of the use of only low-order harmonics.

that allows convergence. For each nonlinear term, strikingly different behaviour is found for opposite signs of λ. That is, denoting by $\lambda_{\rm max}$ and $\lambda_{\rm min}$ the largest positive value and the smallest negative value of λ for which a code converges, we find for each nonlinear term that $\lambda_{\rm max}$ and $|\lambda_{\rm min}|$ differ by at least a factor of 100. In each case, the sign of λ that yields greatest convergence is opposite to the sign of the source term, where the source is large. The 'favourable' sign damps the effect of the source distribution on the field, while the 'unfavourable' sign gives an amplified effective

Table 6 : The range of nonlinear amplitude λ in scalar models for which codes converged. The first column gives the type of nonlinearity, while the second column indicates the numerical method, as discussed in the text. The third and fourth columns, showing $\lambda_{\min}$ and $\lambda_{\max}$, give the range of λ for which convergence was achieved. Where an inequality is given, no limiting value was found.

$\mathcal{N}[\Psi]$	Code	$\lambda_{\min}$	$\lambda_{\max}$
Ψ^3	KEH	-2.3	11
Ψ^3	KEH, softened/continued	-2.3	>10000
Ψ^3	FD	-2.5	>1000
Ψ^3	ES	-2.4	>1000
$\|\nabla\Psi\|^2$	KEH	-30	7.7
$\|\nabla\Psi\|^2$	KEH, softened/continued	< -1000	7.7
$\|\nabla\Psi\|^2$	FD	-2.0	5.6
$\|\nabla\Psi\|^2$	ES	-360	7.3
$\|\nabla\Psi\|^2$	ES, continued	< -1000	7.3
$\Psi\Box\Psi$	KEH	-0.96	1.3
$\Psi\Box\Psi$	KEH, softened/continued	-0.96	10
$\Psi\Box\Psi$	FD	-1.8	>1000
$\Psi\Box\Psi$	ES	-1.7	>1000

source. For $\mathcal{N}[\Psi] = \Psi^3, |\nabla\Psi|^2, \Psi\Box\Psi$, the favourable signs of lambda are $+, -, +$, respectively.

Softening and continuation improved the range of convergence in the direction of the favourable sign, but had no effect on the limit of the unfavourable signed λ. Fig. 21 shows the effect of softening, parameterized by ω, and of using continuation on the limiting favourable-sign values of λ.

Convergence is attained, if softening and continuation are allowed, for all attempted favourable sign values for λ, except when using the KEH method with the $\Psi\Box\Psi$ nonlinear term or when using the finite difference method with the $|\nabla\Psi|^2$ nonlinear term.

The range of convergence results are given in Table 6. If softening and continuation maintain convergence to the largest tested value of λ, the uncertainty in the true maximum value or minimum value of λ is indicated by $>$ or $<$.

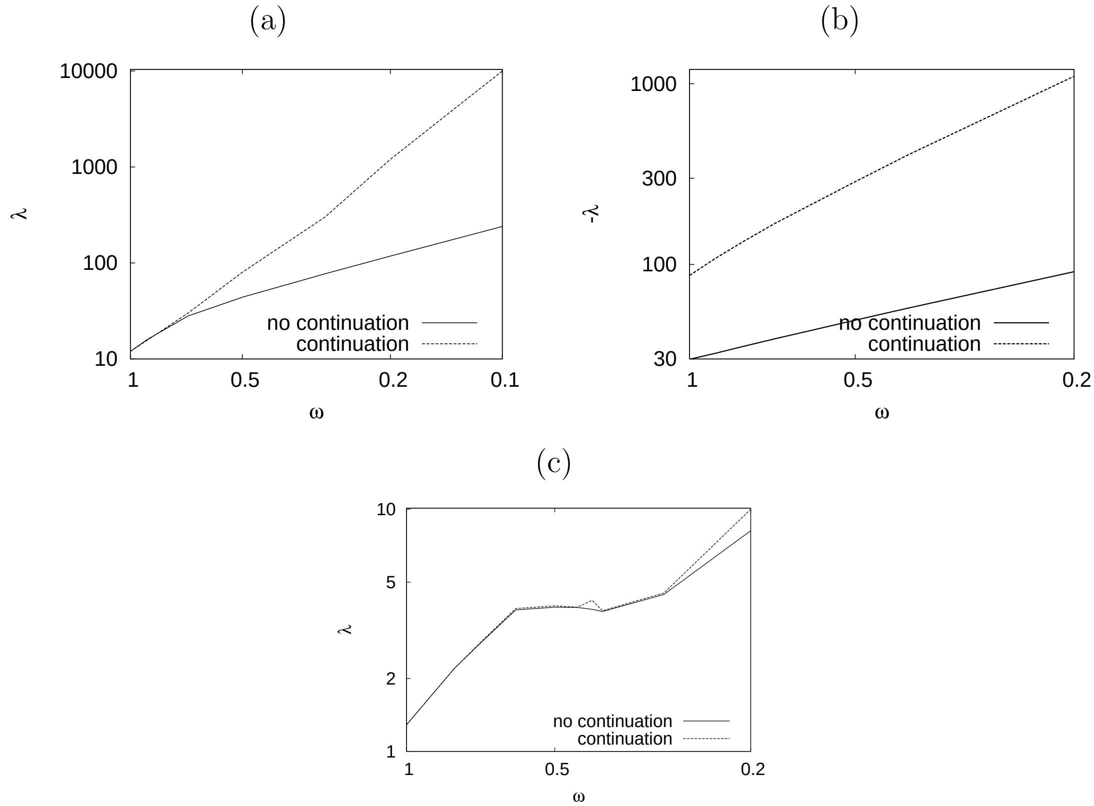

Figure 21 : The effect of a softening parameter ω and continuation on range of λ. The plots indicate the limiting value of λ for convergence of the KEH code. Each panel corresponds to a different nonlinear model, with $\mathcal{N}[\Psi]$ set to Ψ^3 (panel a), $|\nabla\Psi|^2$ (panel b), and $\Psi\Box\Psi$ (panel c). In each case, the limiting λ value of the opposite sign was unaffected by softening or continuation.

5.7 Boundary and convergence

As described in Sec. 4.4.6, Uryu has obtained a convergent helically symmetric BNS code within a region that extends about one wavelength of the source, by using a waveless formulation outside that radius. Led by this result, we explored the effects of the outer boundary placement on the range of converging λ for the fully helical code.

While bringing the boundary in had little effect on the limits of the favourably signed λ, it did allow for a larger magnitude unfavourable λ, as shown in Fig. 22a. However, these runs also exposed a danger in the unfavourable sign of λ, as seen in Fig. 22b. Previous tests had shown that linear field solution and the $\lambda = 100$ solution were fairly insensitive to boundary placement, showing convergence of the nonlinear solutions as the outer boundary was increased. However, the unfavourable $\lambda = -2.2$ did not show this behaviour, diverging as the maximum grid radius was moved outwards. A moderate $\lambda = -1.0$ run showed that convergence with respect to outer boundary was possible for unfavourable sign λ of smaller magnitude.

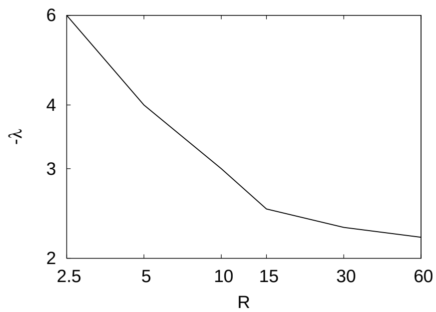

(a)

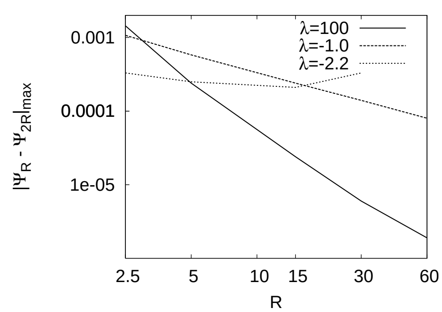

(b)

Figure 22 : (a) The effect of the outer boundary R on convergence in the cubic nonlinear model ($\mathcal{N}[\Psi] = \Psi^3$). The limiting value of λ for which the KEH method converges as a function of outer boundary location, R, in units of orbital radii a. (b) Effect of outer boundary R on the field solution. For both, he nonlinear term is $\mathcal{N}[\Psi] = \Psi^3$. For $\lambda = -2.2$, divergence of iterations when $R = 120$ prevents evaluating $\Psi_R - \Psi_{2R}$ at $R = 60$.

5.8 Conclusions

The work done with toy models suggests that the lack of convergence of fully helically symmetric initial data is intractable—one cannot change the sign of the diverging terms in the Einstein equations cannot be controlled. However, as discussed in Chapter 4, solutions with full helical symmetry in the near zone agree well with solutions using the waveless approximation. This implies that the two methods can be used interchangeably to generate improved quasiequilibrium sequences or initial data. The waveless approximation has the additional advantage that a nonzero radial velocity can be accommodated, leading to initial data which minimizes eccentricity in full numerical simulations.

Part III

Gravitational radiation and the equation of state

Chapter 6

Wave production and analysis

6.1 Post-Newtonian approximations

Post-Newtonian calculations of waveforms make use of expanded expressions for the orbital energy and luminosity of two orbiting point particles. A useful overview is given in [77]. As in the quasiequilibria of Chapter 4, the binary is modelled at each instant via a secular evolution of a quasi-circular orbit. For quasi-circular orbits, the parameter of the post-Newtonian (PN) expansion can be chosen in terms of coordinate separation or frequency. In terms of orbital frequency Ω, as observed at infinity, the PN parameter is

$$x = \left(\frac{GM\Omega}{c^3}\right)^{2/3}, \tag{6.1}$$

where M is total mass. To first post-Newtonian order,

$$x \sim \frac{GM}{c^2 r}, \tag{6.2}$$

where r is the orbital radius.

The orbital energy and luminosity have been calculated to 3.5 PN order. With m_1 and m_2 the masses of the individual components, $\eta = m_1 m_2 / M^2$ is the dimensionless reduced mass, taking values between 0 in the test particle limit and 1/4 in the equal mass case. From [78]:

$$\begin{aligned} E = -\frac{1}{2} M c^2 \eta x \Bigg[1 &- \left(\frac{3}{4} + \frac{1}{12}\eta\right) x - \left(\frac{27}{8} - \frac{19}{8}\eta + \frac{1}{24}\eta^2\right) x^2 \\ &- \left\{ \frac{675}{64} - \left(\frac{34\,445}{576} - \frac{205}{96}\pi^2\right)\eta + \frac{155}{96}\eta^2 + \frac{35}{5184}\eta^3 \right\} x^3 \Bigg] \end{aligned} \tag{6.3}$$

$$\mathcal{L} = \frac{32}{5}\frac{c^5}{G}\eta^2 x^5 \left[1 - \left(\frac{1247}{336} + \frac{35}{12}\eta\right) x + 4\pi x^{3/2} \right.$$
$$- \left(\frac{44\,711}{9072} - \frac{9271}{504}\eta - \frac{65}{18}\eta^2\right) x^2 - \left(\frac{8191}{672} + \frac{583}{24}\eta\right) \pi x^{5/2}$$
$$+ \left\{\frac{6\,643\,739\,519}{69\,854\,400} + \frac{16}{3}\pi^2 - \frac{1712}{105}\gamma - \frac{856}{105}\ln(16x) \right. \tag{6.4}$$
$$\left. - \left(\frac{134\,543}{7776} - \frac{41}{48}\pi^2\right)\eta - \frac{94\,403}{3024}\eta^2 - \frac{775}{324}\eta^3\right\} x^3$$
$$\left. + \left(-\frac{16\,285}{504} + \frac{214\,745}{1728}\eta + \frac{193\,385}{3024}\eta^2\right) \pi x^{7/2}\right].$$

Here $\gamma = 0.5772\ldots$ is Euler's constant.

The time evolution of x can be calculated by equating the change in orbital energy to the amount of energy radiated

$$\frac{dE}{dt} = -\mathcal{L}, \tag{6.5}$$

to give

$$\frac{dx}{dt} = -\frac{\mathcal{L}}{(dE/dx)} \tag{6.6}$$

while the orbital phase Φ is then evolved using the orbital frequency $\Omega = d\Phi/dt$ in Eq. (6.1):

$$\frac{d\Phi}{dt} = \frac{c^3}{GM} x^{3/2}. \tag{6.7}$$

Various PN approximants can use different methods of solving these equations at the same post-Newtonian order; these lead to different orbital evolutions depending on how higher-order terms are truncated. The Taylor-expansions TaylorT1, TaylorT2, and TaylorT3 of [79] were augmented by TaylorT4 in [77]. TaylorT1 is direct numerical integration. TaylorT2 and TaylorT3 are term-by-term analytical evaluations of integrals for $\{t(x), \Phi(x)\}$ and $\{x(t), \Phi(t)\}$ respectively. TaylorT4 truncates Eqs. (6.6) and (6.7) at the desired post-Newtonian order before integrating. TaylorT4 is shown empirically [77] to agree closely with fully relativistic binary black hole simulations over tens of cycles, until roughly the last orbit before merger. This agreement is coincidental, as Taylor T4 departs from the numerical simulations in other characteristic behaviours [80], but it allows the use of TaylorT4 as a waveform closely representative of full binary black hole evolutions up to just before merger.

The 3.5PN truncated form of Eq. (6.6) is

$$\begin{aligned}\frac{dx}{dt} = \frac{64}{5}\frac{c^3}{G}\frac{x^5\eta}{M}\Bigg[1 &- \left(\frac{743}{336} + \frac{11}{4}\eta\right)x + 4\pi x^{3/2} \\ &+ \left(\frac{34\,103}{18\,144} + \frac{13\,661}{2016}\eta + \frac{59}{18}\eta^2\right)x^2 - \left(\frac{4159}{672} + \frac{189}{8}\eta\right)\pi x^{5/2} \\ &+ \Bigg\{\frac{16\,447\,322\,263}{139\,708\,800} + \frac{16}{3}\pi^2 - \frac{1712}{105}\gamma - \left(\frac{56\,198\,689}{217\,728} - \frac{451}{48}\pi^2\right)\eta \\ &\quad + \frac{541}{896}\eta^2 + \frac{5605}{2592}\eta^3 - \frac{856}{105}\ln(16x)\Bigg\}x^3 \\ &+ \left(-\frac{4415}{4032} + \frac{358\,675}{6048}\eta + \frac{91\,495}{1512}\eta^2\right)\pi x^{7/2}\Bigg]. \end{aligned} \tag{6.8}$$

6.1.1 Time-domain waveform

Given the orbital evolution equations, one can determine the gravitational radiation emitted by the system. The amplitude of these waves can be calculated from the multipole moments of the post-Newtonian source to successive post-Newtonian orders. The phase of the dominant $m = 2$ quadrupole-moment gravitational waves ϕ can be written as twice the orbital phase Φ, plus corrections from high-order imaginary parts in the amplitude terms.

The gravitational waves emitted in all directions can be encoded by decomposing the waves themselves in terms of spin-weighted spherical harmonics. For near-equal mass binaries, the $(l, m) = (2, 2)$ mode is much larger than other modes [81]. This component can be calculated for point particles in terms of x and Φ above, after absorbing frequency scale terms into the phase at 4PN order, to be at 3PN order [82]:

$$
\begin{aligned}
h_{(2,2)} = -8\sqrt{\frac{\pi}{5}}\frac{G}{c^2}\frac{M\eta}{D}e^{-2i\Phi}x\Bigg[1 &- \left(\frac{107}{42}-\frac{55}{42}\eta\right)x + 2\pi x^{3/2} \\
&- \left(\frac{2173}{1512}+\frac{1069}{216}\eta-\frac{2047}{1512}\eta^2\right)x^2 \\
&- \left\{\left(\frac{107}{21}-\frac{34}{21}\eta\right)\pi + 24i\eta\right\}x^{5/2} \\
&+ \left\{\frac{27\,027\,409}{646\,800}-\frac{856}{105}\gamma+\frac{2}{3}\pi^2-\frac{1712}{105}\ln(2)\right. \\
&\quad -\frac{428}{105}\ln x - \left(\frac{278\,185}{33\,264}-\frac{41}{96}\pi^2\right)\eta \\
&\quad \left. -\frac{20\,261}{2772}\eta^2+\frac{114\,635}{99\,792}\eta^3+\frac{428i}{105}\pi\right\}x^3\Bigg]
\end{aligned}
\tag{6.9}
$$

where D is the distance to the observer.

When combined with some solution for $x(t)$ and $\Phi(t)$, this specifies the quadrupole mode of the waveform. Along the rotation axis, the optimal orientation of the binary, this mode gives the polarization waveforms h_+ and $h_\times$

$$h_+^{(z)} - ih_\times^{(z)} = \frac{1}{2}\sqrt{\frac{5}{\pi}}h_{(2,2)} \tag{6.10}$$

which, in the restricted PN approximation with quadrupole formula amplitude, are

$$h_+^{(z)} - ih_\times^{(z)} = -4\frac{G}{c^2}\frac{M\eta}{D}x\,e^{-2i\Phi}. \tag{6.11}$$

The amplitude of the $(2,2)$ mode is the absolute value of the complex $h_{(2,2)}$ above, which is independent of the phase, and the frequency is defined at a time t before the coalescence t_c by

$$f_{3PN}(t,t_c) = \frac{1}{\pi}\frac{x(t_c-t)^{3/2}}{GMc^{-3}}. \tag{6.12}$$

6.1.2 Other multipoles

Higher multipole contributions to the gravitational radiation are proportional to $\delta M = m_1 - m_2$ or of higher post-Newtonian order. BH-NS systems can have $\delta M \sim M$, adding at next highest amplitude and half the frequency

$$h_{(2,1)} = -\frac{8i}{3}\sqrt{\frac{\pi}{5}}\frac{G}{c^2}\frac{\delta M\,\eta}{D}e^{-i\Phi}x^{3/2}\left(1-\left(\frac{17}{28}-\frac{5}{7}\eta\right)x+\left(\pi-\frac{i}{2}-2i\ln 2\right)x^{3/2}\right.$$
$$\left.-\left(\frac{43}{126}+\frac{509}{126}\eta-\frac{79}{168}\eta^2\right)x^2+O(x^{5/2})\right). \tag{6.13}$$

However for NS-NS, $\delta M \lesssim .5M$, and $x \sim 0.01$–0.1 in the relevant frequency range of 50–1000 Hz, so higher multipole radiation will have much smaller amplitude than quadrupole radiation.

6.1.3 Stationary phase approximation

The stationary phase approximation can be used to determine the amplitude of the gravitational waveform's Fourier transform directly from the amplitude of Eq. (6.9) and the time derivative of x given by Eq. (6.6). We require a waveform of the general form

$$B(t) = A(t)\cos[\phi(t)] \tag{6.14}$$

in the limit where

$$\frac{d\ln(A)}{dt} \ll \frac{d\phi}{dt} \tag{6.15}$$

and

$$\frac{d^2\phi}{dt^2} \ll \left(\frac{d\phi}{dt}\right)^2. \tag{6.16}$$

Note that ϕ is the phase of the wave, not the orbital phase Φ. We use the stationary phase approximation[83] to obtain, in terms of an instantaneous frequency

$$f(t) = \frac{1}{2\pi}\frac{d\phi}{dt}, \tag{6.17}$$

the Fourier transform of the waveform

$$\tilde{B}(f) \simeq A(f)\left(\frac{df}{dt}\right)^{-1/2}\exp\left(i\left(2\pi f t_c - \phi(f) - \frac{\pi}{4}\right)\right). \tag{6.18}$$

Since x is related to the gravitational wave frequency f (which is twice the orbital frequency, or Ω/π, for the $m = 2$ mode) by Eq. (6.1), we have

$$\frac{df}{dt} = \frac{1}{\pi}\frac{c^3}{GM}\frac{3}{2}x^{1/2}\frac{dx}{dt}; \tag{6.19}$$

and the amplitude of the Fourier transform can be written entirely in terms of known functions dx/dt of Eq. (6.8) and the amplitude of the polarization waveforms in Eq. (6.10):

$$A = \frac{1}{2}\sqrt{\frac{5}{\pi}}\left|h_{(2,2)}\right| \tag{6.20}$$

$$\phi = \arg h_{(2,2)} \simeq 2\Phi \tag{6.21}$$

The phasing of the Fourier transform requires solving for $\phi(f)$, which can be done numerically in TaylorT4 style using the 3.5PN expression of

$$\frac{d\phi}{df} = \frac{d\phi/dt}{df/dt}. \tag{6.22}$$

6.2 Detection

Consider some polarization waveform $h_+(t), h_\times(t)$ incident on a detector. The detection and parameter estimation methods from such a waveform are outlined below following [83, 84, 85].

The strain produced in a detector, given polarization waveforms h_+ and $h_\times$ incident upon it, is

$$h(t) = \mathcal{F}_+ h_+(t) + \mathcal{F}_\times h_\times(t) \tag{6.23}$$

where $\mathcal{F}_+$, $\mathcal{F}_\times$ are the antenna patterns which depend on the type and orientation of the detector; they are known functions.

For noise described by a one-sided spectral density $S_n(f)$

$$S_n(f) = 2\int_{-\infty}^{\infty} \overline{n(t+\tau)n(t)} e^{-2\pi i f\tau} d\tau, \qquad f < 0, \tag{6.24}$$

an optimal matched filter output ρ can be calculated for a known signal $h(t)$ in the detector output $s(t) = n(t) + h(t)$ by filtering for it after weighting by the inverse of the noise spectrum.

Given two different signals h_1 and h_2, define an inner product for a particular noise spectrum $S_n(f)$ by

$$\langle h_1|h_2\rangle = 4\mathrm{Re}\int_0^{\infty} \frac{\tilde{h}_1(f)\tilde{h}_2^*(f)}{S_n(f)} df. \tag{6.25}$$

This inner product yields a natural metric on a space of waveforms with distance between waveforms weighted by the inverse of the noise. We filter the detector output against an expected waveform h using $\langle s|h\rangle$. Then

$$\rho = \frac{\langle s|h\rangle}{\sqrt{\langle h|h\rangle}} \tag{6.26}$$

is the optimal statistic to detect a waveform of known form h in the signal s [84]. Note that I do not use normalized waveforms in this presentation.

Pure noise has an expectation value of zero, $\overline{N} = \overline{\langle n|h\rangle} = 0$, filtered against some waveform $h(t)$. The expectation value of a signal $s(t) = n(t) + h(t)$ containing the waveform $h(t)$ is therefore

$$\overline{S} = \overline{\langle s|h\rangle} = \langle h|h\rangle. \tag{6.27}$$

The average response of filtering with waveform $h(t)$ to random noise is characterized by

$$\overline{N^2} = \overline{\langle n|h\rangle\langle n|h\rangle} = \langle h|h\rangle \tag{6.28}$$

where the second equality follows from Eqs. (6.24) and (6.25).

The expectation value of ρ is the signal-to-noise ratio or SNR

$$\frac{(\overline{S})^2}{\overline{N^2}} = \overline{\rho}^2, \tag{6.29}$$

and the expected SNR of a particular waveform h in the detector, when filtered against an exact template, is

$$\overline{\rho} = \sqrt{\langle h|h\rangle}. \tag{6.30}$$

For detection one usually wishes to consider a continuous family of related waveforms with shifts in start time τ_0 and phase ϕ_0, but marginalize/optimize over such possible shifts. A nice way to simultaneously search over all possible start times τ_0 is to note that the Fourier transform of a time shifted waveform $h(t - \tau_0)$ is

$$\tilde{h}(f)e^{2\pi i f \tau_0} \tag{6.31}$$

in terms of the transform $\tilde{h}(f)$ of $h(t)$, and this itself acts as an inverse Fourier transformation from f to τ_0, such that one can construct ρ as a function of τ_0 via

$$X(\tau_0) = 2\mathrm{Re} \int_{-\infty}^{\infty} \frac{\tilde{s}(f)\tilde{h}^*(f)}{S_n(|f|)} e^{2\pi i f \tau_0} df \tag{6.32}$$

as

$$\rho(\tau_0) = \frac{X(\tau_0)}{\sqrt{\langle h|h\rangle}}. \tag{6.33}$$

One can generalize further [85] to search over all phase shifts ϕ_0 by constructing the sum of the above output, with template $h(t - \tau_0; \phi_0 = 0)$, with a similar output for a template with a an orthogonal phase shift $h(t - \tau_0; \phi_0 = \pi/2)$, which Fourier transforms as

$$h(t - \tau_0; \phi_0 = \pi/2) \rightarrow \tilde{h}(f) e^{2\pi i f \tau_0} e^{i\pi/2}. \tag{6.34}$$

This yields the quantity

$$Z(\tau_0) = X(\tau_0) + iY(\tau_0) = 4 \int_0^\infty \frac{\tilde{s}(f)\tilde{h}^*(f)}{S_n(f)} e^{2\pi i f \tau_0} df, \tag{6.35}$$

with absolute value $|Z(\tau_0)|$ which is the filter output optimized over all template phases, so that

$$\rho(\tau_0, \phi_{max}) = \frac{|Z(\tau_0)|}{\sqrt{\langle h|h\rangle}}. \tag{6.36}$$

6.3 Parameter estimation

Generally one considers a waveform dependent on a set of M physical parameters θ^A, forming an M-dimensional subspace of gravitational waveforms in a N-dimensional space of possible signals. For a given signal, a perfect detector would find a measured signal lying in this sub-space at the physical parameters. However, one really measures $h + n$, where n is random noise. In the case of Gaussian noise, various realizations of n form a $N - 1$ dimensional Gaussian distribution of measured signals s centred around the true waveform h. Parameter estimation consists of finding the $\hat{\theta}$ which give the best fit to the signal s.

The maximum likelihood criterion is a standard method of choosing best parameters. The probability of measuring s, given that the real waveform is $h(\theta^A)$, is proportional to $\exp(-\langle s - h|s - h\rangle/2)$, where $s - h = n$. The best estimate $\hat{h}(\hat{\theta}^A)$ is value of h at the point $\hat{\theta}^A$ that maximizes this probability. It thus satisfies

$$\left.\frac{\partial}{\partial\theta^i}\langle s - h(\theta^A)|s - h(\theta^A)\rangle\right|_{\theta^i = \hat{\theta}^i} = 0, \tag{6.37}$$

for all $i = 1..M$, which can be reduced to the set of equations

$$\langle s - \hat{h}(\theta^A)|\partial_{\theta^i}\hat{h}(\theta^A)\rangle = 0, \tag{6.38}$$

which imply that $s - \hat{h}$ is orthogonal to variations in all parameters in the surface of $h(\theta)$—it is the point in $h(\theta)$ closest to s using the metric defined in Eq. 6.25.

In the limit of large ρ, one can determine how well the parameters are estimated using the Fisher matrix (for other cases and caveats see [86]). Let $h(\theta^A)$ be the actual waveform, assuming it itself lies on our subspace of parameterized waveforms. An inaccuracy in the measured parameters $\delta\theta^A = \hat{\theta}^A - \theta^A$ corresponds approximately to an estimate $\hat{h}$ that differs from h by

$$h \simeq \hat{h} - \partial_A \hat{h} \delta\theta^A, \tag{6.39}$$

where ∂_A is a vector of $\partial/\partial\theta^i$s. Then Eq. (6.38) becomes

$$\langle \partial_A \hat{h} | \partial_B \hat{h} \rangle \delta\theta^A = \langle n | \partial_B \hat{h} \rangle, \tag{6.40}$$

and, to first order in $\delta\theta^A$,

$$\langle \partial_A h | \partial_B h \rangle \delta\theta^A = \langle n | \partial_B h \rangle. \tag{6.41}$$

The Fisher matrix is the $M \times M$ matrix $\Gamma_{AB} = \langle \partial_A h | \partial_B h \rangle$. Its inverse, $(\Gamma^{-1})^{AB}$, yields

$$\overline{\delta\theta^A \delta\theta^B} = (\Gamma^{-1})^{AB} \tag{6.42}$$

so that the expected error in a given parameter θ^A is

$$\overline{(\delta\theta^A)^2} = (\Gamma^{-1})^{AA} \tag{6.43}$$

and the cross terms of the inverse Fisher matrix yield correlations between different parameters.

This analysis is valid to first order in $1/\rho$ or, equivalently, in $\delta\theta^A$.

6.4 Advanced LIGO noise and tuning

A noise spectrum of coloured Gaussian noise is a useful first approximation to the sensitivity of LIGO type detectors. Advanced LIGO, in particular will be able to be tuned to measure high frequency signals, such as those from binary neutron stars near merger. A starting point for investigating sensitivity to the EOS is the 1150 Hz narrowband tuning, although other detector configurations allow for observation of frequency up to several kilohertz, as seen in Fig. 23.

There are additional broadband and standard tunings for the interferometers, with less sensitivity at high frequency. The reference broadband tuning has been optimized for the burst search, whereas the standard Advanced LIGO configuration is optimized for binary neutron star *detection*.

It is expected that the implementation of narrow banding will happen after an initial period of Advanced LIGO observation with all three detectors. One of the three detectors may then be tuned to a given high frequency for some period of observation; the other detectors will be left in the standard configuration. However, the exact mode of operation of Advanced LIGO is still under discussion, and the scientific case for various configurations will be made on the basis of investigations such as the one we will present in Chapter 7.

6.5 EOS constraint with NS-NS

Existing literature on the possible use of LIGO-style interferometers to constrain neutron star properties has reached mixed conclusions.

A common assumption in considering the potential effects of EOS effect is that the waveform will be essentially point particle up to some sharply-defined innermost stable circular orbit, or ISCO, which may depend on the EOS. The spectrum of such a waveform would follow that of point particles up to a maximum cutoff frequency, that of the ISCO, and then fall off rapidly. This frequency can be considered as the measurable quantity (as in [88], [89]).

Point particle approximations are expected to hold up approximately $r = 4R$, where r is binary separation and R is stellar radius[61]. We approximate the orbital frequency by $\Omega = \sqrt{M/r^3}$, for total mass M, to estimate for two $1.35M_{\cdot}$ stars with radius between 8 and 16 km

$$f \approx \frac{1}{\pi}\sqrt{\frac{M_{\rm tot}}{4\dot{R}}} \approx 400\text{–}1000 \text{ Hz}. \tag{6.44}$$

Lai and Wiseman [90] compute corrections to orbital dynamics from tidal effects and relativistic radiation. Comparing point mass calculations to $\Gamma = 3, R/M = 5$ ellipsoids, in both relativistic and non-relativistic cases, they show a finite size effect on gravitational energy emitted near a given frequency starting at roughly 300–500 Hz.

Quasiequilibrium simulations with realistic equations of state show orbital instability that is dependant on equation of state close to the LIGO-observable band. For example, Gondek-Rosińska et al. [91] estimate a 1100–1460 Hz ISCO for strange stars, due to orbital instability, and 800–1230 Hz for neutron stars, from Roche lobe overflow. Numerical evolutions of quasiequilibrium initial data with polytrope equation of state by Marronetti, Duez, and Shapiro [92] show orbital instability at 15% smaller frequency than the quasiequilibrium-estimated ISCO. As the EOS become stiffer, simulations show a transition from an ISCO-limited orbit to a merger prior to the expected ISCO frequency.

Faber et al. [93], using polytropic EOS, calculate energy spectra from the quasiequilibrium sequences which show a slow fall-off from the point mass spectrum, starting between 500Hz and 1050Hz. Bejger et al. [94] show similar results with realistic EOS.

Given these results of quasiequilibrium simulation, it seems reasonable to expect waveforms to hold equation of state information at frequencies as low as 400–500 Hz.

Work on merger waveforms from binary neutron stars with realistic equation of state has focused only on the last orbit, giving meaningful spectra only for frequencies greater than 1 kilohertz. The waveforms estimated, for example from fully relativistic simulations by Shibata et al. [33] and from conformally flat simulations by Oechslin and Janka [95] show distinctions between different equations of state. Both groups estimate late merger waveform dependence on total mass, mass ratio, spin, and EOS, and find that the frequency spectrum from the merger and post-merger is most sensitive to EOS and total mass.

6.5.1 Post-Newtonian with finite size effects

Orbital energy calculations following [96, 97] show first order tidal corrections to orbital energy overwhelming all PN effects at the high end of LIGO-observable frequencies. These corrections first appear in PN expressions in terms $\sim x^5 k_2 (R/M)^5$, where k_2 is an apsidal constant characterizing the internal structure and $x \sim M/r$ with r the radius of an orbit. They are explicitly fifth post-Newtonian order, however they are also proportional to the fifth power of radius of the star R, so become significant when the two radii are comparable.

The same first-order tidal correction terms are derived by Flanagan and Hinderer

[98], and are used to estimate internal structure measurability of polytropic neutron stars using early inspiral in LIGO-type detectors. They estimate that such observations could constrain radii of $1.4M_{\odot}$ neutron stars to $\lesssim$ 13–15 km depending on the polytropic index.

Hinderer [99] calculates the internal structure corrections k_2, which modify the R-dependence of the post-Newtonian effects for a given mass, using polytropic EOS. For polytropes with similar characteristics as realistic EOS, varying k_2 shifts the effect of radius R in the tidal correction terms by $\sim 10\%$.

Figure 23 : Possible noise spectra of Advanced LIGO in different modes of operation. The three most sensitive noise curves at $\gtrsim 500\,\mathrm{Hz}$ are the NS-NS optimized curve, the Zero Detune high power curve (a broadband configuration), and the narrowband tuned High Freq curve. Figure from [87].

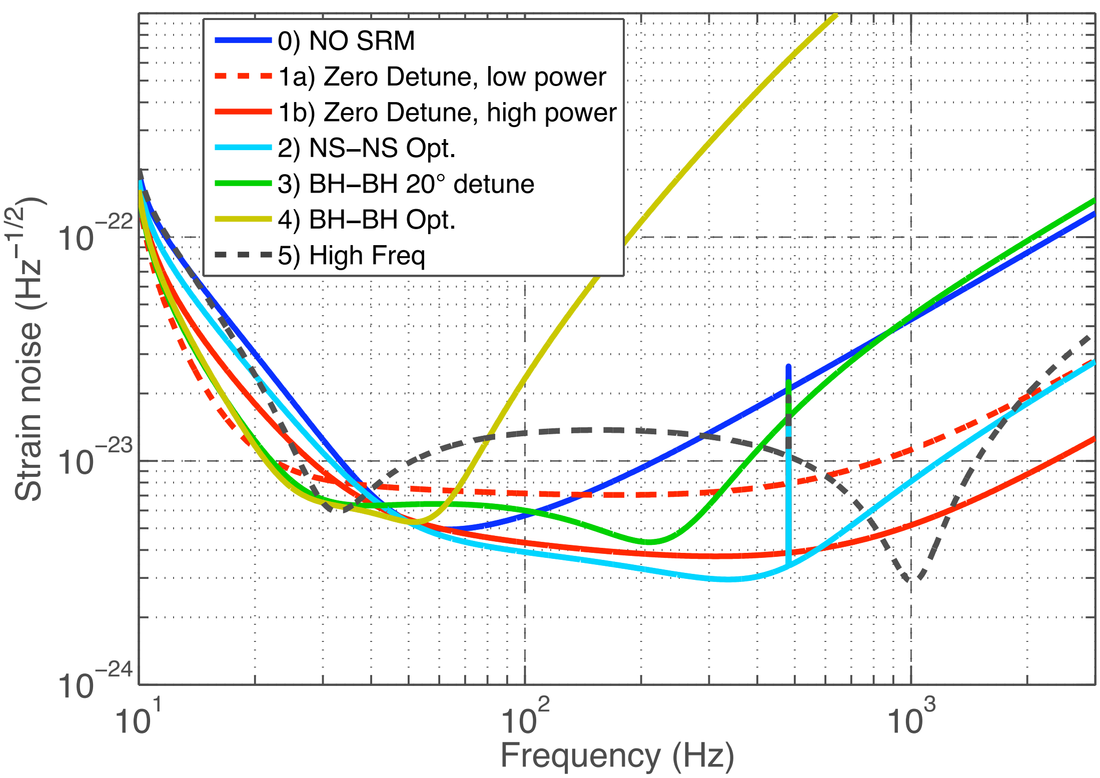

Chapter 7

Constraints from binary inspiral on the equation of state

This chapter reports the results of a first study that uses numerical simulations of binary inspiral to estimate the accuracy with which one can extract parameters of the neutron-star equation of state from gravitational wave observations.

We would like to estimate whether interferometers with the sensitivity of Advanced LIGO can detect the effects of the equation of state on the late inspiral to merger waveforms, and study the potential constraints placed on the EOS parameters from such observations. To do this, we use a set of numerical simulation waveforms produced by varying the equation of state used to model the neutron star matter. These simulations of binary neutron star inspiral and merger, the first to compute several orbits before merger, were provided by Masaru Shibata using initial data produced by Charalampos Markakis and Koji Uryu. The signal analysis focuses on the late inspiral, as the radius of the orbit r approaches the neutron star radius R. The orbital dynamics in this region will depend on the radius and internal structure of the neutron star, which in turn depend on the equation of state.

As Lattimer and Prakash observed, neutron-star radius is closely tied to the pressure at at density one to two times nuclear density, and our results suggest that gravitational wave observations will be able to place stringent constraints on a related equation of state parameter, the p_2 of Chapter 3.

7.1 Parameter variation in numerical simulation

We will assume that equation of state effects on the waveform impact the late inspiral and merger waveform only. For simplicity, we assume that orbital parameters, such as M,η,t_c, and ϕ_c, are determined from the observations of the inspiral waveform, with sufficient accuracy that their measurement uncertainty will not affect the accuracy to which the late inspiral effects determine the EOS parameters.

The initial model EOS are very simple: we vary the core equation of state with an overall pressure shift p_2, specified at the fiducial density $\rho_2 = 5.011872336 \times 10^{14}\,\mathrm{g\,cm^{-3}}$, while holding the adiabatic indices in all regions of the core fixed at $\Gamma = 3$. The crust equation of state modelled by a single polytrope, fitted to tabulated crust EOS, for the region above neutron drip, as the simulations do not resolve densities below roughly $10^{12}\,\mathrm{g\,cm^{-3}}$. The crust polytrope has $\Gamma_0 = 1.35692395$ and $p_0/c^2 = 1.745557593 \times 10^{10}\,\mathrm{g\,cm^{-3}}$ at $\rho_0 = 10^{13}\,\mathrm{g\,cm^{-3}}$.

Figure 24 : Initial choices of EOS for numerical evolution (left) compared to a set of candidate equations of state (right). Candidates are labelled in order of increasing softness: 2H, HB, B, 2B.

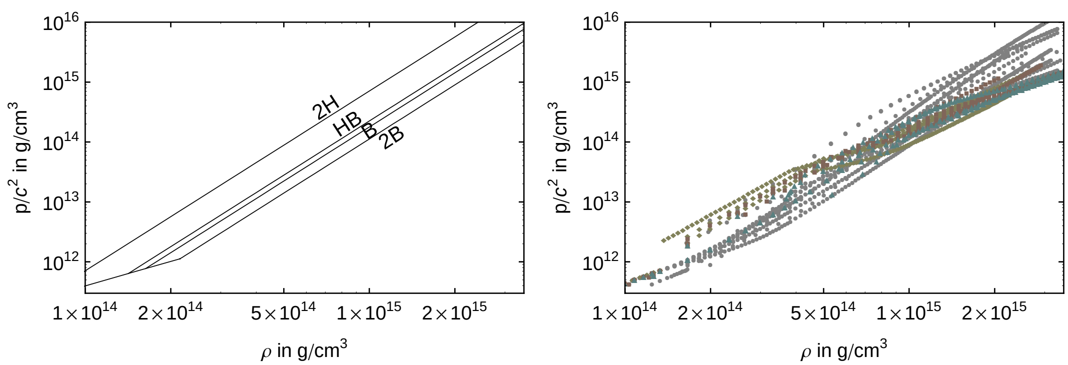

We expect the structure of $\sim 1.4 M_\odot$ neutron stars to depend most strongly on the value of p_2, based on both the empirical formula of Lattimer and Prakash [25] describing radius as a function of pressure at a fiducial density at some $\rho \simeq 2.7$ to $5 \times 10^14\,\mathrm{g\,cm^{-3}}$, and the piecewise polytrope equation of state study described in Chapter 3 showing moment of inertia of $1.388 M_\odot$ neutron stars is largely dependent on p_2.

The first models were chosen with EOS that "bracket" the range of existing candidates, seen in Fig. 24. The models HB with $\log_{10} p_2 = 13.45$, a standard equation of state, H2 with $\log_{10} p_2 = 13.95$, a stiff equation of state; and B2 with $\log_{10} p_2 = 13.15$, a soft equation of state. An additional model, B, with $\log_{10} p_2 = 13.35$ was chosen with a small shift in parameter from HB to better estimate local parameter dependence of the waveform. We measure p_2 in units of $\mathrm{g\,cm^{-3}}$, dividing pressure measured in $\mathrm{erg\,cm^{-3}}$ by c^2.

Table 7 : Properties of initial EOS. These range from the "softest" equation of state at the top, which results in a prompt collapse to a black hole upon merger, to the "hardest" (or "stiffest") at the bottom. Model HB is considered a typical EOS. Radius is that of an isolated TOV star, in Schwartzchild-like coordinates. All candidates have $\Gamma = 3$ in the core.

Model	$\log_{10} p_2 [\mathrm{g\,cm^{-3}}]$	$R\,[\mathrm{km}]$	M/R
2B	13.15	9.7	0.21
B	13.35	10.9	0.18
HB	13.45	11.6	0.17
2H	13.95	15.2	0.13

Although the set of models is explicitly constructed by varying the single parameter p_2, the resulting neutron star models also have systematic variation in the radius R, as seen in Table 7. They can also be considered a one-parameter family of varying R, and the parameter estimation analysis is done for both p_2 and R.

Future work could involve additional models of varying adiabatic indices around a fixed p_2, or varying multiple equation of state parameters to construct models of the same R but different internal structure.

7.2 Numerical Simulation

The method of numerical simulation of binary neutron stars with these EOS follows methods of previous work by Masaru Shibata and collaborators [81, 100, 101].

Initial data is constructed by Koji Uryu and Charalampos Markakis in the conformally flat approximation from these two equations of state. The initial data is constructed by taking two stars which have gravitational mass $1.35 M_\odot$ when far apart, and bringing them together while preserving baryon number. The initial data are irrotational. Quasiequilibrium sequences are used to estimate a initial separation roughly three orbits before merger.

The initial data are evolved using the code of Masaru Shibata. The Einstein equations are solved with a version of the BSSN formulation, using approximately maximal slicing. Hydrodynamics are calculated with a high-resolution shock-capturing scheme. The simulations use the cold equation of state specified in Sec. 7.1, along with a thermal effective adiabatic index Γ_t as described in [102]. The cold approximation is valid for the bulk of the neutron star matter until the merger, where thermal energy can increase from shock heating to up to $\sim 25\%$ of the total energy [81], and determines EOS effects on late inspiral properties.

Gravitational radiation is extracted via a method of splitting the wave-zone metric into a flat background and linear perturbation, and decomposing the latter with tensor spherical harmonics. A gauge invariant Moncrief variable is constructed for each mode. For equal or near-equal mass binary neutron stars the quadrupole (2,2) mode is much larger than other modes, and is the only the (2,2) mode reported for this analysis. The polarization waveforms h_+ and $h_\times$ can then written in terms of the quadrupole modes and the spherical angles to the observer.

7.3 Waveform analysis methods

The waveforms output from the simulation, using the procedure outlined in Sec. 7.2, are the cross and plus amplitudes h_+D/M and $h_\times D/M$ of the quadrupole waveform, as would be measured far along the z axis perpendicular to the plane of rotation, versus the retarded time t. Here M is the sum of the two neutron star masses when they are far apart, $2.7M_\odot$. The strain is specified at discrete values evenly spaced in t.

We construct the complex quantity $h = h_+ - ih_\times$ from this data. The amplitude and phase of this quantity define the instantaneous amplitude $|h|$ and phase $\phi = \arg(h)$ of the numerical waveform. The instantaneous frequency f is then estimated by

$$f = \frac{1}{2\pi}\frac{d\phi}{dt} \simeq \frac{1}{2\pi}\frac{\phi_{i+1} - \phi_i}{t_{i+1} - t_i}. \tag{7.1}$$

The time marking the end of of the inspiral (and onset of merger) is defined by the peak of the waveform amplitude $|h|$. However, the amplitude of the waveforms oscillates over the course of an orbit. A moving average over 0.0005 s segments is used to (roughly) average over the last orbit; the end of the inspiral is defines as a time 0.00025 s after the maximum of the moving average. The resulting merger time t_M is marked by solid lines in the plots to follow.

The numerical data can be shifted in phase and time by adding a time shift τ to the time series points and multiplying the complex h by $e^{i\phi_s}$ to shift the overall wave phase by ϕ_s.

Working in terms of discretized quantities, waveform comparison will sometimes require resampling of one waveform to the time step of another. We use cubic interpolation of the coarser waveform onto a time series with the same time step as the finer waveform. The resolution Δt of the numerical waveforms decreases with increasing stiffness, as the starting frequency (estimated three orbits before merger by quasiequilibrium sequences) is lower and the time for the full simulation is larger.

Windowing of the discrete time series is used to

1. smoothly truncate waveforms to isolate inspiral behaviour,
2. join a matched PN inspiral onto the numerical waveform, and
3. decrease side-band effects in the discrete Fourier transform (DFT) from the sharp start and stop of a finite time series.

One-sided Hann-like windows are used to smoothly turn on

$$w(n) = \frac{1}{2}\left[1 - \cos\left(\frac{\pi n}{N-1}\right)\right] \tag{7.2}$$

or turn off

$$w(n) = \frac{1}{2}\left[1 + \cos\left(\frac{\pi n}{N-1}\right)\right] \tag{7.3}$$

a signal over a range of N points (or over a time $N\,\Delta t$).

A butterfly of windows is used to join PN fit to numerical data by turning on the numerical waveform as the PN is turned off, such that the sum of the two window functions is 1 over the whole range. The choice of range is discussed in Sec. 7.4.

7.4 Post-Newtonian matching

The numerical waveforms are started at different frequencies. To align them for comparison, they are each matched in the early inspiral region to the same post-Newtonian point particle, or PP, waveform.

The particular post-Newtonian waveform chosen follows the Taylor T4 of [77], where it was found that this particular version had excellent agreement in both amplitude and phase with the long-term numerical binary black hole inspiral. It is thus taken to be representative of the full GR behaviour of the (point-particle-like) binary black hole inspiral. The post-Newtonian waveform agrees with binary black hole inspiral up to the last cycle before merger; we will show that the binary neutron star waveforms depart from the point-particle evolution 3–7 cycles before the point particle merger.

To match the numerical data, both a time shift and phase shift must be specified. The complex numerical quadrupole waveform is convolved with the complex post-Newtonian quadrupole waveform, $g = h_+^{PP} - i h_\times^{PP}$.

$$
\begin{aligned}
z(\tau) &= \int_{T_0}^{T_f} h(t) g^*(t-\tau) dt &(7.4)\\
&= \int_{T_0}^{T_f} \left[h_+(t) - i h_\times(t)\right]\left[g_+(t-\tau) + i g_\times(t-\tau)\right] dt &(7.5)\\
&= \int_{T_0}^{T_f} \left[h_+(t) g_+(t-\tau) + h_\times(t) g_\times(t-\tau)\right] dt \\
&\quad + i \int_{T_0}^{T_f} \left[h_+(t) g_\times(t-\tau) - h_\times(t) g_+(t-\tau)\right] dt &(7.6)
\end{aligned}
$$

Here the integrals are taken over a matching region $T_0 < t < T_f$ before the end of the numerical inspiral.

This quantity is similar to the complex matched filter output of the FINDCHIRP algorithm [85]. The real part of $z(\tau)$ corresponds to the correlation of the two waveforms as a function of the time shift τ. The absolute value $|z(\tau)|$ is the correlation maximized over a constant overall phase shift, and the argument is the overall phase shift required to so maximize.

The match time τ maximizing PP and numerical correlations is sensitive to the portion of the numerical waveform matched, T_0–T_f. Some truncation of the numerical waveform is required to eliminate residual effects of initial data, and one would also like to truncate the waveform at some point before the peak amplitude, at the end of the region without significant finite size effects.

As the region without significant finite size effects is itself determined by comparison with point particle post-Newtonian waveforms, this procedure is somewhat self-referential. The variation in the best time shift can be calculated as the match region is varied, truncating at various times $T_f = t_M - T$ before the end of numerical inspiral t_M.

Figure 25 : Best time shift τ between numerical waveform and post-Newtonian waveform, matching to a segment $T_0 < t < T_f = t_M - T$ of the numerical waveform truncated starting a time T before the end of numerical inspiral t_M.

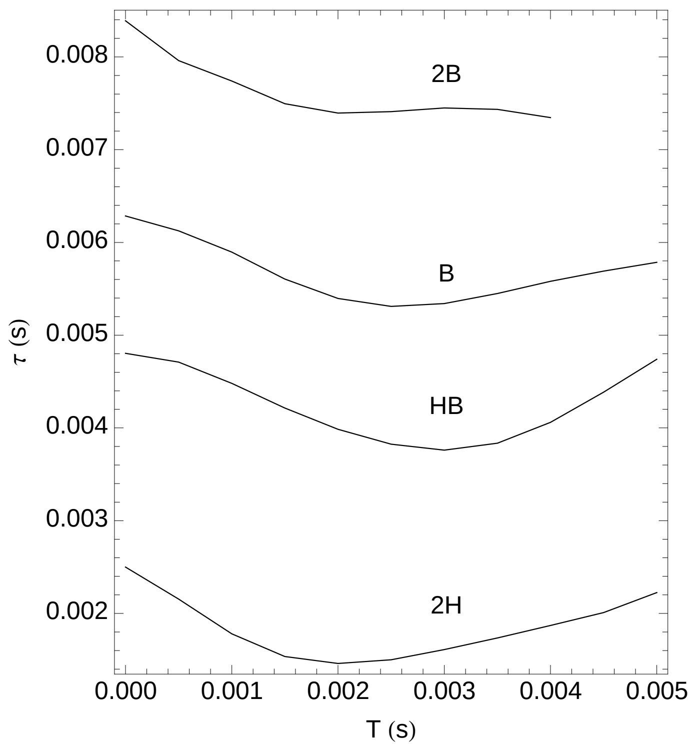

Fig. 25 shows that truncating the numerical waveform just at the end of inspiral leads to a larger time shift τ: the waveform is matched to point-particle post-Newtonian closer to the point particle merger. As late-inspiral regions are windowed out, and T increases, the matching time shift τ is smaller. Ideally, there would be convergence of the time shift as finite-size effects are eliminated from the numerical waveform. As can be seen in Fig. 25, this does not happen, i.e., the curves do not level off as T increases. The reason is that for large T few waveform cycles are available for matching after the early-stage inaccuracies are windowed out, degrading the ability to estimate the matching PP coalescence time.

Varying these choices can change the best match τ by up to $\simeq 0.001$ s. By comparison, one waveform cycle takes between 0.0005 and 0.002 s in the inspiral region, so this will be a significant source of uncertainty in SNR estimates. Longer duration simulations are required to more accurately choose τ. Of course, in a real data analysis application, the PP coalescence time will be found to accuracies of better than ~ 1 ms even for relatively weak detections ($\rho \sim 10$) [83].

We choose to take a larger matching region truncated to between 0.0015 s after the start of the waveform and 0.001 s before merger. Varying these choices can change the best match τ by up to $\simeq 0.001$ s. By comparison, one waveform cycle takes between 0.0005 and 0.002 s in the inspiral region, so this will be a significant source of uncertainty in SNR estimates. Longer duration simulations are required to more accurately choose τ. Of course, in a real data analysis application, the PP coalescence time will be found to accuracies of better than ~ 1 ms even for relatively weak detections ($\rho \sim 10$) [83].

Unlike the case of matching binary black hole simulations to point particle post-Newtonian, the binary neutron star simulations show departure from point particle many cycles before the post-Newtonian merger time. Fig. 26 shows the four waveforms. As the stiffness of the equation of state, and thus the radius of the neutron stars, increases, the end of inspiral for the binary neutron stars is shifted away from the end of inspiral for point particle post-Newtonian.

This can also be seen by plotting the instantaneous frequency of the numerical simulation waveform with the same time shifts, as in Fig. 27. Fig. 27 also shows more clearly the difference in the post-merger oscillation frequencies of the hyper-massive remnants, when present: the larger neutron star produced by the stiff EOS 2H has a lower frequency than that from the medium EOS HB.

7.5 Discrete Fourier transform and comparison with Advanced LIGO noise

Given h_+ or $h_\times$, one can construct the Fourier transform $\tilde{h}_+$ or $\tilde{h}_\times$. Both polarizations yield the same DFT spectrum $|\tilde{h}|$, with phase shifted by $\pi/2$, if one neglects discretization, windowing, and numerical effects (including eccentricity). The spectrum $|\tilde{h}|$ is independent of phase and time shifts of the waveform.

Figure 26 : Plus (left) and cross (right) amplitudes of numerical waveforms, scaled by D/M, and aligned in time and phase to the same point-particle post-Newtonian inspiral (dashed line), using the method described in Sec. 7.4. The two dashed vertical bars indicate the limits of the waveform used for matching; the last vertical bar indicates the peak amplitude of the numerical waveform. The top three simulations, 2H, HB, and B, show the start of post-merger oscillations from a hypermassive NS remnant in the simulation. The bottom simulation 2B shows quasinormal ringdown from a prompt collapse to a black hole following merger.

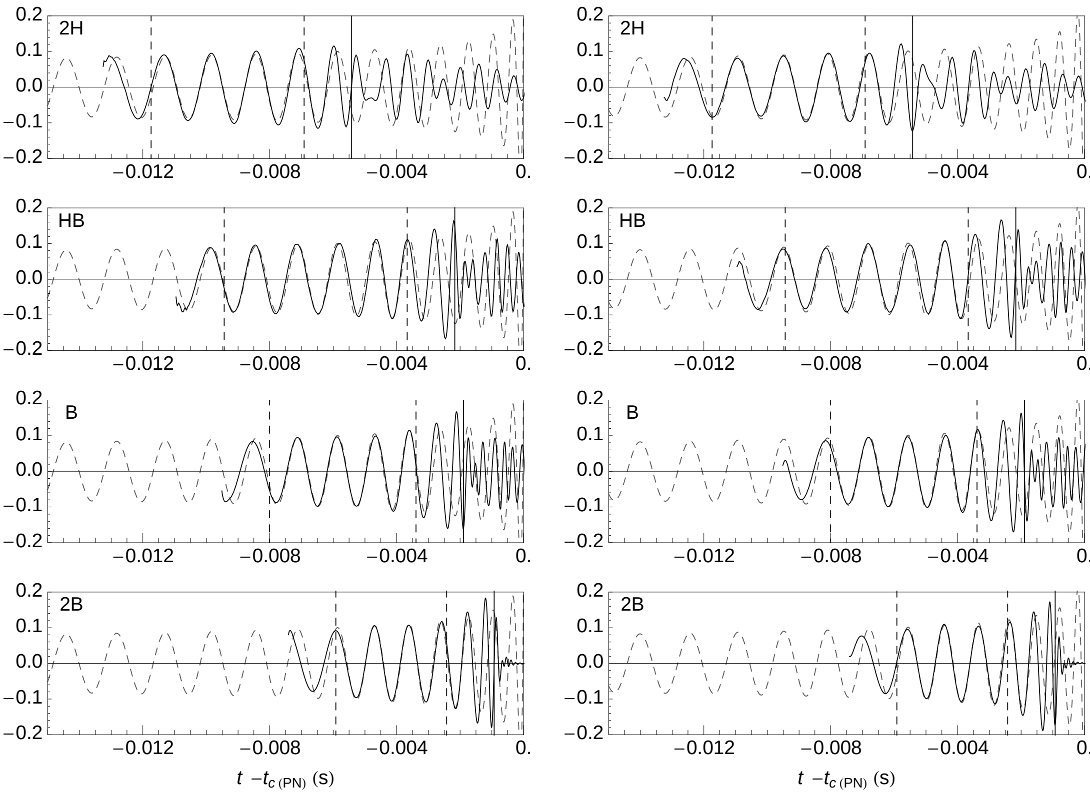

The stationary phase approximation of Sec. 6.1.3 is valid for the post-Newtonian waveform in the frequency ranges considered, so it is used to generate the point particle spectrum.

To compare to detector noise, the spectra are converted into equivalent strains in a one-Hz bandwidth, based on a given effective distance D to the system. Fig. 28 shows the result for the numerical simulations only, scaled for a system at 100 Mpc, compared to the burst-optimized Advanced LIGO equivalent strain noise. The quantity plotted is $\sqrt{f|\tilde{h}(f)|^2}$, rescaling from the previously plotted numerical output $h(t)D/M$ using $M = 2.7M_\odot$ and $D = 100\,\mathrm{Mpc}$. Fig. 29 compares similar 100 Mpc spectra from

Figure 27 : Instantaneous frequency of numerical simulation, averaged over 0.001 s, as a function of time. Stars mark the time of peak numerical waveform amplitude. Results from each numerical simulation are shifted in time to match a common point particle early inspiral; this is the only degree of freedom available to improve the agreement in frequency. The waveforms of 2H and HB show a roughly constant frequency post-merger from a hyper-massive neutron star bar mode; the simulation of B was halted shortly after the formation of such a hyper-massive object. Waveform 2B collapses promptly to a black hole.

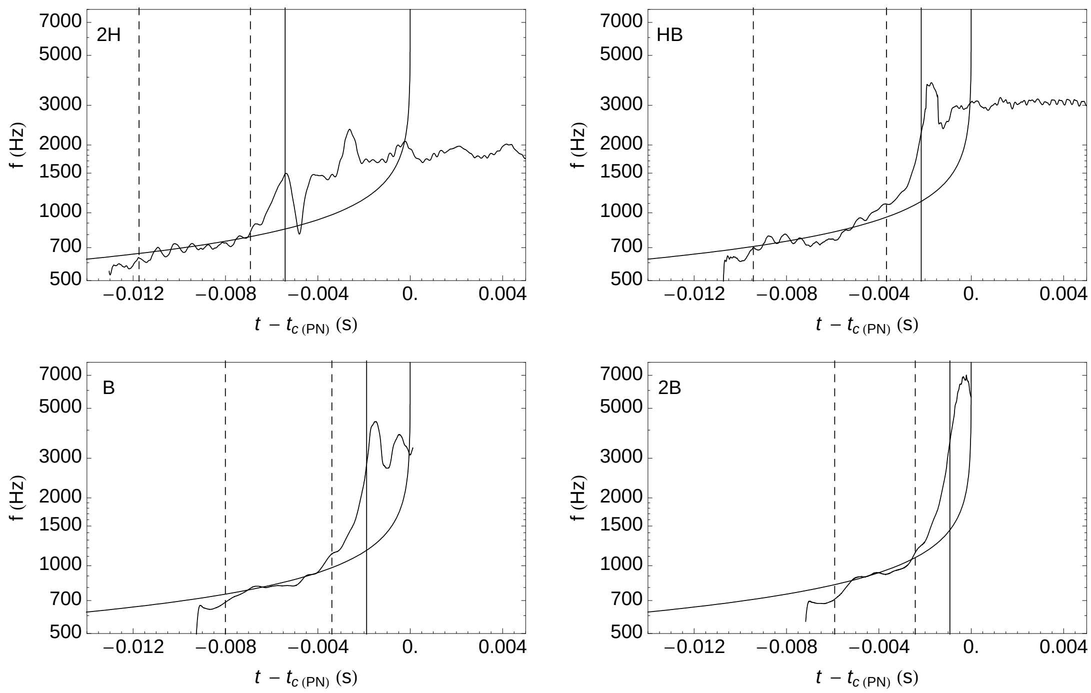

waveforms truncated after inspiral.

The full spectra of models 2H, HB, and B, seen in Fig. 28, show peaks at post-merger oscillation frequencies; those of B are weaker as the waveform is truncated shortly after the formation of the hyper-massive remnant. Waveforms of 2H and HB are also truncated while the post-merger oscillation is ongoing; if the simulations were allowed to continue, these peaks would presumably grow further. The simulation of 2B, in contrast, collapses to a black hole and has only a short lived (and relatively small-amplitude) quasinormal mode ringdown post merger.

Although such post-merger oscillations are an interesting source of potentially measurable strains, the dependence on the cold equation of state is less straight-forward as temperature effects become significant during the the merger. We focus

Figure 28 : DFT of numerical waveforms windowed by 0.001 s at edges, at an effective distance $D = 100\,\mathrm{Mpc}$, compared to the noise spectrum for Advanced LIGO in a broadband configuration optimized for burst detection. Curves are shown, for each numerical simulation, from both the + and × polarizations.

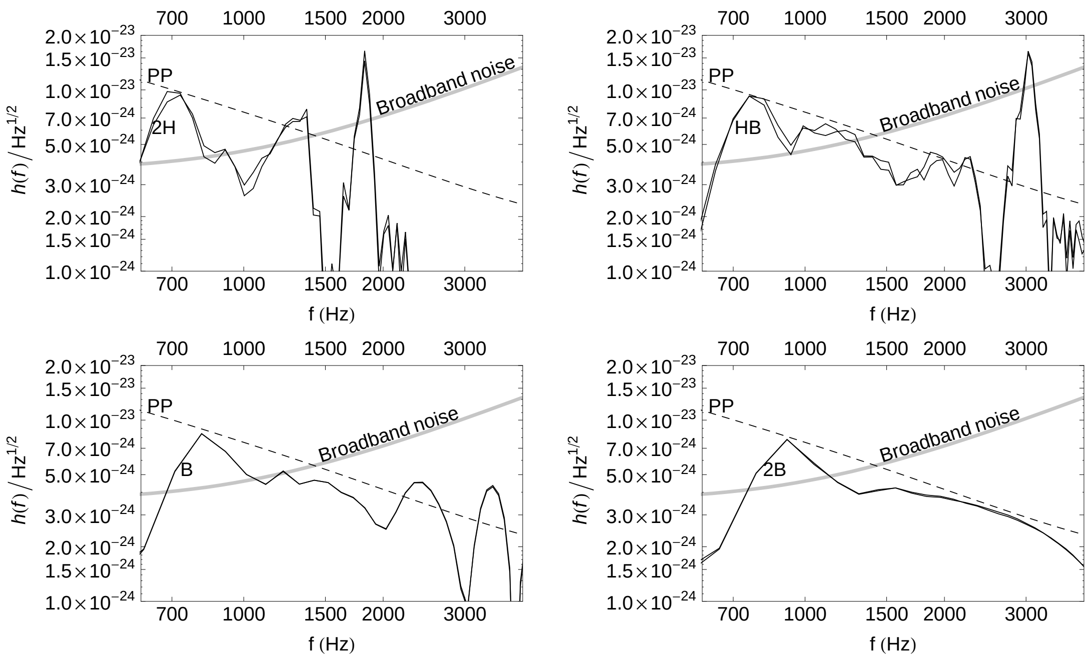

Figure 29 : Left panel is DFT of numerical waveforms truncated after peak waveform amplitude to show spectrum of inspiral only. Right panel shows DFT of same waveforms smoothly merged in the time domain with the point particle PN waveforms shown in Fig. 26.. The distance $D = 100\,\mathrm{Mpc}$. Curves are shown, for each numerical simulation, from both the + and × polarizations. The lumps in the spectrum, for example around 1100Hz for HB, may be due to eccentricity in the numerical waveform.

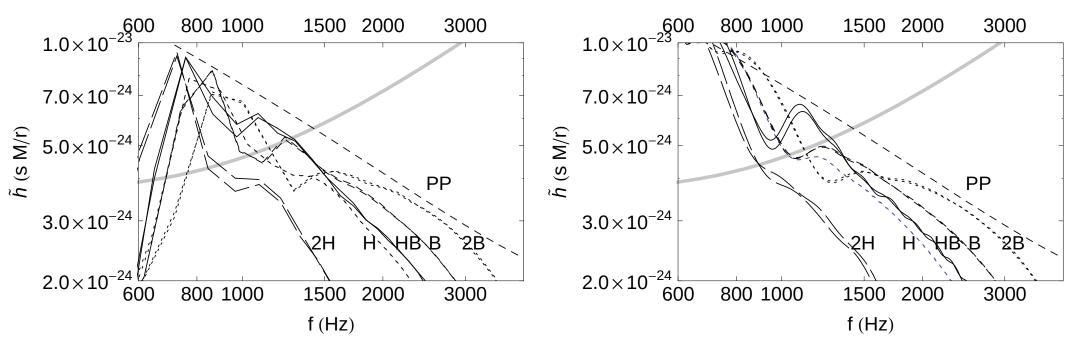

instead on the spectra from the waveforms during the inspiral region only. Fig. 29 shows how these change as the equation of state is varied.

Note that time-frequency plots like the ones shown Fig. 27 show that numerical waveforms match the PP waveform at instantaneous frequencies of up to roughly 750–1150 Hz, depending on the EOS. The disagreement in the spectra from the PP stationary-phase approximation waveform at frequencies below this is primarily due to the finite starting time of the numerical waveforms.

7.6 Detectability

In general signal detection, one finds the best fit parameters of the system including the best fit phase and time shifts for a given signal. In our case, we assume that the two masses, the distance, as well as the phase and time shift have been fixed by a strong inspiral measurement in the frequency range 10 to 500 Hz, where the NS-NS inspiral is assumed to be well modelled by a post-Newtonian point particle binary.

We then attempt to measure a single parameter, either p_2 or R, which generates a one-dimensional family when all other parameters are fixed. This family is discretely sampled by the waveforms from the numerical simulations above.

After the numerical waveforms have been matched to the same post-Newtonian point-particle inspiral, the signals will be aligned in time and phase. We can then then compare the resulting waveforms to each other using different Advanced LIGO noise spectra. A stationary phase approximation can be used to calculate the Fourier transform of the signals at low frequencies.

We first consider the "distinguishability" of a pair of waveforms (h_a, h_b) with a given noise spectrum as estimated by calculating the SNR of the difference between them, $\rho_{\text{diff}} = \sqrt{\langle h_a - h_b | h_a - h_b \rangle}$. We consider two waveforms distinguishable in a given noise spectrum if $\rho_{\text{diff}} > 1$ using the inner product defined with that spectrum.

The result is given in Tables 8-10 for noise curve tuning optimized for 1.4 Solar Mass NS-NS inspiral ("Standard"), bursts ("Broadband"), and pulsars at 1150Hz ("Narrowband"), at a reference effective distance of 100 Mpc. For h_a and h_b as measured, the signal to noise ratio will be proportional to $1/D$.

The difference between waveforms due to finite size effects is not detectable in the NS-NS detection optimized configuration of Advanced LIGO for ~ 100 Mpc effective

Table 8 : ρ_{diff} in standard (NS-NS detection optimized) noise $\times\,(100\mathrm{Mpc}/D_{\mathrm{eff}})$

	PP	2B	B	HB	H
PP	0	0.30	0.47	0.42	0.61
2B		0	0.42	0.33	0.55
B			0	0.23	0.52
HB				0	0.50
2H					0

Table 9 : ρ_{diff} in broadband (burst-optimized) noise $\times\,(100\mathrm{Mpc}/D_{\mathrm{eff}})$

	PP	2B	B	HB	H
PP	0	1.77	2.33	2.21	2.62
2B		0	1.97	1.81	2.24
B			0	0.89	2.06
HB				0	2.05
2H					0

Table 10 : ρ_{diff} in narrowband 1150 Hz noise $\times\,(100\mathrm{Mpc}/D_{\mathrm{eff}})$

	PP	2B	B	HB	H
PP	0	0.78	2.75	1.99	1.91
2B		0	2.08	1.30	1.41
B			0	0.89	2.24
HB				0	1.68
2H					0

distances. However, in both narrowband and broadband they are. Note that this implies that even if the details of the NS-NS late inspiral signal are not known, the difference between it and a point particle waveform should be measurable. The quantity ρ_{diff} between a NS-NS waveform and a point particle waveform may be useful in itself to constrain possible equations of state without reference to waveform details.

To give a first estimate the accuracy of parameter estimation, we require an estimate of $\partial h/\partial p_2$ and $\partial h/\partial R$ from the sampled waveforms. We use

$$\left.\frac{\partial h}{\partial p_2}\right|_{p_2=(p_{2,a}+p_{2,b})/2} \simeq \frac{h(p_{2,a}) - h(p_{2,b})}{p_{2,a} - p_{2,b}} \tag{7.7}$$

and then, for our one-parameter family and neglecting correlations with other parameters, we have to first order

$$\overline{(\delta p)^2} \simeq\simeq \frac{p_{2,a} - p_{2,b}}{\left\langle h(p_{2,a}) - h(p_{2,b}) \middle| h(p_{2,a}) - h(p_{2,b}) \right\rangle}. \tag{7.8}$$

Similar equations hold for the estimation of R.

Using adjacent pairs of models to estimate waveform dependence at an average parameter value, we then find estimates of radius measurability as shown in Table 11 and p_2 measurability as shown in Table 12 for various noise configurations.

Table 11 : Estimate of measurement error δR for given R in different Advanced LIGO configurations, using adjacent models 2B-B (9.7 km - 10.9 km), B-HB (10.9 km - 11.6 km) , and HB-2H (11.6 km - 15.2 km).

	Broadband	1150 Hz
$\overline{R} = 10.3$	± 0.61 km	± 0.57 km
$\overline{R} = 11.25$	± 0.78 km	± 0.78 km
$\overline{R} = 13.4$	± 1.75 km	± 2.13 km

Table 12 : Estimate of $\delta \log_{10}(p_2)$ for given $\log_{10}(p_2)$ in different Advanced LIGO configurations, using adjacent models 2B-B (13.15 - 13.35), B-HB (13.35 - 13.45), and HB-2H (13.45 - 13.94). The parameter p_2 measures pressure/c^2 in g/cm^3, at a fiducial density of $\rho_2 \simeq 5 \times 10^{14}$ g/cm^3.

	Broadband	1150 Hz
$\overline{\log_{10}(p_2)} = 13.25$	± 0.10	± 0.10
$\overline{\log_{10}(p_2)} = 13.4$	± 0.11	± 0.11
$\overline{\log_{10}(p_2)} = 13.7$	± 0.24	± 0.30

These results are first estimates of the accuracy with which the EOS might be constrained by gravitational wave estimates; they do not take into account multiple detectors or observations nor parameter correlations. A more accurate estimation of EOS parameter measurability will require more detailed analysis, with a larger set of inspiral simulations sampling a broader region of parameter space, e.g. with mass ratios departing from 1, and with several more orbits prior to merger.

Conclusions

Part I was aimed at the following question: Can we find a systematic way to characterize the neutron star equation of state by a small number of parameters that are independent of the particular microphysical model, such that astrophysical observations can be used to limit the values of these parameters?

My work shows that a diverse array of EOS candidates can be well-modelled above nuclear density by a few polytropic regions of constant adiabatic index. Equations of state with exotic matter can require up to three regions, requiring six parameters. However, we can reduce the number of parameters by fixing the boundary density between polytropic regions, without reference to any individual equation of state. Unexpectedly, the optimal choices for fitting the universe of candidates are robustly picked out.

The result is a tractable four-parameter equation of state. It matches each of 31 tabled equations of state to better than 10% accuracy, including examples incorporating the appearance of hyperons, kaons, and quark matter. This allows us to use observations to constrain a parameter space, rather than individually allowing or ruling out an ever-changing set of proposed candidates.

Furthermore, the parameterization allows construction of systematically varying EOS to explore effects on the physics of neutron stars in numerical simulations. The effect of an overall core EOS pressure shift, our parameter p_2, on the inspiral of neutron stars was explored in Chapter 7. The equation of state parameters can also, for example, be varied to create a set of neutron stars with the same mass and radius but different internal structure.

❋

Part II was aimed at the following question: Can a full helical symmetry assumption be used to construct convergent numerical solutions for quasiequilibrium neutron stars which go beyond conformal flatness?

Full helical symmetry with half-ingoing half-outgoing radiation only converges when matched in the wave zone to a waveless solution. The toy model work showed that the convergence of iterative solutions to helically symmetric wave equations was critically dependent on the sign of their nonlinear terms. One choice of sign gives robust convergence, while for the other, convergence sets an upper limit on the coefficient of the nonlinear terms. This suggests that the lack of convergence for the helical code is intractable, given the fixed sign of the nonlinear terms in the Einstein equations.

However, the agreement of the helically symmetric solution with the fully waveless solution in the near zone validates the assumption that more accurate initial data is insensitive to the details of the wave region. This implies that the waveless and helical formulations can be used interchangeably to create quasiequilibrium sequences with improved accuracy. Waveless initial data also allows the addition of a nonzero radial velocity, minimizing orbital eccentricity in full numerical simulations.

❃

Finally, Part III was aimed at following question: Will the effects of the neutron star equation of state be visible with Advanced LIGO, and, if so, how accurately might an observation of a binary neutron star inspiral in Advanced LIGO constrain equation of state properties?

The results of numerical simulation show that the tidal disruption of finite-size neutron stars leads to departure from the point-particle waveform at frequencies as low as 700 Hz, yielding detectable differences for waveforms from neutron stars as far away as 200 Mpc. This translates to measurements of neutron star radius, ignoring internal structure corrections, to roughly $\pm 1\,\mathrm{km}\,(100\ \mathrm{Mpc}/D_{\mathrm{eff}})$, where D_{eff} is the effective distance to the observed neutron star binary.

❃

This thesis has touched on several areas of active research in relativistic neutron star astrophysics. The combination of many observational tools—such as electromagnetic wave astronomy, gravitational wave astronomy, and heavy ion experiments—with an arsenal of analytic, approximate, and numerical methods in many areas of physics, is required to finally nail down the composition and equation of state of cold dense matter, and the properties of stars after they die.

Appendix A

Equation of state tables

J. Lattimer and M. Alford generously provided EOS tables from [25] and [49]. Other tables are from from the LORENE C++ library (`http://www.lorene.obspm.fr`).

AV18 Via Lattimer, AP1 in[25]; a variational EOS with np composition. Akmal et al. [35] use the Argonne two-nucleon interaction AV18. The model valid in liquid core only, and appended onto a separate crust table. See akmalpr for general discussion.

AV18D Via Lattimer, AP2 in[25]; a variational EOS with np composition. Similar to AV18 [35], with relativistic boost corrections.

AV18U Via Lattimer, AP3 in[25]; a variational EOS with np composition. Similar to AV18 [35], with the Urbana model of the three-nucleon interaction.

AV18UD Via Lattimer, AP4 in[25]; a variational EOS with np composition. Similar to AV18 [35], with both the relativistic boost corrections and the three-nucleon interaction. This EOS is also referred to in the literature as APR.

AKMALPR Via LORENE; a variational EOS with np composition. Another version of AV18UD, from Akmal et al. [35], but with the LORENE style SLY4 crust.

Haensel [103] calculates: $M_{max} = 2.21 M_{\odot}$, $R = 10.0\,\mathrm{km}$, $n_c = 1.15\,\mathrm{fm}^{-3}$, $\epsilon_c = 2.73 \times 10^{15}\,\mathrm{g\,cm}^{-3}$.

All AV18-based equations of state use variational chain summation methods using the Argonne v_{18} model of two-body nuclear interactions, which is fit to nucleon-nucleon scattering data at energies below 350 MeV. The Urbana Model IX, (UIX) estimates the effect of three-nucleon interactions, and the δv_b (DVB) is a relativistic boost correction. A nonrelativistic Hamiltonian is calculated from kinetic energies, AV18 interactions, and UIX interactions.

Configurations above roughly $2.1 M_\odot$, $\epsilon_c > 1.73 \times 10^{15}$g/cm^3 have $v_{sound} > c$[6].

BBB2 Via LORENE; a DBHF EOS with np composition. Baldo et al. [38] calculate the EOS using Brueckner-Bethe-Goldstone many-body theory with explicit three-body forces: uses the Argonne v_{18} two-body force and the Urbana Model IX three-body force. The crust is SLY4, matched (at $n = 0.0957, \epsilon = 1.60E14$).

Haensel [103] calculates: $M_{max} = 1.92 M_\odot$, $R = 9.49\,\mathrm{km}$, $n_c = 1.35\,\mathrm{fm}^{-3}$, $\epsilon_c = 3.20 \times 10^{15}\,\mathrm{g\,cm}^{-3}$.

BPAL12 Via LORENE; a DBHF EOS with np composition. EOS supplied by Bombaci in August 1999, referencing Zuo, Bombaci, and Lombardo [39], where the EOS is calculated from an extended Brueckner-Hartree-Fock approximation, using the Argonne v_14 two-body interaction. Matched to SLY4 crust at $n = 0.095, \epsilon = 1.60E14$.

Haensel [103] calculates: $M_{max} = 1.46 M_\odot$, $R = 9.00\,\mathrm{km}$, $n_c = 1.76\,\mathrm{fm}^{-3}$, $\epsilon_c = 3.94 \times 10^{15}\,\mathrm{g\,cm}^{-3}$.

ENGVIK Via Lattimer, ENG in [25]; a DBHF EOS with np composition. Engvik et al. 1996 [40, 104] construct this EOS using Dirac-Brueckner-Hartree-Fock many-body theory, and the table is made causal above $n = 0.7$ through unspecified means.

FPS Via LORENE; a variational EOS with np composition. EOS supplied by Stergioulas in 1998 via Haensel. The EOS follows BPS below neutron drip, then mimics FPS using a Skyrme-type energy density fitted to the Friedman and Panharipande [36] (FP in [25]) equation of state. This method is described by Lorenz, Ravenhall, and Pethick[105]. Crust bottom at $n = 0.0957, \epsilon = 1.60E14$.

Haensel [103] calculates: $M_{max} = 1.79 M_\odot$, $R = 9.66\,\mathrm{km}$, $n_c = 1.37\,\mathrm{fm}^{-3}$, $\epsilon_c = 3.09 \times 10^{15}\,\mathrm{g\,cm}^{-3}$.

MPA1 Via Lattimer, MPA1 in [25]; a DBHF EOS with np composition. Müther, Prakash, and Ainsworth [41] extend the relativistic Brueckner-Hartree-Fock approach for nuclear matter to dense neutron matter, including contributions from the exchange of π and ϱ mesons and the dependence upon neutron-proton asymmetry.

MS00 Via Lattimer, MS1 in [25]; a field theoretical EOS with np composition. Müller and Serot [42] calculated with relativistic mean field theory. This table uses $\xi = 0, \zeta = 0$, where ξ and ζ are parameters determining the strength of nonlinear vector and isovector interaction (σ, ω, and ϱ mesons).

MS1506 Via Lattimer, MS2 in [25]; a field theoretical EOS with np composition. Similar to MS00, from Müller and Serot [42], but with $\xi = 1.5, \zeta = 0.06$

MS2 Via Lattimer; a field theoretical EOS with np composition. Similar to MS00, from Müller and Serot [42] with $\xi = 0, \zeta = 0$ and $E_{\text{sym}} = 25MeV$, a variant of MS1.

PAL2 Via Lattimer; a schematic potential EOS with np composition. From Prakash, Ainsworth and Lattimer [34], using a parameterization of $E(n)$ in terms of symmetry energy at saturation density, density dependence of symmetry energy, and bulk nuclear matter incompressibility K. A soft version, possibly PAL6 in [25].

PRAKDAT Via Lattimer; a field theoretical EOS with np composition. Glendenning and Moskowski [43] calculate a relativistic mean field theory EOS, suppressing hyperons.

PS Via Lattimer, PS in [25]; an effective potential EOS with $n\pi^0$ composition. Pandharipande and Smith [44] calculate an EOS based on neutrons and a pion condensate, with no charged particles.

SLY4 Via LORENE, an effective potential EOS with np composition. SLY4, from Douchin and Haensel [6], is a unified crust-core equation of state, calculated using an effective S(kyrme-)Ly(on) nuclear interaction for both crust (in nucleus bulk energy) and core (in nucleon-nucleon energy).

Haensel [103] calculates: $M_{max} = 2.05 M_\odot$, $R = 9.99\,\mathrm{km}$, $n_c = 1.21\,\mathrm{fm}^{-3}$, $\epsilon_c = 2.86 \times 10^{15}\,\mathrm{g\,cm}^{-3}$.

The outer crust EOS is calculated assuming T=0 and ground state composition with a Compressible Liquid Drop Model (CLDM) for nuclei and nuclear structures. Similar to the CLDM ignores shell effects and pairing within the nuclei, it is replaced for $\rho < 4.3 \times 10^{11}\mathrm{gcm}^{-}3$ by the crust EOS of Haensel & Pichon [106].

This EOS leads to minimum mass $0.094 M_\odot$, maximum mass $2.05 M_\odot$ ($2.42 M_\odot$ with rigid rotation), and maximum rotation at $P_{min} = 0.55ms$, neglecting the envelope $\rho < 10^6 gcm^{-3}$ of mass $\sim 10^{-10} M_\odot$. Stars of $1.4 M_\odot$ have central energy density roughly $10^{15}\mathrm{g/cm}^3$. Beneath the central density of maximum mass stars, SLY4 has $v_{sound} < c$. Near $1.4 M_\odot$, the radius is slightly below 12km. Surface redshift, binding energy, moment of inertia and crustal moment of inertia, other rotational effects, apparent radii, are also discussed in [6].

A SLY4-based crust is used in all EOS except fps.

WFF1 Via Lattimer, WFF1 in [25]; a variational EOS with *np* composition. This EOS uses the Argonne $v14$ (an earlier version of AV18) nucleon-nucleon interaction plus the Urbana VII three nucleon interaction model, calculated by Wiringa, Fiks, and Fabrocini [37] using variational chain summation. The maximum mass is $2.19 M_\odot$. There is a kink in the total energy of this model that is interpreted as evidence for a phase transition to a neutral pion condensate.

WFF2 Via Lattimer, WFF2 in [25]; a variational EOS with *np* composition. From Wiringa, Fiks, and Fabrocini, as WFF1 [37]. The maximum mass of this variant is $2.13 M_\odot$.

WFF3 Via Lattimer, WFF1 in [25]; a variational EOS with *np* composition. From Wiringa, Fiks, and Fabrocini, similar to WFF1. [37].

BALBN1H1 Via LORENE; an effective potential EOS with *npH* composition. EOS supplied by Balberg in January 2000, from Balberg and Gal [46]. Uses a local effective potential, including nucleons and hyperons (all eight species of (s=1/2) baryons). Table matches EOS in Fig. 7 labelled $np\Lambda\Xi + \Sigma$. Matched to SLY4 crust at $n = 0.0957, \epsilon = 1.60E14$. Haensel [103] calculates: $M_{max} = 1.64 M_\odot$, $R = 9.38\,\mathrm{km}$, $n_c = 1.60\,\mathrm{fm}^{-3}$, $\epsilon_c = 3.72 \times 10^{15}\,\mathrm{g\,cm}^{-3}$.

GLENDENH Via LORENE; a field theoretical EOS with npH composition. Glendenning [47] case 3. EOS incorporating both nucleons and hyperons, calculated with mean field theory.

GM1NPH–GM3NPH Via Lattimer, GM1–GM3 in [25]; a field theoretical EOS with npH composition. From Glendenning and Moszkowski [43].

PCL_NPHQ Via Lattimer, PCL2 in [25]; a field theoretical EOS with $npHQ$ composition. From Prakash, Cooke, and Lattimer [48].

SCHAF1–2 Via Lattimer, GS1–GS2 in [25]; a field theoretical EOS with npK composition. From Glendenning and Schaffner-Bielich[45].

ALF* Via Alford, in [107]. A generic parameterization of a quark matter equation of state is generalized to a charged phase, as is nuclear matter based on the equation of state from Akmal, Pandharipande, and Ravenhall. Mixed phases are then allowed in intermediate density regions based on energetics. ALFC incorporates QCD corrections to the quark chemical potential.

Appendix B

Accuracy of best-fit parameterizations

Table 13: Values for observables calculated using tabulated equations of state as well as the corresponding parameterized equation of state using the best fit parameters. $M_{\rm max}$ is the maximum nonrotating mass configuration.$z_{\rm max}$ is the corresponding maximum gravitational redshift. $f_{\rm max}$ is the maximum rotation frequency as calculated using the rotating neutron-star code rns. $R_{1.4}$ is the radius of a 1.4 $M_\odot$ star in units of km. $I_{1.338}$ is the moment of inertia for a 1.338 $M_\odot$ star in units of 10^{45} g cm^2. $v_{s,\rm max}$ is the maximum adiabatic speed of sound below the central density of the maximum mass neutron star. The difference in calculated values for each observable when using the tabulated equation of state (O_{tab}) versus the best fit parameterized equation of state (O_{fit}) is calculated with $(O_{fit}/O_{tab} - 1)100\%$.

EOS	$M_{\rm max}$	$z_{\rm max}$	$f_{\rm max}$	$R_{1.4}$	$I_{1.338}$	$v_{s,\rm max}$
AV18	1.683	0.581	1970	9.361	0.908	0.924
fit	1.656	0.597	2043	9.188	0.884	1.016

Continued on next page...

EOS	$M_{\max}$	$z_{\max}$	$f_{\max}$	$R_{1.4}$	$I_{1.338}$	$v_{s,\max}$
%	-1.60	2.79	3.68	-1.85	-2.57	9.94
AV18D	1.808	0.605	1890	10.179	1.024	1.032
fit	1.781	0.607	1923	10.019	1.000	1.0359
%	-1.50	0.33	1.76	-1.57	-2.34	0.42
AV18U	2.390	0.704	1585	12.094	1.375	1.134
fit	2.366	0.708	1607	11.978	1.353	1.165
%	-1.00	0.57	1.39	-0.96	-1.59	2.72
AV18UD	2.213	0.696	1699	11.428	1.243	1.160
fit	2.189	0.697	1720	11.326	1.226	1.177
%	-1.08	0.22	1.24	-0.90	-1.36	1.45
BPAL12	1.452	0.382	1616	10.024	0.974	0.708
fit	1.449	0.381	1614	10.091	0.976	0.716
%	-0.18	-0.29	-0.09	0.67	0.20	1.03
BBB2	1.918	0.574	1713	11.139	1.188	0.914
fit	1.920	0.579	1724	11.107	1.190	0.985
%	0.10	0.97	0.61	-0.29	0.17	7.75
FPS	1.799	0.530	1719	10.850	1.137	0.883
fit	1.799	0.533	1729	10.863	1.137	0.903
%	-0.03	0.67	0.55	0.12	0.03	2.29
ENGVIK	2.240	0.654	1611	12.059	1.372	1.000
fit	2.239	0.657	1616	11.975	1.359	1.107
%	-0.05	0.39	0.31	-0.69	-0.97	10.71
MPA1	2.461	0.670	1491	12.473	1.455	0.994
fit	2.457	0.670	1497	12.440	1.449	1.043
%	-0.16	-0.05	0.13	-0.26	-0.41	4.91
MS00	2.767	0.606	1236	14.918	1.944	0.888
fit	2.752	0.603	1238	14.927	1.942	0.998
%	-0.54	-0.52	0.16	0.06	-0.09	12.44
MS1506	1.806	0.343	1176	14.464	1.658	0.582
fit	1.798	0.352	1210	14.074	1.666	0.605

Continued on next page...

EOS	$M_{\max}$	$z_{\max}$	$f_{\max}$	$R_{1.4}$	$I_{1.338}$	$v_{s,\max}$
%	-0.42	2.57	2.86	-2.69	0.46	3.96
MS2	2.776	0.614	1244	14.583	1.888	0.889
fit	2.747	0.611	1252	14.535	1.876	0.990
%	-1.03	-0.56	0.64	-0.32	-0.64	11.38
PAL2	1.477	0.374	1559	10.547	1.051	0.693
fit	1.470	0.372	1559	10.490	1.030	0.702
%	-0.47	-0.51	0.01	-0.54	-2.03	1.37
PRAKDAT	1.788	0.366	1263	13.954	1.715	0.641
fit	1.777	0.365	1266	14.080	1.698	0.673
%	-0.60	-0.37	0.26	0.90	-0.98	5.11
SLY4	2.049	0.592	1641	11.736	1.288	0.989
fit	2.049	0.597	1650	11.712	1.287	1.003
%	0.02	0.81	0.57	-0.21	-0.08	1.41
WFF1	2.133	0.739	1832	10.414	1.085	1.185
fit	2.127	0.755	1863	10.416	1.086	1.279
%	-0.29	2.21	1.67	0.02	0.10	7.86
WFF2	2.198	0.717	1745	11.159	1.204	1.139
fit	2.195	0.723	1756	11.128	1.196	1.230
%	-0.14	0.71	0.59	-0.28	-0.59	7.93
WFF3	1.844	0.530	1678	10.926	1.160	0.835
fit	1.835	0.542	1715	10.913	1.157	0.903
%	-0.48	2.26	2.22	-0.12	-0.253	8.11
BALBN1H1	1.628	0.437	1625	12.901	1.504	0.878
fit	1.634	0.422	1569	12.648	1.512	0.813
%	0.39	-3.55	-3.45	-1.96	0.56	-7.42
GLENDNH3	1.962	0.427	1321	14.203	1.713	0.750
fit	1.964	0.429	1323	14.163	1.720	0.765
%	0.13	0.37	0.19	-0.28	0.38	2.04
GM1NPH	1.788	0.343	10.091	0.976	0.716	
fit	1.798	0.352	1210	0.67	0.20	1.03

Continued on next page. . .

EOS	$M_{\max}$	$z_{\max}$	$f_{\max}$	$R_{1.4}$	$I_{1.338}$	$v_{s,\max}$
%	-0.79	1.07	1.82	0.31	-1.18	7.05
GM2NPH	1.666	0.322	11.107	1.190	0.985	
fit	1.653	0.320	1201	13.518	1.610	0.573
%	-0.77	-0.55	0.24	0.29	-0.82	1.38
GM3NPH	1.555	0.311	1244	12.861	1.488	0.561
fit	1.540	0.307	1237	12.857	1.467	0.577
%	-0.92	-1.47	-0.54	-0.03	-1.45	2.81
SCHAF1[1]	1.382	0.395	1752	–	0.766	0.695
fit	1.368	0.393	1760	–	0.742	0.698
%	-1.00	-0.64	0.43	–	-3.13	0.49
SCHAF2[1]	1.653	0.339	1269	14.299	1.795	0.592
fit	1.648	0.365	1365	14.308	1.736	0.687
%	-0.30	7.71	7.59	0.07	-3.33	16.10
PS	1.755	0.355	1250	15.472	2.067	0.691
fit	1.728	0.350	1252	16.048	2.004	0.742
%	-1.53	-1.45	0.17	3.72	-3.06	7.36
PCL_NPHQ	1.482	0.326	1366.14	11.761	1.291	0.600
fit	1.470	0.319	1347	11.625	1.249	0.610
%	-0.79	-2.25	-1.42	-1.15	-3.27	1.74
ALF1	1.495	0.386	1585	9.896	0.987	0.565
fit	1.488	0.400	1644	9.875	0.983	0.670
%	-0.53	3.52	3.71	-0.22	-0.40	18.59
ALFC	2.086	0.436	1264	13.188	1.638	0.642
fit	1.976	0.433	1327	12.7058	1.524	0.652
%	-5.26	-0.62	4.99	-3.66	-6.94	1.50
ALF2	1.473	0.358	1501	10.314	1.041	0.565
fit	1.472	0.367	1536	10.288	1.049	0.629
%	-0.06	2.46	2.35	-0.25	0.76	11.29
ALF3	1.943	0.454	1407	11.667	1.297	0.685
fit	1.925	0.457	1427	11.527	1.266	0.786
%	-0.93	0.59	1.44	-1.20	-2.38	14.78

Continued on next page...

EOS	$M_{\max}$	$z_{\max}$	$f_{\max}$	$R_{1.4}$	$I_{1.338}$	$v_{s,\max}$
σ	0.99	2.01	1.98	1.25	1.63	5.58

[1]Tabled EOS does not extend to central density of maximum mass star with this crust; maximum sound velocity cannot be accurately estimated.

Bibliography

[1] J. H. Taylor. Binary Pulsars and Relativistic Gravity. In *Bulletin of the American Astronomical Society*, volume 26 of *Bulletin of the American Astronomical Society*, page 971, May 1994.

[2] F. Reif. *Fundamentals of statistical and thermal physics*. McGraw-Hill, 1965.

[3] N. K. Glendenning. *Compact stars: nuclear physics, particle physics, and general relativity*. Springer-Verlag, New York, 2000.

[4] S. L. Shapiro and S. A. Teukolsky. *Black holes, white dwarfs, and neutron stars: The physics of compact objects*. Wiley-Interscience, 1983.

[5] G. Baym, H. A. Bethe, and C. J. Pethick. Neutron star matter. *Nuclear Physics A*, 175:225–271, 1971.

[6] F. Douchin and P. Haensel. A unified equation of state of dense matter and neutron star structure. A&A, 380:151–167, December 2001. `arXiv:astro-ph/0111092`.

[7] J. R. Oppenheimer and G. M. Volkoff. On Massive neutron cores. *Phys. Rev.*, 55:374–381, 1939.

[8] Lee Lindblom. Determining the nuclear equation of state from neutron-star masses and radii. *The Astrophysical Journal*, 308:569–573, October 1992.

[9] Norman K. Glendenning and Christiane Kettner. Non-Identical Neutron Star Twins. *Astron. Astrophys.*, 353:L9, 2000. `arXiv:astro-ph/9807155`.

[10] J. B. Hartle. Slowly Rotating Relativistic Stars. I. Equations of Structure. ApJ, 150:1005, December 1967.

[11] J. B. Hartle and K. S. Thorne. Slowly Rotating Relativistic Stars. II. Models for Neutron Stars and Supermassive Stars. ApJ, 153:807, September 1968.

[12] I. A. Morrison, T. W. Baumgarte, S. L. Shapiro, and V. R. Pandharipande. The Moment of Inertia of the Binary Pulsar J0737-3039A: Constraining the Nuclear Equation of State. ApJ, 617:L135–L138, December 2004. `arXiv:astro-ph/0411353`.

[13] N. Stergioulas and J. L. Friedman. Comparing models of rapidly rotating relativistic stars constructed by two numerical methods. ApJ, 444:306–311, May 1995. `arXiv:astro-ph/9411032`.

[14] Sharon Morsink. Users manual for rns: version 2.0, 2007. Provided with source for rns code. Available from: `http://www.gravity.phys.uwm.edu/rns/`.

[15] G. B. Cook, S. L. Shapiro, and S. A. Teukolsky. Rapidly rotating neutron stars in general relativity: Realistic equations of state. ApJ, 424:823–845, April 1994.

[16] T. Nozawa, N. Stergioulas, E. Gourgoulhon, and Y. Eriguchi. Construction of highly accurate models of rotating neutron stars - comparison of three different numerical schemes. A&AS, 132:431–454, November 1998. `arXiv:gr-qc/9804048`.

[17] Nikolaos Stergioulas. Rotating stars in relativity. *Living Reviews in Relativity*, 6(3), 2003. Available from: `http://www.livingreviews.org/lrr-2003-3`.

[18] H. Komatsu, Y. Eriguchi, and I. Hachisu. Rapidly rotating general relativistic stars. I - Numerical method and its application to uniformly rotating polytropes. MNRAS, 237:355–379, March 1989.

[19] J. L. Friedman, J. R. Ipser, and R. D. Sorkin. Turning-point method for axisymmetric stability of rotating relativistic stars. ApJ, 325:722–724, February 1988.

[20] P. Haensel and J. L. Zdunik. A submillisecond pulsar and the equation of state of dense matter. Nature, 340:617–619, August 1989.

[21] P. Haensel, M. Salgado, and S. Bonazzola. Equation of state of dense matter and maximum rotation frequency of neutron stars. A&A, 296:745, April 1995.

[22] J. L. Friedman, L. Parker, and J. R. Ipser. Rapidly rotating neutron star models. ApJ, 304:115–139, May 1986.

[23] J. M. Lattimer, M. Prakash, D. Masak, and A. Yahil. Rapidly rotating pulsars and the equation of state. ApJ, 355:241–254, May 1990.

[24] L. Engvik, E. Osnes, M. Hjorth-Jensen, G. Bao, and E. Ostgaard. Asymmetric Nuclear Matter and Neutron Star Properties. ApJ, 469:794, October 1996. `arXiv:nucl-th/9509016`.

[25] J. M. Lattimer and M. Prakash. Neutron Star Structure and the Equation of State. ApJ, 550:426–442, March 2001. `arXiv:astro-ph/0002232`.

[26] J. M. Lattimer and M. Prakash. Equation of state, neutron stars and exotic phases. *Nuclear Physics A*, 777:479–496, October 2006.

[27] T. Klähn, D. Blaschke, S. Typel, E. N. E. van Dalen, A. Faessler, C. Fuchs, T. Gaitanos, H. Grigorian, A. Ho, E. E. Kolomeitsev, M. C. Miller, G. Röpke, J. Trümper, D. N. Voskresensky, F. Weber, and H. H. Wolter. Constraints on the high-density nuclear equation of state from the phenomenology of compact stars and heavy-ion collisions. Phys. Rev. C, 74(3):035802, September 2006. `arXiv:nucl-th/0602038`.

[28] D. Page and S. Reddy. Dense Matter in Compact Stars: Theoretical Developments and Observational Constraints. *Annual Review of Nuclear and Particle Science*, 56:327–374, November 2006. `arXiv:astro-ph/0608360`.

[29] C. Vuille and J. Ipser. On the Maximum Mass of Neutron Stars. In C. P. Burgess and R. C. Myers, editors, *General Relativity and Relativistic Astrophysics*, volume 493, page 60, College Park MD, 1999. American Institute of Physics.

[30] J. L. Zdunik, M. Bejger, P. Haensel, and E. Gourgoulhon. Phase transitions in rotating neutron stars cores: back bending, stability, corequakes, and pulsar timing. A&A, 450:747–758, May 2006. `arXiv:astro-ph/0509806`.

[31] M. Bejger, P. Haensel, and J. L. Zdunik. Mixed-phase induced core-quakes and the changes in neutron-star parameters. MNRAS, 359:699–706, May 2005. arXiv:astro-ph/0502348.

[32] P. Haensel and A. Y. Potekhin. Analytical representations of unified equations of state of neutron-star matter. A&A, 428:191–197, December 2004. arXiv:astro-ph/0408324.

[33] Masaru Shibata, Keisuke Taniguchi, and Koji Uryu. Merger of binary neutron stars with realistic equations of state in full general relativity. *Physical Review D*, 71:084021, 2005.

[34] M. Prakash, T. L. Ainsworth, and J. M. Lattimer. Equation of state and the maximum mass of neutron stars. *Phys. Rev. Lett.*, 61(22):2518–2521, Nov 1988.

[35] A. Akmal, V. R. Pandharipande, and D. G. Ravenhall. Equation of state of nucleon matter and neutron star structure. *Phys. Rev. C*, 58(3):1804–1828, Sep 1998.

[36] B. Friedman and V. R. Pandharipande. Hot and cold, nuclear and neutron matter. *Nuclear Physics A*, 361:502–520, 1981.

[37] R. B. Wiringa, V. Fiks, and A. Fabrocini. Equation of state for dense nucleon matter. *Phys. Rev. C*, 38(2):1010–1037, Aug 1988.

[38] M. Baldo, I. Bombaci, and G. F. Burgio. Microscopic nuclear equation of state with three-body forces and neutron star structure. A&A, 328:274–282, December 1997. arXiv:astro-ph/9707277.

[39] W. Zuo, I. Bombaci, and U. Lombardo. Asymmetric nuclear matter from an extended brueckner-hartree-fock approach. *Phys. Rev. C*, 60(2):024605, Jul 1999.

[40] L. Engvik, G. Bao, M. Hjorth-Jensen, E. Osnes, and E. Østgaard. Asymmetric nuclear matter and neutron star properties. *Astrophysical Journal*, 469:794, 1996. arXiv:nucl-th/9509016v1.

[41] H. Muther, M. Prakash, and T. L. Ainsworth. The nuclear symmetry energy in relativistic Brueckner-Hartree-Fock calculations. *Physics Letters B*, 199:469–474, t 1987.

[42] H. Müller and B. D. Serot. Relativistic mean-field theory and the high-density nuclear equation of state. *Nuclear Physics A*, 606:508–537, February 1996. arXiv:nucl-th/9603037.

[43] N. K. Glendenning and S. A. Moszkowski. Reconciliation of neutron-star masses and binding of the λ in hypernuclei. *Phys. Rev. Lett.*, 67(18):2414–2417, Oct 1991.

[44] V. R. Pandharipande and R. A. Smith. A model neutron solid with π^0 condensate. *Nuclear Physics A*, 237:507–532, January 1975.

[45] Norman K. Glendenning and Jürgen Schaffner-Bielich. First order kaon condensate. *Phys. Rev. C*, 60(2):025803, Jul 1999.

[46] S. Balberg and A. Gal. An effective equation of state for dense matter with strangeness. *Nuclear Physics A*, 625:435–472, February 1997. arXiv:nucl-th/9704013.

[47] N. K. Glendenning. Neutron stars are giant hypernuclei? ApJ, 293:470–493, June 1985.

[48] M. Prakash, J. R. Cooke, and J. M. Lattimer. Quark-hadron phase transition in protoneutron stars. *Phys. Rev. D*, 52(2):661–665, Jul 1995.

[49] M. Alford, M. Braby, M. Paris, and S. Reddy. Hybrid Stars that Masquerade as Neutron Stars. ApJ, 629:969–978, August 2005. arXiv:nucl-th/0411016.

[50] S. E. Thorsett and Deepto Chakrabarty. Neutron Star Mass Measurements. I. Radio Pulsars. *Astrophys. J.*, 512:288, 1999. arXiv:astro-ph/9803260.

[51] Scott M. Ransom et al. Twenty-One Millisecond Pulsars in Terzan 5 Using the Green Bank Telescope. *Science*, 307:892–896, 2005. arXiv:astro-ph/0501230.

[52] Paulo C. C. Freire, Alex Wolszczan, Maureen van den Berg, and Jason W. T. Hessels. A Massive Neutron Star in the Globular Cluster M5. 2007. `arXiv:astro-ph/0712.3826`.

[53] Paulo C. C. Freire et al. Eight New Millisecond Pulsars in NGC 6440 and NGC 6441. 2007. `arXiv:astro-ph/0711.0925`.

[54] J. Cottam, F. Paerels, and M. Mendez. Gravitationally redshifted absorption lines in the X-ray burst spectra of a neutron star. *Nature*, 420:51–54, 2002. `arXiv:astro-ph/0211126`.

[55] J. Cottam et al. The Burst Spectra of EXO 0748-676 during a Long 2003 XMM-Newton Observation. 2007. `arXiv:astro-ph/0709.4062`.

[56] F. Ozel. Soft equations of state for neutron-star matter ruled out by EXO 0748-676. *Nature*, 441:1115–1117, 2006.

[57] Jason W. T. Hessels et al. A Radio Pulsar Spinning at 716 Hz. *Science*, 2006. `arXiv:astro-ph/0601337`.

[58] Philip Kaaret et al. Discovery of 1122 Hz X-Ray Burst Oscillations from the Neutron-Star X-Ray Transient XTE J1739-285. 2006. `arXiv:astro-ph/0611716`.

[59] James M. Lattimer and Bernard F. Schutz. Constraining the equation of state with moment of inertia measurements. *The Astrophysical Journal*, 629:979–984, 2005.

[60] E. Gourgoulhon. Construction of initial data for 3+1 numerical relativity. *Journal of Physics Conference Series*, 91:2001, November 2007. `arXiv:0704.0149`.

[61] M. Shibata, K. Uryū, and J. L. Friedman. Deriving formulations for numerical computation of binary neutron stars in quasicircular orbits. Phys. Rev. D, 70(4):044044, August 2004. `arXiv:gr-qc/0407036`.

[62] S. Yoshida, B. C. Bromley, J. S. Read, K. Uryu, and J. L. Friedman. Models of helically symmetric binary systems. *Classical and Quantum Gravity*, 23:599, August 2006. `arXiv:gr-qc/0605035`.

[63] K. Uryū, F. Limousin, J. L. Friedman, E. Gourgoulhon, and M. Shibata. Binary Neutron Stars: Equilibrium Models beyond Spatial Conformal Flatness. *Physical Review Letters*, 97(17):171101, October 2006. `arXiv:gr-qc/0511136`.

[64] Koji Uryu. A collection of equations for helically symmetric perfect fluid spacetimes. Personal notes.

[65] John L. Friedman. Initial value equations. Personal notes.

[66] K. ō. Uryū and Y. Eriguchi. New numerical method for constructing quasiequilibrium sequences of irrotational binary neutron stars in general relativity. Phys. Rev. D, 61(12):124023, June 2000. `arXiv:gr-qc/9908059`.

[67] Antonios A. Tsokaros and Koji Uryu. Numerical method for binary black hole / neutron star initial data: Code test. *Phys. Rev.*, D75:044026, 2007. `arXiv:gr-qc/0703030`.

[68] J. L. Friedman, K. Uryū, and M. Shibata. Thermodynamics of binary black holes and neutron stars. Phys. Rev. D, 65(6):064035, March 2002. `arXiv:gr-qc/0108070`.

[69] P. Grandclément, E. Gourgoulhon, and S. Bonazzola. Binary black holes in circular orbits. II. Numerical methods and first results. Phys. Rev. D, 65(4):044021, February 2002. `arXiv:gr-qc/0106016`.

[70] J. K. Blackburn and S. Detweiler. Close black-hole binary systems. Phys. Rev. D, 46:2318–2333, September 1992.

[71] John T. Whelan, William Krivan, and Richard H. Price. Quasi-stationary binary inspiral: Ii. radiation-balanced boundary conditions. *Class. Quantum Grav.*, 17:4895–4911, 2000.

[72] John T. Whelan, Christopher Beetle, Walter Landry, and Richard H. Price. Radiation-balanced simulations for binary inspiral. *Class. Quantum Grav.*, (19):1285–1290, 2002.

[73] R. H. Price. Binary inspiral: finding the right approximation. *Classical and Quantum Gravity*, 21:281, February 2004.

[74] Z. Andrade, C. Beetle, A. Blinov, B. Bromley, L. M. Burko, M. Cranor, R. Owen, and R. H. Price. Periodic standing-wave approximation: Overview and three-dimensional scalar models. Phys. Rev. D, 70(6):064001, September 2004. `arXiv:gr-qc/0310001`.

[75] C. G. Torre. The helically-reduced wave equation as a symmetric-positive system. *Journal of Mathematical Physics*, 44:6223–6232, December 2003.

[76] B. Bromley, R. Owen, and R. H. Price. Periodic standing-wave approximation: Nonlinear scalar fields, adapted coordinates, and the eigenspectral method. Phys. Rev. D, 71(10):104017, May 2005. `arXiv:gr-qc/0502034`.

[77] M. Boyle, D. A. Brown, L. E. Kidder, A. H. Mroué, H. P. Pfeiffer, M. A. Scheel, G. B. Cook, and S. A. Teukolsky. High-accuracy comparison of numerical relativity simulations with post-Newtonian expansions. Phys. Rev. D, 76(12):124038, December 2007. `arXiv:0710.0158`.

[78] Luc Blanchet. Gravitational radiation from post-newtonian sources and inspiralling compact binaries. *Living Reviews in Relativity*, 9(4), 2006. Available from: `http://www.livingreviews.org/lrr-2006-4`.

[79] T. Damour, B. R. Iyer, and B. S. Sathyaprakash. Comparison of search templates for gravitational waves from binary inspiral. Phys. Rev. D, 63(4):044023, February 2001. `arXiv:gr-qc/0010009`.

[80] L. Kidder. Matching of pn waveforms with long-time numerical evolutions. In *APS April Meeting Session X7*, 2008.

[81] M. Shibata, K. Taniguchi, and K. Uryū. Merger of binary neutron stars with realistic equations of state in full general relativity. Phys. Rev. D, 71(8):084021, April 2005. `arXiv:gr-qc/0503119`.

[82] Lawrence E. Kidder. Using full information when computing modes of post-newtonian waveforms from inspiralling compact binaries in circular orbit. *Physical Review D (Particles, Fields, Gravitation, and Cosmology)*, 77(4):044016, 2008. `arXiv:0710.0614`.

[83] C. Cutler and É. E. Flanagan. Gravitational waves from merging compact binaries: How accurately can one extract the binary's parameters from the inspiral waveform? Phys. Rev. D, 49:2658–2697, March 1994. `arXiv:gr-qc/9402014`.

[84] C. Cutler. Gravitational wave data analysis (with an introduction to sources). Notes from CGWA Summer School, 7-11 June 2004.

[85] B. Allen, W. G. Anderson, P. R. Brady, D. A. Brown, and J. D. E. Creighton. FINDCHIRP: an algorithm for detection of gravitational waves from inspiraling compact binaries. *ArXiv General Relativity and Quantum Cosmology e-prints*, September 2005. `arXiv:gr-qc/0509116`.

[86] M. Vallisneri. Use and Abuse of the Fisher Information Matrix in the Assessment of Gravitational-Wave Parameter-Estimation Prospects. *ArXiv General Relativity and Quantum Cosmology e-prints*, March 2007. `arXiv:gr-qc/0703086`.

[87] R. Abbot, R. Adhikari, S. Ballmer, L. Barsotti, M. Evans, P. Fritschel, V. Frolov, G. Mueller, B. Slagmolen, and S. Waldman. Advligo interferometer sensing and control conceptual design. May 2008. Technical note LIGO-T070247-01-I.

[88] S. A. Hughes. Tuning gravitational-wave detector networks to measure compact binary mergers. *Physical Review D*, 66(10):102001, November 2002. `arXiv:gr-qc/0209012`.

[89] M. Vallisneri. Prospects for Gravitational-Wave Observations of Neutron-Star Tidal Disruption in Neutron-Star-Black-Hole Binaries. *Physical Review Letters*, 84:3519–3522, April 2000. `arXiv:gr-qc/9912026`.

[90] D. Lai and A. G. Wiseman. Innermost stable circular orbit of inspiraling neutron-star binaries: Tidal effects, post-Newtonian effects, and the neutron-star equation of state. Phys. Rev. D, 54:3958–3964, September 1996. `arXiv:gr-qc/9609014`.

[91] D. Gondek-Rosińska, M. Bejger, T. Bulik, E. Gourgoulhon, P. Haensel, F. Limousin, K. Taniguchi, and L. Zdunik. The final phase of inspiral of neutron stars: Realistic equations of state. *Advances in Space Research*, 39:271–274, 2007.

[92] Pedro Marronetti, Matthew D. Duez, Stuart L. Shapiro, and Thomas W. Baumgarte. Dynamical determination of the innermost stable circular orbit of binary neutron stars. *Physical Review Letters*, 92:141101, 2004.

[93] J. A. Faber, P. Grandclément, F. A. Rasio, and K. Taniguchi. Measuring Neutron-Star Radii with Gravitational-Wave Detectors. *Physical Review Letters*, 89(23):231102, November 2002. `arXiv:astro-ph/0204397`.

[94] M. Bejger, D. Gondek-Rosińska, E. Gourgoulhon, P. Haensel, K. Taniguchi, and J. L. Zdunik. Impact of the nuclear equation of state on the last orbits of binary neutron stars. *Astronomy and Astrophysics*, 431:297–306, February 2005. `arXiv:astro-ph/0406234`.

[95] R. Oechslin and H.-T. Janka. Gravitational Waves from Relativistic Neutron-Star Mergers with Microphysical Equations of State. *Physical Review Letters*, 99(12):121102, September 2007. `arXiv:astro-ph/0702228`.

[96] T. Mora and C. M. Will. Post-Newtonian diagnostic of quasiequilibrium binary configurations of compact objects. Phys. Rev. D, 69(10):104021, May 2004. `arXiv:gr-qc/0312082`.

[97] E. Berti, S. Iyer, and C. M. Will. Post-Newtonian diagnosis of quasiequilibrium configurations of neutron star–neutron star and neutron star–black hole binaries. Phys. Rev. D, 77(2):024019, January 2008. `arXiv:0709.2589`.

[98] É. É. Flanagan and T. Hinderer. Constraining neutron-star tidal Love numbers with gravitational-wave detectors. Phys. Rev. D, 77(2):021502, January 2008. `arXiv:0709.1915`.

[99] T. Hinderer. Tidal Love Numbers of Neutron Stars. ApJ, 677:1216–1220, April 2008. `arXiv:0711.2420`.

[100] M. Shibata, K. Taniguchi, and K. Uryū. Merger of binary neutron stars of unequal mass in full general relativity. Phys. Rev. D, 68(8):084020, October 2003. `arXiv:gr-qc/0310030`.

[101] M. Shibata and K. Uryū. Gravitational Waves from Merger of Binary Neutron Stars in Fully General Relativistic Simulation. *Progress of Theoretical Physics*, 107:265–303, February 2002. `arXiv:gr-qc/0203037`.

[102] Masaru Shibata. Axisymmetric general relativistic hydrodynamics: Long-term evolution of neutron stars and stellar collapse to neutron stars and black holes. *Phys. Rev. D*, 67(2):024033, Jan 2003.

[103] P. Haensel. Equation of state of dense matter and maximum mass of neutron stars. In J.-M. Hameury and C. Motch, editors, *Final Stages of Stellar Evolution*, volume 7 of *EAS Publication Series*, Les Ulis, France, 2003. EDP Sciences.

[104] L. Engvik, M. Hjorth-Jensen, E. Osnes, G. Bao, and E. Østgaard. Asymmetric nuclear matter and neutron star properties. *Phys. Rev. Lett.*, 73(20):2650–2653, Nov 1994.

[105] C. P. Lorenz, D. G. Ravenhall, and C. J. Pethick. Neutron star crusts. *Phys. Rev. Lett.*, 70(4):379–382, Jan 1993.

[106] P. Haensel and B. Pichon. Experimental nuclear masses and the ground state of cold dense matter. A&A, 283:313–318, March 1994. `arXiv:nucl-th/9310003`.

[107] M. Alford, M. Braby, M. Paris, and S. Reddy. Hybrid Stars that Masquerade as Neutron Stars. ApJ, 629:969–978, August 2005. `arXiv:nucl-th/0411016`.

Curriculum Vitae

Jocelyn S. Read

Place of Birth

Calgary, Alberta, Canada

Education

B.Sc., University of British Columbia	1997–2002
Combined Honours Mathematics and Physics	
Ph.D., University of Wisconsin–Milwaukee	2003–2008
Physics	

Dissertation Title:

Neutron stars in compact binary systems:
from the equation of state to gravitational wave detection

Publications

1. Yoshida S, Bromley B C, Read J S, Uryu K, and Friedman J L, *Models of helically symmetric binary systems*, Classical and Quantum Gravity **23** 599 (August 2006)

2. Siemens X, Creighton J, Maor I, Majumder S R, Cannon K, and Read J, *Gravitational wave bursts from cosmic (super)strings: Quantitative analysis and constraints*, prd **73** 105001 (May 2006)

Awards and Fellowships

2007-2008	UWM Graduate School Dissertation Fellowship
2007	Midwest Relativity Meeting Blue Apple Award
2003-2008	UWM Chancellor's Graduate Student Award
2003	UWM Papastamatiou Scholarship
2001	UBC Arthur Crooker Prize

Professor John Friedman Date

Professor Jolien Creighton Date